Freie Universität Berlin
Fachbereich Physik

Terahertz Transmission Spectroscopy of the Organic Polymer: PEDOT:PSS

Diplomarbeit

Monika Weber

29 Mai 2009

Diese Arbeit entstand in der Arbeitsgruppe von
Prof. Dr. Martin Wolf an der Freien Universität Berlin.

Berlin, im Mai 2009

Contents

List of Figures

What makes polymers so interesting?

Why not have a flexible mobile display printed at home? Electronics that are printable like an ordinary newspaper would revolutionize everyday life. Twenty years ago this seemed like a sci-fi dream, today commercial applications already exist. This is due to the discovery of organic light emitting diode (OLED) technology by Ching Tang and Steven Van Slyke from the Eastman Kodak Company in 1987 [TS87]. This breakthrough discovery gave rise to a growing interest by the research community and the commercial sector. As a result of the unique features of polymers, years later, a new generation of display devices and electronic equipment has been introduced into the market [DD08], [Fix08], [KH08], [LBNL08] such as organic field-effect transistors, [Koc08], organic light emitting diode television [Son09] and displays, photovoltaic cells (OPVCs), coatings, sensors, memory cells [Koc07].

Among the immediate advantages of polymer-based electronic devices are their simpler and cheaper manufacturing compared to conventional semiconductors. Printing is one of the fastest and cheapest processing methods. Further benefits are flexibility, lower cost and, what is perhaps even more important, the lower energy consumptions of devices which translates into environmental friendliness [GJF$^+$00].

It is crucial for organic electronics that polymers are showing characteristics of metals, insulators and semiconductors in order that basic components of conventional silicon-based technology can be replaced by organic materials. The field of organic materials took a revolutionary leap forward in 1977 when H. Shirakawa, A. G. MacDiarmid and A. J. Heeger [SMH00] discovered intrinsically conducting polymers (ICP), for which they were awarded the Nobel Prize in 2000. A conducting polymer poly(3,4-ethylenedioxythiophene)-poly(styrenesulfonate) (PEDOT:PSS) has been widely used first in antistatic and later on in electronic applications and is one of the most commonly used conducting polymers on the market [KR05].

Growing research and industrial interest in the field of organic electronics means an answer to the following fundamental question is dearly needed: what is the nature of the charge transfer mechanism in PEDOT:PSS? Surprisingly, a fuller the understanding of the charge transfer mechanism is still lacking. Optical conductivity in the far infrared region has not been investigated yet. We aim to better understand the charge transfer mechanism of PEDOT:PSS. To achieve this, we will apply the time-domain terahertz spectroscopy to derive the dielectric properties and the conductivity of PEDOT:PSS thin films.

Time-domain terahertz spectroscopy (TD-TS) is a sensitive tool for charge carrier investigation. Low photon energies correspond to the low excitation energy of weakly bound charge carriers in materials, thus TD-TS reveals information about charge transport properties. Ultrashort laser pulses, in transmission measurements, cause an excitation of an electric field with a frequency $\omega/2\pi$ from 10 to 30 THz, 1 THz corresponds to an energy of 4.1 meV. The Fourier transformation of the temporal electric field transmitted through a PEDOT:PSS thin film and a silicon wafer for reference, gives the complex transmission: $Q(\omega) = \frac{\vec{E}_{\mathrm{sample}}(\omega)}{\vec{E}_{\mathrm{reference}}(\omega)}$, which, in turn, contains the material's response function. Further, it allows the extraction of material properties in the THz frequency range: the complex refractive index $\hat{n}$, the complex dielectric function $\hat{\epsilon}$ and the complex conductivity $\hat{\sigma}$.

Although electronic devices with applied PEDOT:PSS are usually operated at room temperature, it is useful to analyze the temperature dependence of the conductivity. Scattering processes in solids, like electron-electron and electron-phonon scattering, are temperature-dependent. Investigating the temperature dependence of conductivity also allows observing the temperature-induced changes in the scattering processes and by that a more precise identification of conduction mechanisms in solids. Thus, the conductivity was measured in a wide range of temperatures: from 4 K to 320 K.

The objective of this thesis is to measure and understand the dielectric properties and conductivity of self-prepared thin films of the conducting polymer PEDOT:PSS. In the first chapter of this work I give a general overview of conducting polymers and particularly of PEDOT:PSS. In the second chapter two optical material parameters determined by THz spectroscopy are introduced. The following conductivity models are described: the Drude model and it's generalization - the Drude Smith model, as well as two hopping conduction mechanisms: the variable range hopping (VRH) and quantum mechanical tunneling. Furthermore, I will refer to these conductivity models to interpret the experimentally determined optical conductivity. Chapter 3 contains experimental details concerning sample preparation, atomic force microscopy (AFM) and THz spectroscopy. In

this part I also present the morphology of PEDOT:PSS obtained by AFM measurements. Separately I present the results obtained with time-domain terahertz spectroscopy, which are the steady-state THz responses of PEDOT:PSS: the optical conductivity, the complex dielectric function and the complex refractive index. Additionally, in the Appendix, a thorough description of the material parameter extraction from THz measurements is given. It covers a derivation of the model for complex dielectric functions. Previously an approximation was used for the dielectric function calculation [Kam05]. Due to thin film phenomena, this approximation was not valid in the case of the PEDOT:PSS dielectric function extraction. The general formula had to be solved, for which a numerical approach was used. Finally, results obtained for various film thicknesses will be compared.

Chapter 1

Introduction to polymers

Polymers are high performance materials. Put into water solutions they can be easily processed, without a need for clean room facilities or highly precise lithography. Growing prices of conventional semiconductors make polymer applications more and more attractive. A constant quest for more powerful, smaller, thinner, flexible and cheaper electronics brought polymers to the focus of scientific research. Important members of the polymer family are conjugated polymers.

1.1 Conjugated polymers

Conjugated polymers are important due to their conducting behavior. They can overtake a role of metals in classical semiconductor devices. Conjugated polymers have a band structure of a semiconductor [Nar07]. This may seem to be a contradiction. The band structure of PEDOT:PSS will be discussed in details in section 1.3.2.

Conducting polymers have delocalized valence π electrons. Their carbon chains have double bonds alternating with single bonds and overlapping p_z orbitals. The carbon backbone can be linearly composed of alternating bonds or it can contain a phenyl ring [Bar05]. Figure 1.1 shows structures of common conjugated polymers.

The electron configuration of carbon is $1s^2 2s^2 2p^2$. Four valence electrons from $2s$ and $2p$ shells can form single, double or triple bonds. In conjugated polymers are three sp^2 hybridized orbitals and one unhybridized p_z orbital. Two sp^2 orbitals from each carbon atom form σ bonds with hybridized orbitals of neighboring carbon atoms in a polymer chain. The third hybrid orbital forms a bond with a C atom or an atom of a side group. The remaining p_z orbital forms a π bond with a p_z neighbor orbital (Fig.1.2). The perpendicular to the internuclear axis π bonds, unlike σ bonds, are weak, which results in electron delocalization [Bru08].

In conjugated polymers electrons in π bonds are responsible for conduction.

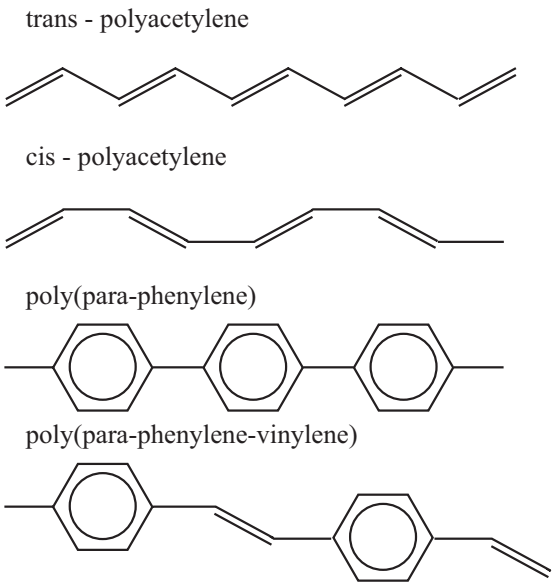

Figure 1.1: Examples of conjugated polymers [SR07]. Characteristic are double bond alternating with single bonds along the polymer structure.

There are conduction electrons from partially filled shells in a periodic potential of carbon bonds. Therefore they form a half filled band, which is characteristic for metals. In each molecule forming the polymer chain two characteristic orbitals can be distinguished: the highest occupied molecular orbital (HOMO) and the lowest unoccupied molecular orbital (LUMO). In π polymers are single $C-C$ and double $C=C$ bonds which form the periodic potential. Their lengths are different, which results in splitting of the interacting orbitals in monomer units. The split orbitals form the band structure. This leads to a formation of a valence band from the highest occupied molecular orbitals of monomer units and and a conduction band from the LUMOs in the hole chain like in solid state semiconductors. The band structure is one dimensional and is formed along the polymer chain, as interchain coupling is rather small [Koc07]. An energy gap in conjugated polymers arises from the difference in length between short (double) bonds and long (single) bonds [Nar07]. The energy gap ranges typically from 1.5 eV to 3.0 eV and can be varied by doping [Bru08]. Such a π system extends over a large number of monomers. As π electrons are responsible for conduction, conduction is strongly anisotropic: much higher along the conjugated chain.

In the intrinsic state the conduction band is practically not occupied. This is due to the large band gap, like 1.5 eV for PEDOT:PSS [GJF$^+$00]. To generate mobile carriers a polymer has to undergo oxidation (p-doping) and/or, less frequently, reduction (n-doping). The whole conjugated chain is composed of single molecules joined with each other by covalent bonds. The energy diagram of a conjugated polymer, a single molecule and the whole crystal, is shown in Fig.1.3.

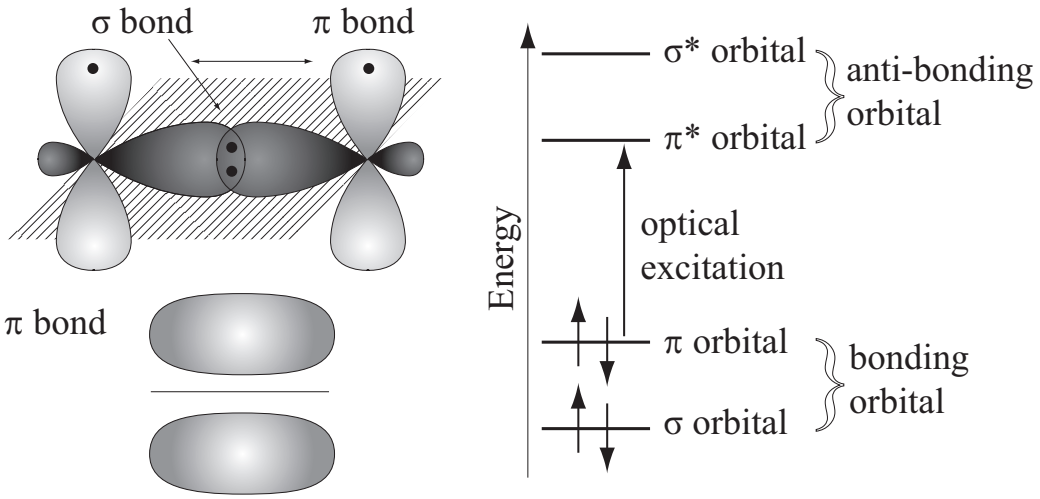

Figure 1.2: Conjugated π electron system. (left) σ bond in the atomic plane and π bonds formed from p_z orbitals in plane perpendicular to the atomic plane. (right) Energy diagram of a π conjugated systems. The lowest optical excitations are between the bonding π and anti-bonding π^* orbital [Bru08].

1.2 Electronic and optical properties of polymers

Owing to the structure of conjugated polymers intramolecular electronic interactions are much stronger than intermolecular electronic interactions. Overlap between electronic wave functions even in neighboring molecules is poor that's why the excited states are localized on single chains [Bru08].

Charge carriers injected into a polymer form polarons along the conjugated chain [CLRR98], which can be positively and negatively charged. A polaron is a moving charge carrier plus an induced lattice polarization, which forms an accompanying cloud of phonons. It behaves like a heavy particle, so it undergoes scattering processes accordingly to [MD71]. An electron with a following group of phonons forms a negative polaron.

Polymer chains are composed of single molecules forming segments (see Fig.1.4). In the highest occupied molecular orbital (HOMO) defect holes can also form polarons, which are positively charged in this case. Disorder and polaronic behavior of charge carriers are the known reasons for hopping transport (more details in section 2.4).

Two polarons with opposite charges can form an exiton, a bound electron-hole pair [Koc07]. These excitons are strongly bound and localized in one molecule. This type of excitons is called Frenkel excitons. The exciton radius is comparable with the molecule diameter and is in the order of nanometers, which results in high binding energies ≈ 0.5 eV. In conventional semiconductors the exciton binding energies are lower than the thermal energy at room temperature 25 meV,

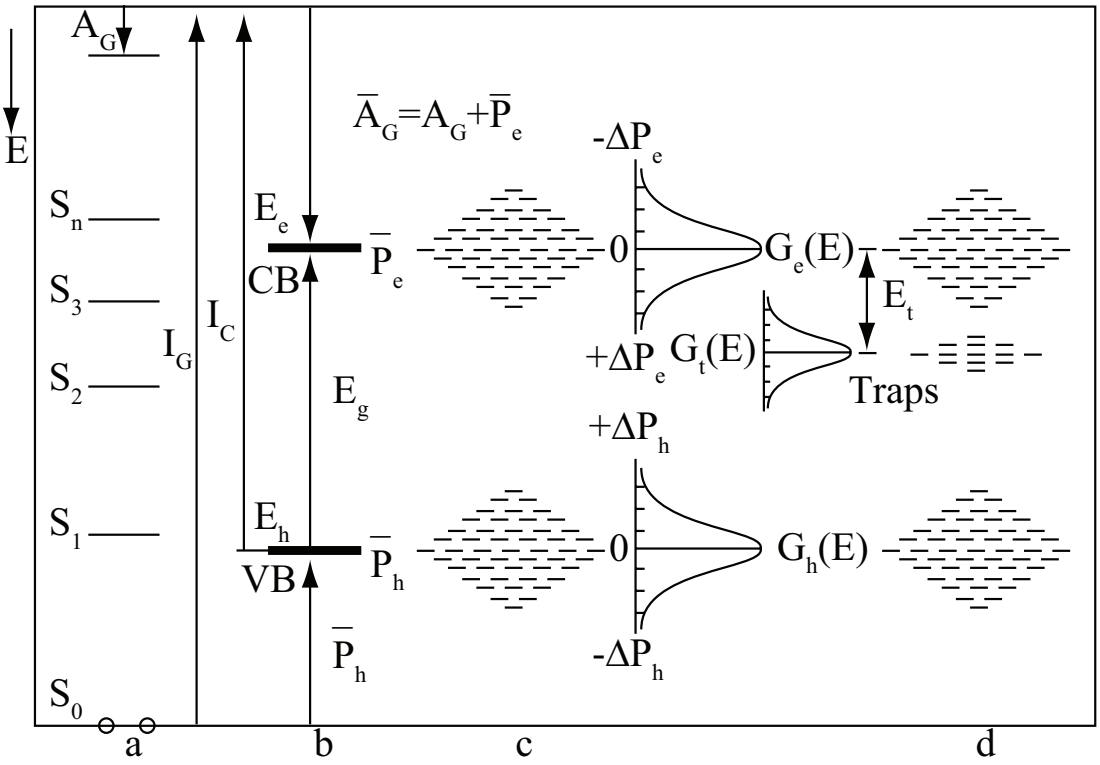

Figure 1.3: Energy diagram of a π conjugated system [SW05]. I_G is the ionization energy of the molecule, A_G is the electron affinity.
a) Energy diagram of a *single molecule* forming the conjugated chain. It consists of the ground state S_0 and excited singuletts S_n.
b) Energy diagram of the *ionized crystal*. Overlapping HOMOs form a valence band (VB) and LUMOs form a conduction band (CB). E_h, E_e - energy of holes and of conduction electrons. $E_g = E_e - E_h$ is the energy gap and $\bar{P}_e$, $\bar{P}_h$ - average polarization energies of electrons and holes.
c) Shows the statistical distribution of the electron and hole polarization energies P_e, P_h. They form a density of states, corresponding $G_h(E)$ and $G_e(E)$.
d) A disturbance of a periodic structure, through molecule disorder, leads to creation of traps with a certain density of states $G_t(E)$. Polarization energies P_e, P_h depend on the ionization and affinity of the molecule and the crystal $P_e = A_C - A_G$, $P_h = I_G - I_C$.

which means that absorption of light results immediately in charge separation. Charge carriers in conjugated polymers cannot be separated easily because of these high exciton binding energies [Bru08].

There are three different types of interaction between electrons and phonons in amorphous materials: Phonons can scatter an electron contributing to the resistance; Phonons can be absorbed or emitted by electron in hopping conduction; Phonons can be trapped by electrons and form a polaron.

1.3 Conducting polymer PEDOT:PSS

PEDOT:PSS is a widely used conducting polymer. Desired features for an intrinsically conducting (IC) polymer suitable for commercial applications are of course high conductivity, comparable with metals, high stability in air or other processing conditions and easy processability. A breakthrough in achieving this aim was the invention of polymers of the bicyclic ethylenedioxythiophene group and its derivatives by Bayer Corporate Research Laboratories [KR05].

1.3.1 Macroscopic properties

The PEDOT:PSS water solution has a deep blue color, PEDOT:PSS films are transparent in the visible range [PGI02]. There is a considerable difference between PEDOT and PEDOT:PSS. PEDOT in situ is highly conductive. Under strictly controlled conditions conductivities as high as 1000 S cm^{-1} can be achieved for PEDOT [KR05]. The conductivity of PEDOT:PSS complex is significantly lower (Tab.1.1). The use of solvents, like sorbitrol, affects the polymer structure and electric properties of intrinsically conducting PEDOT [Nar07]. Conductivity enhancement is possible via chemical additives.

As the solid content of a PEDOT:PSS water solution is in the range of 1% to 3%, added non-volatile components or an impurity content of only 1% can influence the film composition up to 30%. The stability of PEDOT:PSS is excellent, it can be heated in air at 100°C for over 1000 h with only a minimal change in conductivity [GJF+00].

Spin coating of the aqueous dispersion of PEDOT:PSS is an easy and convenient way to deposit thin films on silicon substrates. Film thicknesses in the range 20 nm – 2400 nm can easily be achieved.

1.3.2 Structure

PEDOT:PSS belongs to the poly(ethylenedioxythiophene) group. It is an intrinsically conducting polymer, however it is unstable in air and not soluble in common solvents, which limits its applicability considerably. Addition of a negatively charged PSS group has a stabilizing function for positively charged PEDOT

PEDOT:PSS	Solid contents [%]	Conductivity [S cm^{-1}]	Application
1 : 2.5	1.3	1	Antistatics
1 : 6	1.5	10^{-3}	OLEDs
1 : 20	3.0	10^{-5}	Passive matrix displays

Table 1.1: PEDOT:PSS ratio dependent characteristics.

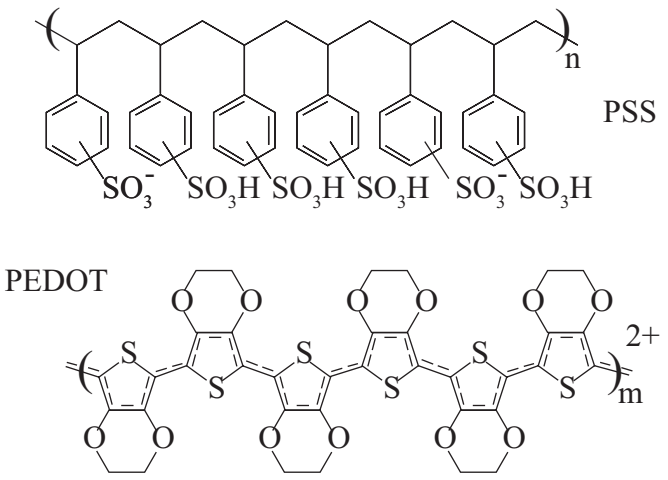

Figure 1.4: PEDOT:PSS chemical structure [Koc07]. See text for details.

ions [KR05]. PEDOT:PSS is composed of a conducting poly(3,4 - ethylene-dioxythiophene) polycation (PEDOT) and an insulating poly(styrenesulfonate) polyanion (PSS). The chemical structure is shown in the Fig.1.4. PEDOT is a p-type semiconductor, with a low band gap of 1.5 - 1.6 eV. Due to doping with $-SO_3^-$ groups from PSS [SGF07], two excess positive charges are injected over six monomer units. This gives rise to valence band population and good conductivity.

The polystyrene sulfonic anion (PSS) has two main functions. First, PSS is a source for the charge balancing counter ions. In the absence of PSS an oxidation product is formed on the PEDOT site. Secondly, because PEDOT alone is hydrophobic and PSS hydrophilic, PSS keeps PEDOT segments dispersed in a water solution. PEDOT π chains (light) are stack with a repeating distance 0.68 nm Fig.1.5. The counter ions from PSS (dark) are incorporated between PEDOT stacks. The size of the whole structure depends on the counter ions [KR05].

Small nanometer sized core-shell agglomerates with PSS shells are being formed in aquarious dispersions [Koc07]. As a result the PEDOT-PSS complex forms a stable, easy to process, water solution.

A structural model is shown in the Fig.1.6 During polymerization oligomeric

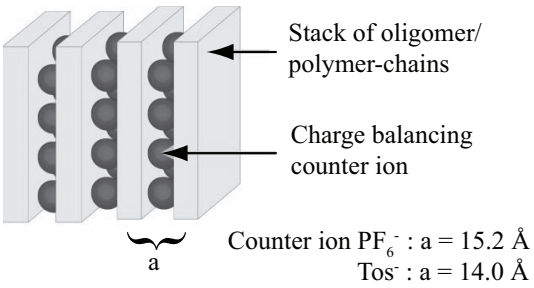

Figure 1.5: PEDOT:PSS stack, a 5 counter ion-dependent layer distance between stacks [KR05].

PEDOT is formed (primary structure) and attached to the long PSS chains, which form the secondary structure. PEDOT:PSS chains are swollen by water [GJF+00]. PSS has a much higher molecular weight than PEDOT and as it is hydrophilic is attracts water. As a results a gel with 90% to 95% water content is formed with a solid content depending PEDOT to PSS ratio (tertiary structure). Free PSS chains may gather at the surface of gel particles forming a thin negatively charged layer, which results in electrostatic repulsion between particles [SGF07]. The gel form of the PEDOT:PSS water solution is easy to process and widely used in industry [KR05].

Depending on the PEDOT to PSS ratio, optical and electric properties change. So the ratio of the solid content can be adjusted to meet custom applications. In the table 1.1 are summarized properties of three grades of PEDOT:PSS solutions [KR05]. Conductivity decreases with increasing solid content (increasing PSS content).

1.3.3 Applications

Antistatic Coatings

PEDOT:PSS found its first commercial application in antistatic coatings. High transparency in the visible range together with good conductivity, stability and processability are important features for antistatic layers for photographics films. During photographic film processing sides of the film rub against each other, what can result in charge accumulation and rapid electric discharges, which can destroy parts of the film and thus contained information. To avoid such effects films have to be coated with a conductive material. Each year the total optical film surface coated with PEDOT:PSS to form transparent antistatic layers is in the order of 100 million square meters. AGFA company developed for this purpose a special PEDOT solution called Orgacon [GJF+00].

Also to avoid discharging effects PEDOT:PSS is used for antistatic treatment of plastics. Adhesion of PEDOT:PSS on substrates such as glass and plastics is

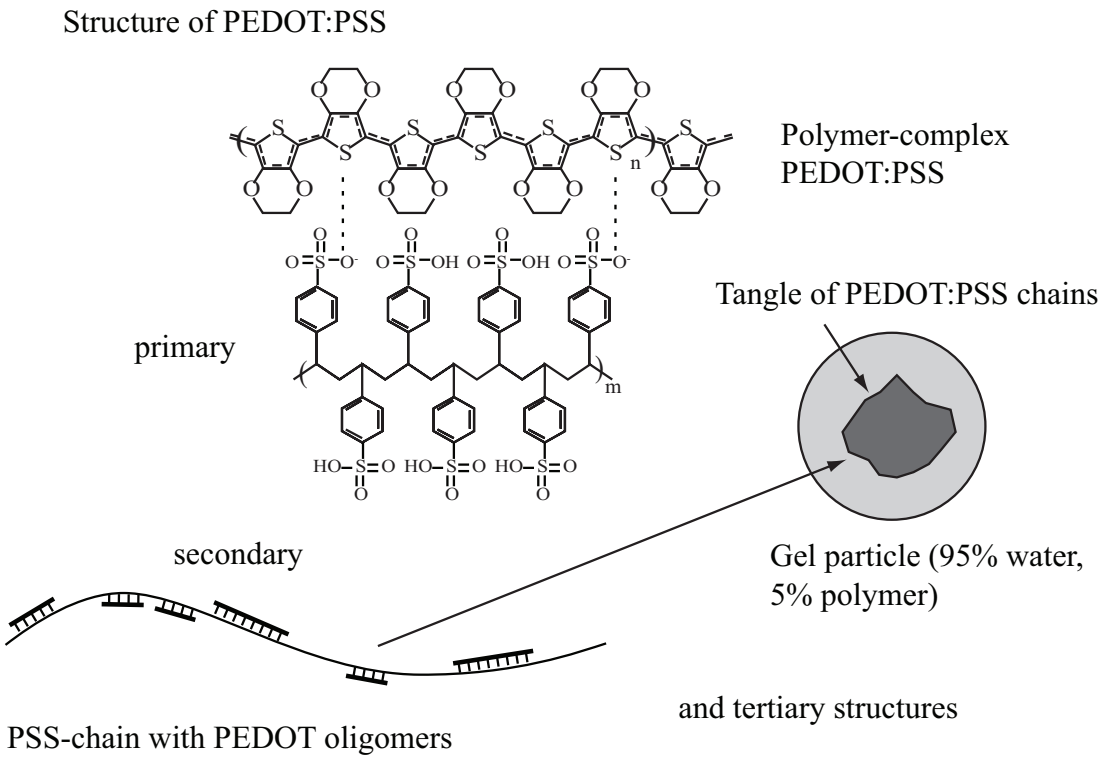

Figure 1.6: PEDOT:PSS primary, secondary and tertiary structure [KR05].

effective, thus PEDOT:PSS is also used for antistatic treatment in other applications e.g. packaging of electronic components.

Capacitors

PEDOT:PSS is an excellent choice of material for electrodes in capacitors Fig.1.7.

Bodies of modern capacitors consist of highly porous media in order to maximize their surface. Figure 1.7 shows a schematic picture of a Ta/Ta_2O_5 capacitor with tantalum (gray) and next layer of thin metal - oxide dielectric (white). PEDOT:PSS (blue) when applied as a solution penetrates easily the porous capacitor body resulting in a very good contact.

Its conductivity is roughly 1000 times higher than that of previously used MnO_2. PEDOT:PSS, because of the solution processing form, penetrates porous media much better than other substances in a solid form, making thus a much better electric contact [KR05]. The equivalent series resistance (ESR), which has a direct impact on the high frequency performance of a capacitor, is much lower when PEDOT:PSS is used as an electrode material.

A crucial aspect in capacitor manufacturing and usage is safety. Tantalum capacitors with manganese dioxide as an electrode material would ignite or even

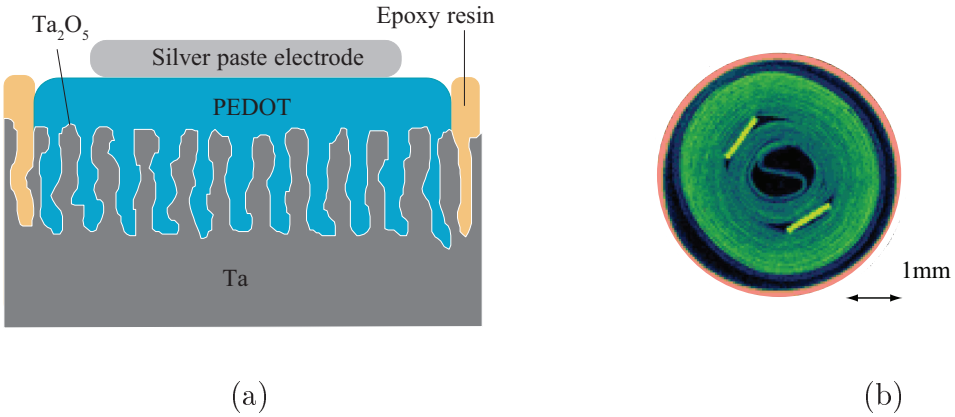

(a) (b)

Figure 1.7: a) PEDOT:PSS applied in capacitors [GJF+00] with high capacitance. To achieve high surface area, the tantalum electrode is roughen. A thin oxid Ta_2O_5 layer serves as dielectric. PEDOT:PSS coating forms the counter electrode. b) A round capacitor with a PEDOT:PSS counter electrode [Sta09].

explode when overcharged or overheated due to chemical reactions between metal and manganese dioxide. PEDOT:PSS in similar conditions, e.g. when leakage currents appear owing to a damage of a thin dielectric layer, losses locally its conductivity, so the device simply stops working [KR05].

Organic LEDs

A rapidly expanding area of applications are photoluminescent devices, in which PEDOT:PSS is used for conducting layers. Example devices with PEDOT:PSS solution called CLEVIOS, manufactured by C.H Starck Company are presented in Fig.1.8. Clevios is a solution of PEDOT:PSS with a 1 : 6 solid ratio to optimize OLED performance and minimize disturbing cross talking effects between pixels and still maintain good conductivity of a PEDOT:PSS layer.

To enhance OLED performance a thin and uniform layer of PEDOT:PSS is spin coated on an indium tin oxide ITO substrate, conductive anode, and covered with a next layer - an electroluminescent organic or polymer [Koc07].

The conducting polymer is also applied in organic light emitting diodes (OLED) for displays and television screens [JB09] Fig.1.9.

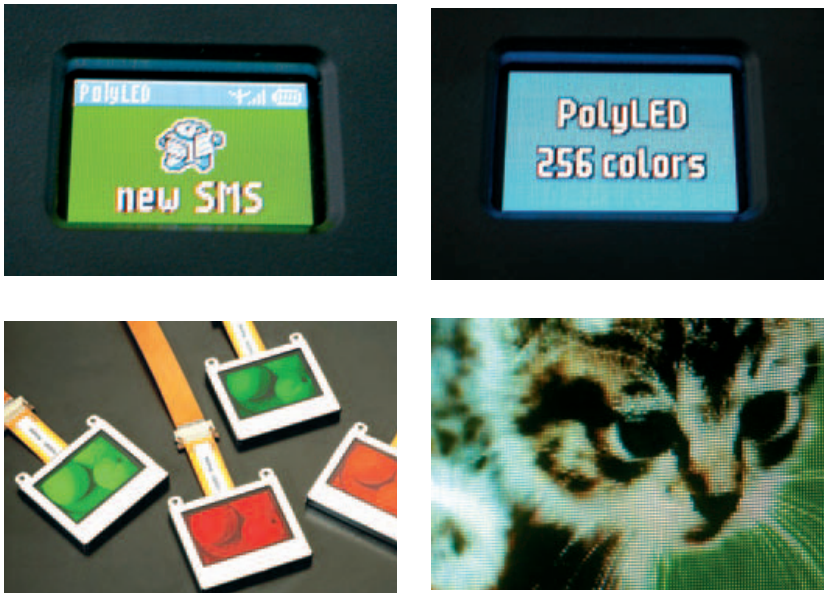

Figure 1.8: PEDOT:PSS in Organic LED applications [Sta09].

Figure 1.9: 'Incredibly Slim – Only 3mm thin!' says the advertisement of a new OLED Digital TV [Son09]. OLED (Organic Light Emitting Diode) television, featuring a 3mm thin panel and breathtaking image contrast, brightness and color.

Chapter 2

Electrical properties of solids

2.1 Dielectric function

Terahertz Spectroscopy, as well as other spectroscopic methods, investigates the interaction between electromagnetic radiation and matter, to gain information on, in this case, charge transport properties of material. Let us focus on the material parameters, in particular on the dielectric function.

Maxwell's equations describe the interaction of electromagnetic waves with matter [Jac99]:

$$\nabla \cdot \vec{D} = 4\pi\rho, \tag{2.1}$$

$$\nabla \times \vec{E} + \frac{1}{c}\frac{\partial \vec{B}}{\partial t} = 0, \tag{2.2}$$

$$\nabla \cdot \vec{B} = 0, \tag{2.3}$$

$$\nabla \times \vec{H} - \frac{1}{c}\frac{\partial \vec{D}}{\partial t} = \frac{4\pi}{c}\vec{J}. \tag{2.4}$$

Interesting is the response of a material to an electromagnetic wave acting at position $\vec{r}\,'$ and time t' [Jac99]

$$\vec{E}(\vec{r},t) = \vec{E_0}\exp\left\{i((\vec{k}\cdot\vec{r}-\omega t))\right\}, \tag{2.5}$$

which is the displacement vector $\vec{D}_i(\vec{r},t)$, at position $\vec{r}$ and time t, in a general case, for anisotropic media, represented as [Jac99]

$$\vec{D}_i(\vec{r},t) = \int\int \bar{\bar{\epsilon}}_{i,j}(\vec{r},\vec{r}\,',t,t')\vec{E}_j(\vec{r}\,',t')dt'd\vec{r}\,', \tag{2.6}$$

where $\bar{\bar{\epsilon}}_{i,j}$ is a dielectric tensor. In the frequency domain their relationship is given by [Jac99]

$$\vec{D}_i(\vec{k},\omega) = \bar{\bar{\epsilon}}_{i,j}(\vec{k},\omega)\vec{E}_j(\vec{k},\omega). \tag{2.7}$$

The charge density in the Coulomb's law Eq.(2.1) has two components [Jac99]

$$\rho = \rho_{ext} + \rho_{pol}, \tag{2.8}$$

where ρ_{ext} is the external charge density and ρ_{pol} is the bound charge density, which is due to the polarization [Jac99]:

$$\rho_{pol} = -\nabla \cdot \vec{P}. \tag{2.9}$$

In the conducted experiment an electromagnetic wave was projected onto a sample. The electric field inside the sample rearranges the charge distribution and induced polarization $\vec{P}$. It is important to find the relationship between the induced polarization, which relates to the measured transfer function of a sample (Appendix A), to the interesting material parameters, e.g. dielectric function.

In a general case, the polarization is not necessarily proportional to the applied electric field, like in nonlinear media. The dependence of the electric polarization $\vec{P}$ on the electric field $\vec{E}$ (if the field is weak) is given by the Taylor expansion [ST07]:

$$P_i = \sum_j \chi^{(1)}_{ij} E_j + \sum_{j,k} \chi^{(2)}_{ijk} E_j E_k + ... \tag{2.10}$$

where $\chi^{(\alpha)}_{ij..}$ is a nonlinear susceptibility. For linear media $\vec{P} = \chi\vec{E}$.

The second order expansion describes the Pockel's effect (see section 3.3.1). For further considerations we take only the first term of the expansion into account, and even more, we assume the media is linear. For the investigated material, PEDOT:PSS, we assume that it is homogeneous (*1), linear and isotropic, so that the displacement vector $\vec{D}(\vec{r},t)$ is proportional to the electric field $\vec{E}(\vec{r},t)$. These assumptions follow that $\bar{\bar{\epsilon}}_{i,j}$ is a complex scalar ϵ (*2). The displacement vector is equal to [DG02]:

$$\vec{D}(\vec{k},\omega) = \epsilon(\vec{k},\omega)\vec{E}(\vec{k},\omega) = (1+4\pi\chi)\vec{E}(\vec{k},\omega) = \vec{E}(\vec{k},\omega) + 4\pi\vec{P}(\vec{k},\omega), \tag{2.11}$$

χ is the electric susceptibility.

In analogy to the relationship between the displacement vector and the electric field Eq.(2.7), we can derive the relation between the current and the electric field, additionally we assume that there is a local relationship between the given quantities, but their variation in space is identical and therefore their ratio does not depend on position (*3) [DG02].

$$\vec{D}(\vec{r}) = \hat{\epsilon}\vec{E}(\vec{r}), \tag{2.12}$$

$$\vec{J}(\vec{r}) = \hat{\sigma}\vec{E}(\vec{r}). \tag{2.13}$$

Thus in the frequency domain both quantities are independent of the wavevector. It follows [DG02]:

$$\hat{\epsilon}(\omega) = \epsilon_1(\omega) + \epsilon_2(\omega), \tag{2.14}$$

$$\hat{\sigma}(\omega) = \sigma_1(\omega) + \sigma_2(\omega). \tag{2.15}$$

From the Maxwell's equations follows the relationship between the complex conductivity and the complex dielectric function [DG02]:

$$\hat{\epsilon} = 1 + \frac{4\pi i}{\omega}\sigma, \tag{2.16}$$

$$\hat{\epsilon} = \epsilon_1 + \frac{4\pi i\sigma_1}{\omega}, \tag{2.17}$$

where $\vec{D} = \hat{\epsilon}\vec{E}$. ϵ_1 describes the phase shift of the electromagnetic wave caused by the media and $\epsilon_2 = \frac{4\pi i\sigma_1}{\omega}$ is the change in magnitude, of the electromagnetic wave when passing through the media.

Additionally, we define a complex index of refraction as a sum of the real refractive index and the extinction coefficient [DG02]:

$$N = n + i\kappa = \sqrt{\epsilon\mu} = \sqrt{\epsilon}, \tag{2.18}$$

where the real index of refraction gives the relationship between the phase velocity of electromagnetic wave in a material and speed of light in vacuum $v_{ph} = \frac{c}{n}$.

We assume there are no magnetoresistive effects in PEDOT:PSS. Thus the permeability is $\hat{\mu} = 1 + 0i$ (*4).

To summarize, here are the assumptions (*) for material parameter derivation.

1. sample is homogeneous
2. sample is linear
3. sample is isotropic
4. PEDOT:PSS's permeability is $\hat{\mu} = 1 + 0i$ (*4)

   This assumption is valid if length scales of interest, e.g. electron mean free path, are larger that the boundary conditions of the problem. However, in

the discussed experiment, the focus of the laser spot, defining the boundary conditions, is approximately 104 μm, where the localization lengths of electrons in PEDOT:PSS are in the order of 50 nm [Nar07]. For this reason we can assume $\hat{\epsilon}(\vec{r}) = \hat{\epsilon}$ and $\hat{\sigma}(\vec{r}) = \hat{\sigma}$

2.2 Conduction models

In this section the mechanism describing conduction will be discussed? A simplified phenomenological approach to understand the electrical conduction provides the Drude Model, which was proposed by Paul Drude [Dru00] to explain the transport properties of electrons in metals. Electrodynamic response of a material consists of intraband and interband transitions. The first are optical transitions between states in a partially filled band, while interband transitions occur between different bands. The Drude Model describes the contribution of a free electron gas, thus transitions occurring in a partially filled band of metals - intraband transitions [Deg06].

2.3 Drude model

The Drude theory of metallic conduction, which was presented at the beginning of the twentieth century [Dru00], shows an approach to explain how materials conduct electricity based on the kinetic theory of gases. In this theory a metal is considered to be a gas composed of electrons. These electrons are valence electrons of an atom. Only they form an electron gas, as positively charged ions are considered immobile. This situation is presented schematically in Fig.2.1. Each atom of an atomic number Z_a has Z_a electrons with a total charge $-eZ_a$, where $e = 1.60 \cdot 10^{-19}\ C$ is the electron charge. A part Z of these electrons are weakly bound and are the valence electrons, they detach from the atom and become conduction electrons in the electron gas. The rest $Z_a - Z$ are core electrons and are strongly bound to the nucleus. They don't participate in the conduction process.

There are two major assumptions concerning electron behavior:

1. electrons are independent

2. electrons are free

The first assumption says that electrons don't interact with other electrons (no electron-electron interaction). Due to the second assumption there is no interaction with positively charged ions (no electron-ion interaction). The electric field produced by both electrons and ions is neglected.

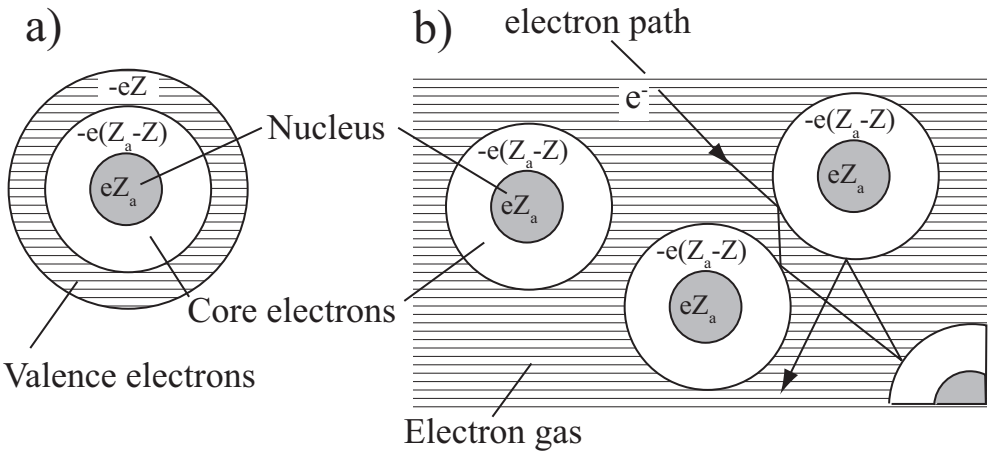

Figure 2.1: Drude conduction model [AM76]: a) an isolated atom b) the nucleus and the ion core of an atom is immobile, valence electrons form electron gas.

Electrons, as gas particles in the kinetic theory of gases, are treated as identical solid spheres. Their motion is governed by Newton's laws. The electron equation of motion has a form Eq.(2.19) [AM76]:

$$\frac{d\vec{p}(t)}{dt} = -\frac{\vec{p}(t)}{\tau} + \vec{f}(t), \tag{2.19}$$

where $\vec{p}(t)$ is electron's momentum.

The first term originates from the Newton's law, the second is a damping and the third is a driving force.

Electrons move uniformly on straight lines until they collide with other electrons or with ions. Collisions are instantaneous and occur with a probability $1/\tau$ per unit time, which means that an electron will travel on average for τ until the next collision. τ is called a relaxation time. The electron velocity after collision does not depend on the velocity before collision. It depends only on the local temperature. For higher temperatures the electron speed after collision is higher [AM76].

2.3.1 Conductivity of solids in the Drude model

Important for interpretation of THz data is the electromagnetic response of an investigated material. The Drude model provides an useful approach for such interpretation.

DC Conductivity

When no external electric field is present, electrons will have random velocity, evenly distributed in all directions, thus the net velocity will be zero. There is no

current flow in this case. In the presence of an external electric field $\vec{E}$ electrons will be accelerated under its influence and thus acquire an additional velocity $\frac{-e\vec{E}t}{m}$. The average time an electron travels between collisions is τ, it is the time it takes the system to reach equilibrium. The average velocity of the electron gas is given by [AM76]:

$$\vec{v}_{ave} = \frac{e\vec{E}\tau}{m}. \tag{2.20}$$

Current density is parallel to the electron velocity. When n electrons per unit volume travel with an average velocity $\vec{v}_{ave}$ then in the total charge $-en\vec{v}_{ave}$ crosses in time a unit area perpendicular to the direction of electron flow, which is a current density $\vec{j}$, thus [AM76]

$$\vec{j} = en\vec{v}_{\text{ave}}. \tag{2.21}$$

Substituting Eq.(2.20) to (2.21) gives a general expression for DC conductivity σ_0 in the Drude model [AM76]:

$$\vec{j} = (\frac{e^2 n\tau}{m})\vec{E} = \sigma_0\vec{E}, \tag{2.22}$$

$$\sigma_0 = \frac{e^2 n\tau}{m}. \tag{2.23}$$

AC Conductivity

Solving the electron equation of motion Eq.(2.19) with the above assumptions under the influence of a time dependent electric field $\vec{E}(t) = \vec{E}_0 \exp(-i\omega t)$ leads to the frequency dependence of conductivity [AM76]:

$$\hat{\sigma}(\omega) = \frac{e^2 n\tau}{m}\frac{1}{1-i\omega\tau} = \frac{\sigma_0}{1-i\omega\tau} = \frac{\omega_p^2}{4\pi}\frac{1}{1/\tau - i\omega}. \tag{2.24}$$

Let $\hat{\sigma}(\omega) = \sigma_1(\omega) + i\sigma_2(\omega)$ where $\sigma_0 = \frac{e^2 n\tau}{m} = \frac{1}{4\pi}\omega_p^2\tau$.

$$\sigma_1(\omega) = \frac{\omega_p^2\tau}{4\pi}\frac{1}{1+\omega^2\tau^2}, \tag{2.25}$$

$$\sigma_2(\omega) = \frac{\omega_p^2\tau}{4\pi}\frac{\omega\tau}{1+\omega^2\tau^2}, \tag{2.26}$$

the ω_p is called a plasma frequency. It is the frequency at which the real part of the dielectric function vanishes $\omega_p = 0$. At the plasma frequency the material changes it optical properties from these of a metal to insulator [Dre].

Integration of $Re(\hat{\sigma})$ over all frequencies

$$\int_0^\infty \sigma_1(\omega)d\omega = \int_0^\infty \frac{\omega_p^2}{4\pi}\frac{d(\omega\tau)}{1+(\omega\tau)^2} = \frac{\omega_p^2}{4\pi}\arctan(\omega\tau)|_0^\infty = \frac{\omega_p^2}{8}. \tag{2.27}$$

From the relationship between the complex dielectric function and complex conductivity Eq.(2.16) derived in chapter 2.1 we get an expression for the complex frequency dependent dielectric function $\epsilon(\omega)$ [AM76]:

$$\hat{\epsilon}(\omega) = 1 - \frac{\omega_p^2}{\omega^2 - i\omega/\tau}. \tag{2.28}$$

The real and imaginary parts are equal to

$$\epsilon_1(\omega) = 1 - \frac{\omega_p^2}{\omega^2 + \tau^{-2}}, \tag{2.29}$$

$$\epsilon_2(\omega) = \frac{1}{\omega\tau}\frac{\omega_p^2}{\omega^2 + \tau^{-2}}. \tag{2.30}$$

The for THz spectroscopy interesting optical material parameters, ϵ_1, ϵ_2, σ_1, σ_2 can be characterized by the plasma frequency ω_p and the relaxation time τ.

2.3.2 Optical properties

The optical properties determine the frequency dependence of optical conductivity $\hat{\sigma}$ and complex dielectric function $\hat{\epsilon}$. To better understand the predictions of the Drude model in the Figure 2.2 are plotted $\hat{\sigma}$ and $\hat{\epsilon}$ for THz frequencies and for exemplary values of plasma frequency $\nu_p = \frac{\omega_p}{2\pi} = 30$ THz and relaxation rate $\gamma = 1/2\pi\tau = 0.5$ THz. Later on we will compare the experimental data with the here presented Drude response.

Depending on the frequency range there are three main regions of optical behavior.

$$\begin{cases} \omega \ll 1/\tau \\ 1/\tau \ll \omega \ll \omega_p \\ \omega_p \ll \omega \end{cases}$$

The extinction coefficient κ indicating absorption (see chapter 2.1 for details) is given by

$$k = \frac{1}{2}\sqrt{\sqrt{\epsilon_1^2 + (\frac{4\pi\sigma_1}{\omega})^2} - \epsilon_1} \tag{2.31}$$

and can also be approximated in each regime.

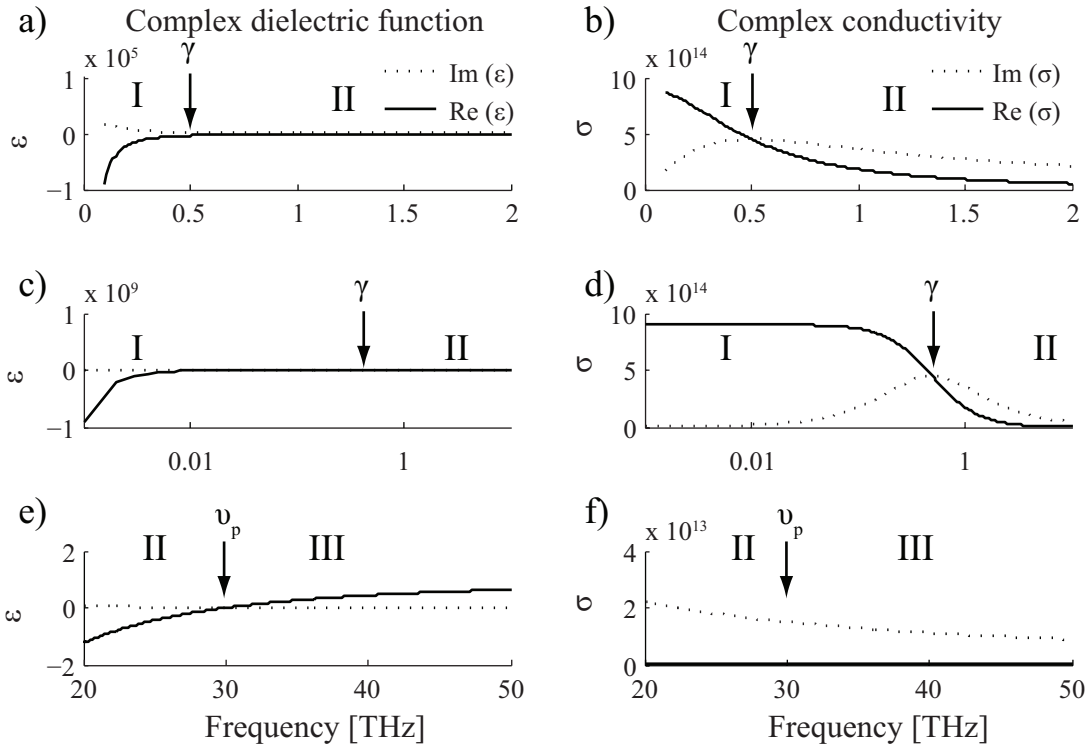

Figure 2.2: Frequency dependence of dielectric function and conductivity in Drude model Plots a) and b) show a low frequency behavior in the range of scattering rate $\gamma = 1/2\pi\tau$. Plots c) and d) are a logarithmic representation of $\hat{\epsilon}$ and $\hat{\sigma}$, with visible dominance of DC behavior. e) and f) show the frequency regime above plasma frequency. Re($\hat{\epsilon}$) changes sign and approaches 1. Regions I, II and III are referred to in text.

Low frequency regime

The first (I in Fig.(2.2)), low frequency region, also referred to as the Hagen-Rubens regime is defined by $\omega\tau \ll 1$ [DG02]:

$$\sigma_1(\omega) = \sigma_0, \tag{2.32}$$

$$\sigma_2(\omega) = \sigma_0\omega\tau, \tag{2.33}$$

$$\epsilon_1(\omega) = 1 - \omega_p^2\tau^2 = 1 - 4\pi\tau^2\sigma_0, \tag{2.34}$$

$$\epsilon_2(\omega) = \frac{\omega_p^2\tau}{\omega}, \tag{2.35}$$

$$\kappa(\omega) = \sqrt{\frac{2\pi\sigma_0}{\omega}} \gg 1, \tag{2.36}$$

The real part of conductivity and dielectric function are dominated by the DC conductivity σ_0. The imaginary part of conductivity grows linearly with frequency, while the imaginary part of $\hat{\epsilon}$ decays with ω^{-1}. The scattering rate determines the peak of $\mathrm{Im}(\hat{\sigma_0})$ and change of the dielectric behavior.

Relaxation regime

The relaxation regime covers the spectral range determined by both crucial quantities plasma frequency and scattering rate $1/\tau << \omega << \omega_p$. The behavior of $\hat{\sigma}$ and $\hat{\epsilon}$ is shown as II in the diagram Fig.2.2. In this regime the conductivity $\sigma_1(\omega)$ decreases with ω^{-2}. It follows [DG02]:

$$\sigma_1(\omega) = \frac{\sigma_0}{\omega^2\tau^2}, \tag{2.37}$$

while $\sigma_2(\omega)$ decreases with ω^{-1}.

$$\sigma_2(\omega) = \frac{\sigma_0}{\omega\tau}, \tag{2.38}$$

$$k(\omega) = \frac{\omega_p}{\omega}. \tag{2.39}$$

The real part of the dielectric function also decreases with ω^{-2}, the imaginary part with ω^{-3}.

$$\epsilon_1(\omega) = 1 - \frac{\omega_p^2}{\omega^2}, \tag{2.40}$$

$$\epsilon_2(\omega) = \frac{\omega_p^2}{\omega^3\tau}. \tag{2.41}$$

Transparent regime

For lower frequencies electromagnetic radiation penetrates the metal only to a certain depth, called the skin depth. At the plasma frequency ω_p the reflectivity drops and the material becomes transparent for electromagnetic waves with $\omega >> \omega_p$. Here are approximate expressions describing conductivity and dielectric response. The character of conductivity behavior stays the same [DG02]:

$$\sigma_1(\omega) = \frac{\sigma_0}{\omega^2\tau^2}, \tag{2.42}$$

$$\sigma_2(\omega) = \frac{\sigma_0}{\omega\tau}. \tag{2.43}$$

The real part of the dielectric constant changes sigh to positive at

$$\omega = \sqrt{\omega_p^2 - (1/\tau)^2}, \tag{2.44}$$

approaches a constant value 1 for high frequencies.

$$\epsilon_1(\omega) \to 1, \tag{2.45}$$

$$\epsilon_2(\omega) = \frac{1}{\omega\tau}\frac{\omega_p^2}{\omega^2 + \tau^{-2}}. \tag{2.46}$$

For high frequencies $\frac{4\pi\sigma_1}{\omega} \ll 1$ therefore $\kappa \to 0$, which means that the material does not absorb energy from the incident radiation.

2.3.3 Temperature dependent conductivity in the Drude model

Temperature dependent measurements reveal information about charge transport. Therefore changes of conductivity and dielectric function with temperature have to be accounted for.

The plasma frequency defined as $\omega_p = \sqrt{4\pi ne^2/m}$ shows a temperature dependence due to volumetric expansion [CWLT00]

$$\omega_p = \omega_{p0}\frac{1}{\sqrt{1 + \alpha(T - T_0)}}, \tag{2.47}$$

where T_0 is a room temperature taken for reference and α the expansion coefficient.

As electron-electron and electron-phonon scattering have been neglected, the only mechanism left for electrons to achieve thermal equilibrium is through collisions: $\frac{1}{2}m\langle v^2\rangle = \frac{3}{2}k_BT$. However, the relaxation time was assumed to be velocity independent [AM76].

To extend the Drude model, the electron mass m in equation (2.23) will be replaced by the effective mass m^*. The effective mass m^* is effectively a mass an electron has when moving, as given by the Newton's laws of motion, in the band structure of a material. It accounts for the effect of interactions with atoms in the lattice, then:

$$\sigma_0 = \frac{e^2 \tau n}{m^*}. \tag{2.48}$$

The conductivity depends on the relaxation time. For increasing temperature the relaxation times shortens, which results in decreasing conductivity.

To further extend the model and to consider the temperature dependence of the electromagnetic response, it is necessary to extend the Drude model on the previously neglected scattering mechanisms, which lead to heat exchange via electron-electron and electron-phonon scattering.

Let us introduce a collision frequency ω_c. Now let ω_{cp} be a contribution from the electron-phonon scattering and ω_{ce} from electron-electron scattering.

According to Holstein [Hol54], [Hol64] and Lawrence [Law76], [CWLT00] it holds

$$\omega_{cp}(T) = \omega_0[\frac{2}{5} + 4(\frac{T}{\Theta})^5 \int_0^{\frac{T}{\Theta}} \frac{z^4 dz}{\exp(z) - 1}], \tag{2.49}$$

where Θ is Debye temperature and ω_0 is a constant determined in a static limit and

$$\omega_{ce}(T) = \frac{1}{12}\pi^3 \frac{\Gamma\Delta}{\hbar E_F}[(k_B T)^2 + (\hbar\omega/2\pi)^2]. \tag{2.50}$$

E_F is the Fermi energy, k_B the Boltzmann constant, Γ a constant averaging the scattering probability over the Fermi surface, and Δ the fractional umklapp scattering. However, a detailed analysis of metallic behavior exceeds the frame of this work, as the focus is on semiconducting polymers.

In semiconductors the temperature dependence of the charge carrier mobility is given by [SKSM02]:

$$\mu(T) = \mu_0 T^{-\alpha}, \tag{2.51}$$

where $\alpha = 3/2$ for scattering on acoustical phonons and $\alpha = 1/2$ for scattering on optical phonons, μ_0 is mobility at a reference temperature. For lower temperatures the scattering on phonons descreases, therefore the charge carrier mobility oncreases. The conductivity depends linearly mobility $\sigma = en\mu$, therefore the conductivity in band conduction increases for decreasing temperature.

2.3.4 Semiclassical Drude model

The above derivation of the Drude model is based on an assumption that electrons behave like identical solid spheres [Dru00]. Let us now consider electrons as

quasiparticles, so influenced by the interaction with the solid, which is accounted for in the effective mass. The effective mass m^* is usually different from the mass of a free electron. Let $f(\vec{p},\vec{r})$ be a non-equillibrium distribution function, which is the average occupation number for the state $\vec{p}$ at point $\vec{r}$. The Boltzmann transport equation (2.53), when applied to metals, describes the statistical distribution of electrons [Gal]:

$$\frac{\partial f}{\partial t} + \vec{v}\frac{\partial f}{\partial \vec{r}} - e(\vec{E} + \frac{1}{c}[\vec{v} \times \vec{H}])\frac{\partial f}{\partial \vec{p}} = -\frac{f - f_0}{\tau}, \tag{2.52}$$

where f is the distribution function and f_0 is the distribution function at equilibrium and τ is the relaxation time. For stationary fields the Boltzmann equation takes a form [Gal]:

$$-e\vec{E}\frac{\partial f}{\partial \vec{p}} = -\frac{f - f_0}{\tau} = -\frac{f_1}{\tau}. \tag{2.53}$$

The electron distribution is governed by the Fermi-Dirac statistics:

$$f(E) = \frac{1}{\exp\left(\frac{E-\mu}{kT}\right) + 1}, \tag{2.54}$$

where E is the energy of a single particle state, μ is the chemical potential, k_B is the Boltzmann constant and T the temperature in K. A short calculation shows that the DC conductivity derived from the Boltzmann equation has a form [Kit96]:

$$\sigma_0 = \frac{ne^2\tau}{m^*}, \tag{2.55}$$

which is up to the mass m exactly the same as the Drude formula in the classical approximation Eq.(2.23). For a time dependent electric field $\vec{E}(\vec{r},t) \propto \exp(-i\omega t)$ we obtain the expression for the AC conductivity [Gal]:

$$\sigma(\omega) = \sigma_0 \frac{1}{\langle\tau\rangle}\left\langle \frac{\tau}{1 - i\omega\tau} \right\rangle. \tag{2.56}$$

The terms $\langle\cdot\rangle$ in Eq.(2.56) denote expectation values.

Drude Smith model

Let us now consider a model of electric behavior introduced by Smith in 2001 [Smi01], the Drude Smith model (DSM), which is an extension to the described classical Drude model [Dru00]. It describes conductivity of materials with charge carrier localization due to inhomogeneity and disorder on the nano-scale [ABK+06].

Further DSM will be applied to explain the electric properties of PEDOT:PSS, as PEDOT:PSS is known to have localized states [Nar07].

Consider an electron system with a unit impulse of electric field applied at time $t = 0$. The current $j(t)$ decays exponentially to equilibrium with a relaxation rate τ, thus there is

$$j(t)/j(0) = \exp(-\frac{t}{\tau}), \tag{2.57}$$

the complex conductivity is the Fourier transform of the current density $j(t)$, thus

$$\hat{\sigma}(\omega) = \int_0^\infty j(t) \exp(i\omega t) dt, \tag{2.58}$$

which leads to the Drude formula [AM76]:

$$\hat{\sigma}(\omega) = \frac{\sigma_0}{1 - i\omega\tau} \tag{2.59}$$

The Drude Smith model is based on an assumption that an electron has a memory of velocity from previous collisions [Smi01]. The velocity memory or the so called persistence velocity is described by the Poisson distribution. The same as in the Drude formula τ is the average time between consecutive collisions. Thus, as given by the Poisson distribution, in the time interval $[0, t]$ an electron will experience n collisions with the probability [Smi01]:

$$p_n(0, t) = (\frac{t}{\tau})^n \frac{\exp(-\frac{t}{\tau})}{n!} \tag{2.60}$$

Now assume that after each n_{th} collision a fraction c_n of electron's velocity is retained. This is the difference to the conventional Drude model, where a charge carrier does not have any velocity related memory. In the classical Drude model $c_n = 0$ for all $n > 0$. Therefore the current density in DSM is given by [Smi01]:

$$j(t)/j(0) = \exp(-\frac{t}{\tau})[1 + \sum_0^\infty \frac{c_n(\frac{t}{\tau})^n}{n!}]. \tag{2.61}$$

Again, the Fourier transformation gives the complex conductivity in the DSM, which accounting for the persistence velocity is equal to [Smi01]:

$$\hat{\sigma}_{DSM}(\omega) = [\frac{\sigma_0}{1 - i\tau\omega}][1 + \sum_{n=1}^\infty \frac{c_n}{(1 - i\tau\omega)^n}]. \tag{2.62}$$

Smith suggested [Smi01] considering only terms $n = 1$ for the case of single scattering. It means that only the velocity from the last collision influences the velocity after collision. For elastic collisions the persistence velocity coefficient $c_1 = \langle \cos\theta \rangle$ is the expectation value of the cosine of the scattering angle θ. Thus, the values of c_1 are allowed in the range $[-1, 1]$. Negative values of persistence velocity parameter $c_1 = -1$ mean, that the carrier undergoes backscattering

or localization [ABK+06]. Fig.2.3 shows the frequency dependence of complex conductivity for negative and positive values of c_1 in comparison with the Drude model $c_1 = 0$. For strong backscattering effects, when $c_1 = -1$, the charge carrier behavior in the Drude Smith Model is significantly different from the classical behavior. For values of c_1 close to -1 the real part of conductivity displays a maximum at [Smi01]

$$\omega_{max} = \frac{\sqrt{\frac{3c_1+1}{c_1-1}}}{\tau} \tag{2.63}$$

In the Drude model $\mathrm{Re}(\hat{\sigma}_{\mathrm{Drude}})$ falls monotonously after reaching maximum at $\sigma(\omega = 0) = \sigma_{DC}$, wheras $\mathrm{Re}(\hat{\sigma}_{\mathrm{DSM}})$ has a maximum at $\omega > 0$. Also for $c_1 = -1$ the imaginary part $\mathrm{Im}(\hat{\sigma})$ shows different behavior: in DSM $\mathrm{Im}(\hat{\sigma}_{\mathrm{DSM}})$ is large and positive, unlike the classical Drude model, where it is large and negative.

Drude Smith Model, although it is a relatively simple generalization of the phenomenological Drude Model, has provided explanation of the behavior of liquid mercury, with the persistence velocity parameter $c_1 = 0.49$, and the quasicrystal $Al_{63.5}Cu_{24.5}Fe_{12}$ with $c_1 = -0.973$ [Smi01].

2.4 Charge transfer mechanisms disordered systems

In materials with a conductivity having a finite value at low temperatures, like metals and highly doped crystalline semiconductors, conductivity depends on the electrons with energies neat the Fermi surface [MD71]. Thus, the conductivity depends on the mobility of these electrons.

Intermolecular electronic interactions in conjugated polymers are weak and the polymer structure is disordered. Thus, charge transport between chains in mostly dominated by hopping conductivity, while in conventional semiconductors by band transport. Hopping conduction increases with increasing temperature, the mobility dependence on temperature is given by Eq.(2.64). The activation energy is approximately $0.3 - 0.5$ eV [Bru08].

$$\mu(T) \propto \exp\left(-E/k_B T\right). \tag{2.64}$$

Hole mobility in a disordered hopping system shows according to [BKN+08] a dependence

$$\mu(T) \propto T^{-2}. \tag{2.65}$$

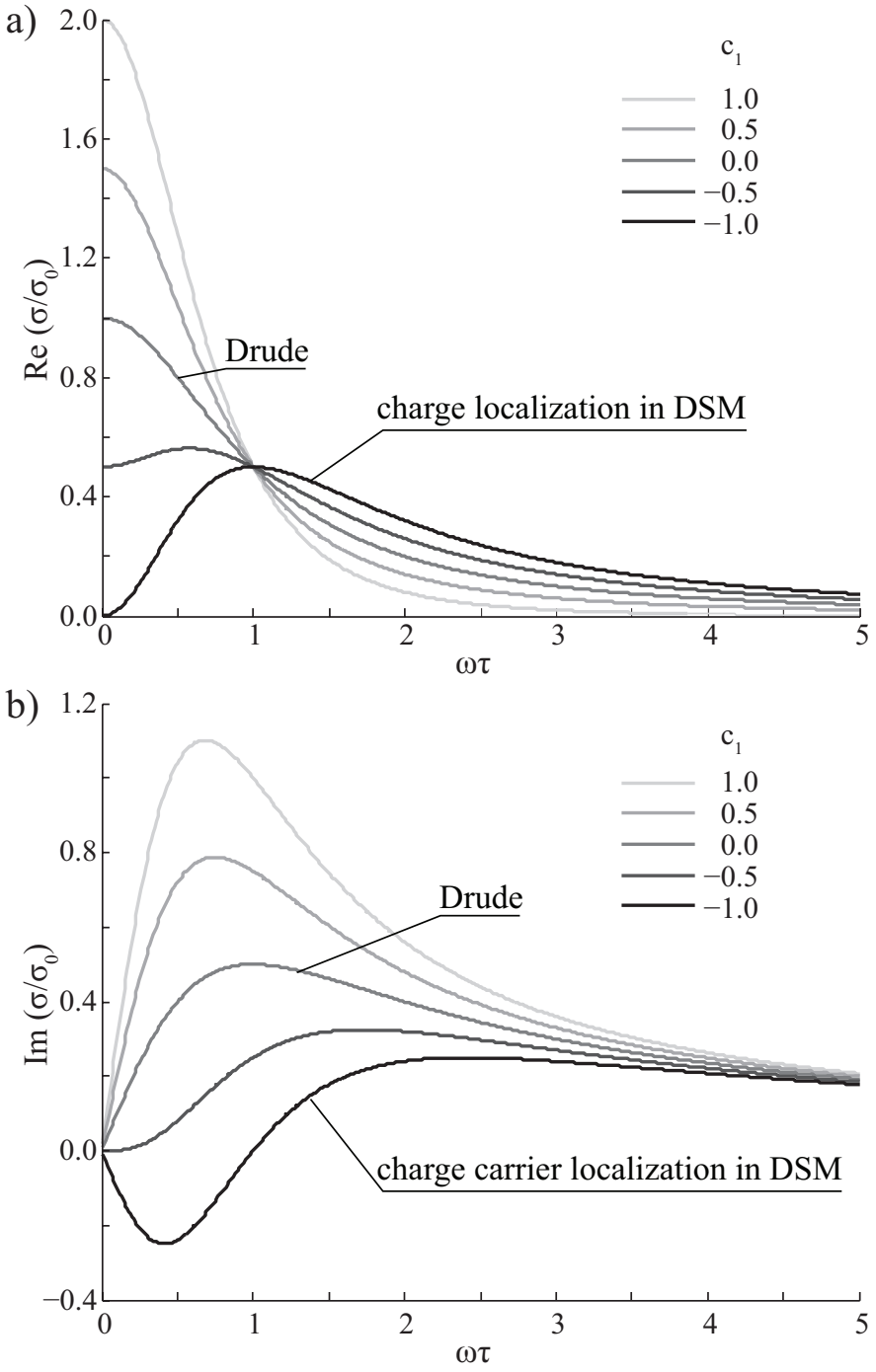

Figure 2.3: a) Real conductivity and b) Imaginary conductivity in Drude Smith Model plotted for different values of persistence velocity coefficient c_1. For $c_1 = 0$ is the classical Drude Model, for $c_1 = -0.5\ -1$ the case of carrier localization or backscattering

2.4.1 Variable range hopping

Charge transport in amorphous materials is different than in solids with a periodic lattice. Anderson [And58] introduced a concept of localized states in amorphous materials. These states 'trap' electrons, are localized at random positions and each state has a random potential. Electrons can move between these trapping centers with a certain probability. Electron movement can be characterized as random walk between states, where a step/jump from one site to another takes place with a certain probability. When moving from one center to another an electron absorbs or emits a phonon. Therefore electrons in this conduction process need a certain activation energy ΔE. Such a from of charge transport in amorphous solids was introduced by Mott and Davis [MD71] to describe impurity conduction and is called thermally activated hopping.

In band conduction, dominant in ordered systems, carrier mobility increases with decreasing temperature. This is due to lower rate of electron-phonon scattering at lower temperatures and increased electron mean free path. In disordered systems, like materials with high impurity grade or polymers, when electron mean free path is comparable with a lattice constant, hopping conduction becomes the dominant condution process. In hopping conduction carrier mobility increases with increasing temperature, because hopping is thermally activated.

A general form of the temperature-dependent conductivity of the variable range hopping conduction is [MD71]

$$\sigma(T) = \sigma_0 \exp[(-\frac{\Delta E}{kT})^{\frac{1}{1+D}}], \tag{2.66}$$

where D is a dimensionality of a system and can have values: 1, 2 or 3. Further, hopping is also responsible for AC conductivity. The model can be extended to describe alternating conductivity at a given frequency ω [DGBZ89], which is

$$\sigma_{\mathrm{AC}} = \sigma^{'}(\omega) + \sigma_{\mathrm{DC}} \tag{2.67}$$

$\sigma^{'}(\omega)$ is a polarization conductivity and is also the quantity measured in a THz experiment. σ_{DC} is a conductivity for direct current.

Following Mott [MD71] the polarization conductivity depends on temperature in the following way

$$\sigma^{'}(\omega) = A(T)\omega^{s} \tag{2.68}$$

where $A(T)$ and s are parameters characteristic for a material and are determined experimentally.

A hop of length R between two localized states can be thermally activated, in this case it is called correlated barrier hopping CBH or through when hops occur via tunneling - quantum mechanical tunneling QMT [DGBZ89].

The main difference between these two mechanisms is the way electrons cross the potential barrier between two localized states. In the CBH crossing of the potential barrier between localized states is thermally activated. It follows that s in Eq. (2.68) shows a temperature dependence. In CBH the potential barrier between localized centers depends on the their distance R. Localized center distribution in isotropic and homogeneous.

It can be shown [DGBZ89] that s depends on temperature in the following way

$$s = 1 - \frac{6k_BT}{W_M + k_BT\ln(\omega\tau_0)}, \tag{2.69}$$

where k_B is the Boltzmann constant, T - temperature, W_M - energy necessary to bring an electron from infinity to the localized center, τ_0 - relaxation time.

Equation (2.69) excludes a possibility of s having a constant value for different temperatures, particularly for T varying in the range from 4 K to 320 K .

In the second mechanism, in the QMT model, proposed by Pollak and Geballe [PG61], electron transitions between localized states occur by tunneling through a potential barrier separating these states. The relaxation time does not depend on temperature but on the hopping distance R. The frequency dependence of the polarization conductivity is given by

$$\sigma^{'}(\omega) = A(T)\omega[\ln(\frac{1}{\omega\tau_0})]^4. \tag{2.70}$$

2.5 Hopping conduction in PEDOT:PSS

A dominant charge transfer mechanism in a conducting polymer PEDOT:PSS for DC fields is hopping conduction [Nar07]. Localized states in PEDOT:PSS are due to structural disorder (3.6) and energetic disorder. DC temperature dependence of PEDOT:PSS coatings has already been reported by [AHO05] with a four-probe measurement and by Nardes [Nar07] . Where Nardes reports conductivity of Baytron P VP Al 4083 from H. C. Starck, the same as investigated in this work, determined in two and four terminal measurements.

In both works [AHO05], [Nar07] it is reported that PEDOT:PSS charge transport is caused by variable range hopping conduction. DC conductivity, as it has been measured, is described by the equation (2.66).

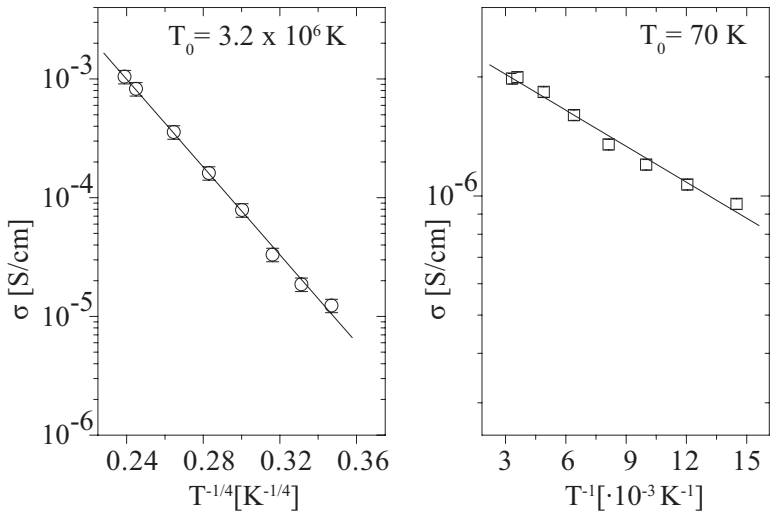

Figure 2.4: Conductivity of PEDOT:PSS reported by Nardes [NKJ07]. Temperature dependence of the conductivity of PEDOT:PSS thin films plotted vs $T^{-1/4}$ (left) and vs T^{-1} (right). Conductivity is fitted to VRH see Eq.(2.66).

Chapter 3

Experimental methods

In this chapter we will give details on sample preparation and experimental methods used to investigate properties of PEDOT:PSS:

- for microstructure characterization we used Atomic Force Microscopy
  - to learn about films morphology and thickness
- to investigate the charge transfer mechanism we used Time Domain Terahertz Spectroscopy (TD-TS)
  - to learn about the frequency dependent dielectric function, the optical conductivity and the refractive index in the THz domain.

3.1 Sample preparation

For sample preparation a water solution of PEDOT:PSS was used. It was manufactured by H.C. Starck and called CLEVIOS P VP AI 4083. The ratio of PEDOT to PSS content is 1:6, which is an optimal choice of conductivity (see Tab.1.1) for OLEDs and photovoltaic systems to avoid cross talk effects [Koc07]. Particle size is $80 - 100$ nm.

The sample mounting is presented in a graphic (Fig.3.1). It consists of a Silicon wafer and a decomposed PEDOT:PSS thin film. Approximately a half of the wafer surface is left free for reference measurements.

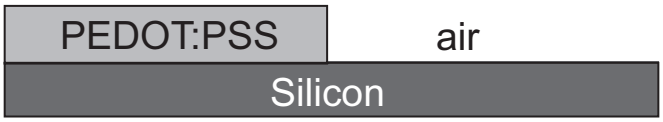

Figure 3.1: PEDOT:PSS sample on silicon substrate.

3.1.1 Preparation process

High ohmic silicon wafers from Wafer Technology were used as substrates for PEDOT:PSS thin films. This type of silicon is appropriate for THz applications due to its high transmittance of THz radiation (see chapter 3.3.3). Wafer before processing were cleaned in an ultrasonic bath with Aceton and Ethanol for 10 minutes. Wafer surface has to be hydrophilic, so that PEDOT:PSS water solution can hold to it during spin coating. To make wafer surface hydrophyllic Silicon was exposed to Ozon atmosphere for 30 minutes. In this process Silicon surface forms bindings with O groups, which in turn can form bindings with water. As a result PEDOT:PSS holds very well on a silicon surface.

Water solution of PEDOT:PSS was spin coated on a Silicon substrate 30 seconds long. Prior to coating the solution was passed through a 0.45 μm filter. The obtained stable dispersion, as a wet coating, was heated immediately after at 150°C for 120 s on a heating plate to remove residual water.

3.1.2 Sample thickness

Three groups of samples concerning sample thickness and homogeneity were prepared and investigated.

- homogeneous thin films in the range $50 - 140$ nm ;
- inhomogeneous thick films in the range $1 - 2$ μm ;
- homogeneous thick films in the range $1.7 - 2.4$ μm.

Homogeneous thin film preparation

The spin coating technique enables decomposition of homogeneous thin films. However, a range of film thicknesses achievable in this way is limited. A higher spin coating speed results in a thinner deposited layer. When the spin coating speed is two low, the water polymer solution does not form a homogeneous layer anymore.

We have prepared samples with PEDOT:PSS layer thickness in the range $50 - 140$ nm with rotation speeds $490 - 2400$ rpm. As an available commercial spin coater was limited to 1200 rpm, which corresponds to 50 nm thickness, in order to obtain thicker samples, for better signal resolution, we have built a spin coater covering the spinning range $490 - 1200$ rpm, corresponding to $50 - 100$ nm.

Samples in the range ≈ 140 nm we obtained with a PEDOT:PSS solution with lower water content (see homogeneous thick film preparation).

Inhomogeneous thick film preparation

A drop of PEDOT:PSS solution was placed on a substrate and dried at room temperature. Thickness of this type of samples varies strongly, which has a huge contribution to THz measurement uncertainty. A comparison of measured THz signals is shown in Fig.3.2. The THz signal of these samples show a significant difference from the reference signal, which means a very good resulution, but huge thickness variation makes this type of samples unsuitable for investigation.

Homogeneous thick film preparation

To achieve larger sample thicknesses during spin coating the water content of the PEDOT:PSS solution was reduced. As a result the solution density increased. In this way, after spin coating and heating, a significantly higher amount of PEDOT:PSS solid content stays on the substrate. The initial and final volumes of solutions used for preparation process are presented in the table Tab.3.1. Using

the modified solutions, with higher PEDOT:PSS concentrations, we were able to manufacture significantly thicker film layers. The thickness values are given in Tab.3.2. The thickness of the PEDOT:PSS layer for all three samples was measured from topography images obtained by AFM. See chapter 3.2 for details.

solution	initial volume [ml]	final volume [ml]	temperature [°C]
1	20.0	13.0	50
2	18.5	2.5	50
3	10.0	1.5	75

Table 3.1: Density of PEDOT:PSS solutions used for sample preparation.

solution	rotations per minute	thickness [nm]
1	6000	140
2	6000	1700
3	1800	2400

Table 3.2: Sample preparation parameters.

In a THz experiment the ratio of two measured signals contains information about electric properties of a material (see appendix A for further reference). These signals are a THz waveform transmitted through a reference (Silicon) and a 2 layer system of PEDOT:PSS and Silicon. To maintain a good measurement accuracy the difference between these two signals should be approximately 30%.

The graphics 3.1 shows a comparison of THz signals of the Silicon substrate used for reference measurements (line), thin 140 nm sample (segment) and a thick (2400 nm) sample (dotted line). All signals were scaled to reference maximum.

Thick samples absorb enough THz radiation (magnitude of signal amplitude decreases), so that the difference between a reference signal and a signal of a sample material is clearly visible. The situation is different for thin samples. Absorption of thin samples is very weak. Amplitudes of both signals under consideration are almost identical. The phase shift between two signals is also small, which makes the difference of both signals comparable with measurement uncertainty. We have concluded that samples with thickness in the range $50 - 140$ nm are too transparent for THz measurements. The sample thickness is an important factor in data evaluation. Its measurement uncertainty is currently the main source of error in THz experiments. For this reason we have decided to consider THz spectra only of two homogeneous samples belonging to group 3.

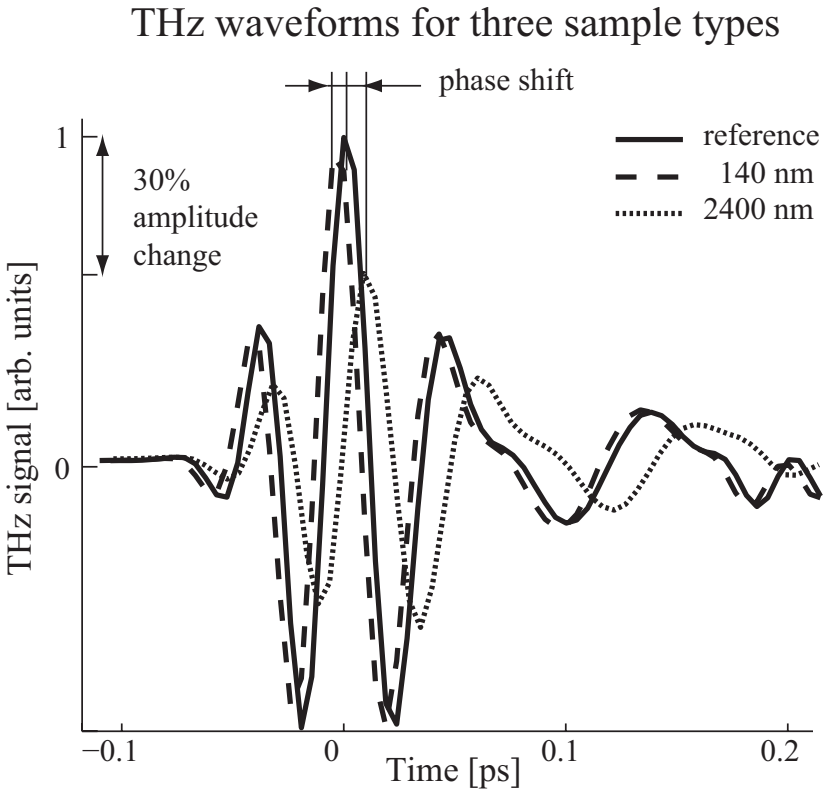

Figure 3.2: Waveforms measured in THz experiments. Solid line represents a waveform transmitted through the silicon substrate. Segment and dotted line stand for waveforms transmitted through two different PEDOT:PSS films. For data processing the amplitude of sample signal should be $\approx 30\%$ lower than that of the reference signal.

3.2 PEDOT:PSS microstructure characterization

Two methods were used to characterize coating thickness: Atomic Force Microscopy (AFM) and Ellipsometry. AFM in Tapping Mode was additionally used to investigate sample morphology in air at room temperature.

3.2.1 AFM measurements

Atomic Force Microscope (AFM) generates a topography map of a surface [HFGR+07]. The measurement is based on an interaction between a sharp cantilever tip, which diameter is in the order of 10 nm. As cantilever approaches the sample surface appearing forces cause the cantilever to deflect, which in turn is registered by the detector (Fig.3.3).

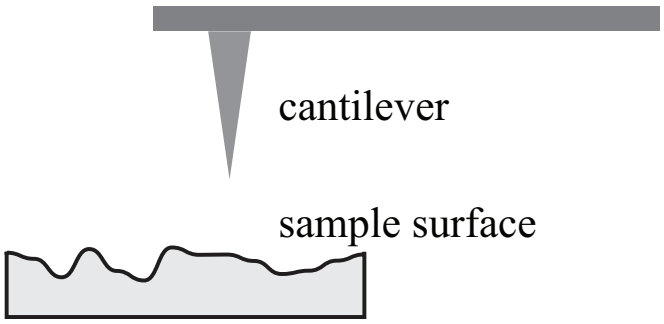

Figure 3.3: AFM setup. Cantilever with a sharp tip approaches sample surface.

The interaction between the sample surface and the cantilever is mostly due to the van der Waals forces (Fig.3.4). As the distance between atoms decreases and reaches a couple angstroms the interatomic force becomes repulsive. When the cantilever is places so 'close' to the sample (in the contact mode), the repulsive force causes the cantilever to deflect, which is in turn detected.

For larger distances, like hundreds of angstroms, the intermolecular force is attractive. Again, cantilever deflection is being measured, when placed within the range of the attractive interaction (non-contact mode).

In the tapping mode the cantilever oscillates above the sample surface with a given frequency and amplitude ≈ 100 nm. The measurement principle is the same as in the contact mode, but due to the oscillations of the cantilever, it does not move along the surface, as in the contact mode, which can damage the sample surface, but oscillates gently. AFM measurements do not depend on the electron density, as for example STM measurements do. Therefore AFM can measure all types of solids.

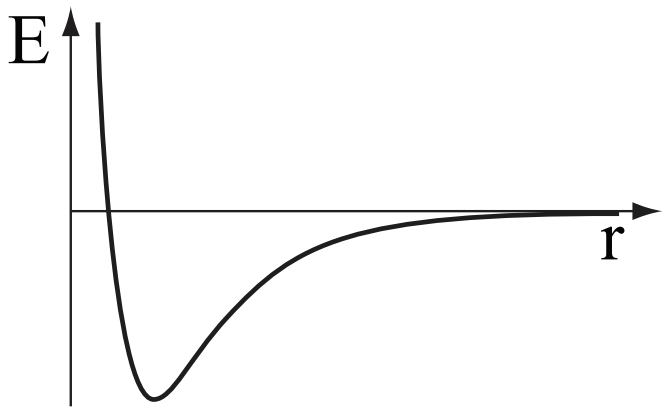

Figure 3.4: Interaction energy between molecules plotted vs. intermolecular distance [HS07].

3.2.2 PEDOT:PSS microstructure

Morphology measurements of three PEDOT:PSS films of different thickness were performed using Nanotec Atomic Force Microscope in tapping modes at room temperature in air. Results were evaluated with Scanning Probe Microscopy Software provided by Nanotec [HFGR$^+$07].

AFM imaging provides information about surface morphology, e.g. height. This property was used to determine PEDOT:PSS film thickness on the silicon substrate. The Silicon surface topography is shown in the picture (Fig.3.5a). The surface roughness is in the order of 2.5 nm, which is negligable in comparison with the measured sample thickness 1700 nm. A height difference between the PEDOT:PSS layer and the substrate surface was measured (Fig.3.5). As surface topographies of PEDOT:PSS and Silicon are different (Fig.3.5c) it is possible to distinguish between these two types of surface and measure the edge difference (Fig.3.5d).

Figure 3.6 shows topography images of three samples. The thickness of each sample is different a) 1700 nm, b) 140 nm, c) 2400 nm. This results from the preparation process. Solution for preparation of each sample had a different density and was dispersed at a different coating speed.

Morphology of all investigated films is uniform. Samples roughness varies from 0.15 nm for sample a) to $2 - 2.5$ nm for samples b) and c). Sample a) was prepared from a thickened solution and spin coated very fast, which might have resulted in this extremely even distribution in comparison to other samples.

Granulated structure previously reported by [SGF07], [Nar07], [NJK08] and [TKT$^+$04] can be identified in all samples. The granulated structure is created during the polymerization process, when PEDOT ogliomers attach to PSS chains and form shell like gel particles. PEDOT is hydrophobic, while PSS is hydrophilic. It results in a formation of small shell agglomerates, with PSS shells, in the water

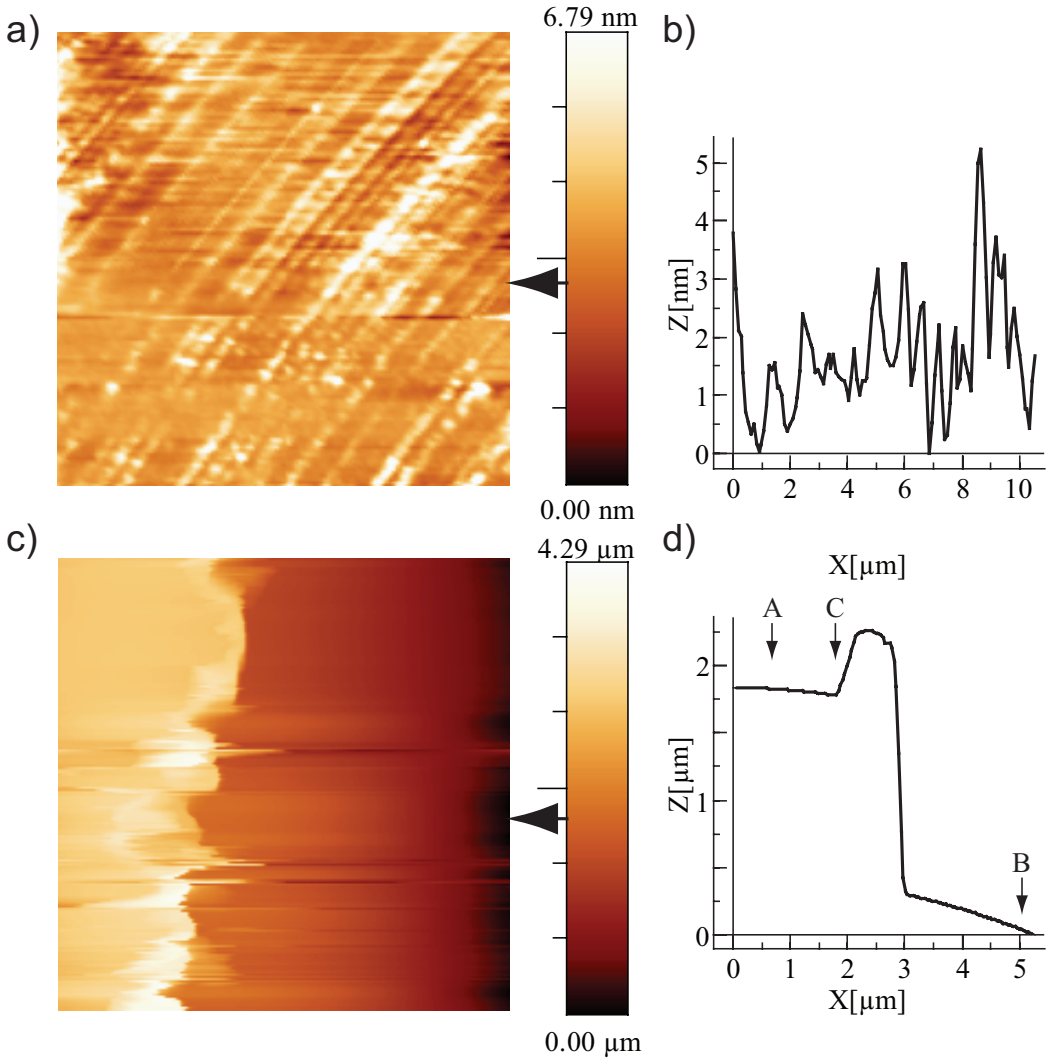

Figure 3.5: Film thickness measurement with AFM. The scan area is 10 μm $\times$ 10 μm. a) Silicon surface b) boundary region: PEDOT:PSS (left), Silicon (right). On the right hand side are roughness profiles of both scanned areas. The x direction is in the sample plane, while the z direction is perpendicular to the sample surface. The film thickness was measured between points A and B. The height variation between points B and C is due to the gathered residual amount of PEDOT:PSS, which was formed, when the sample surface was mechanically scratched to obtain a sharp edge between both materials.

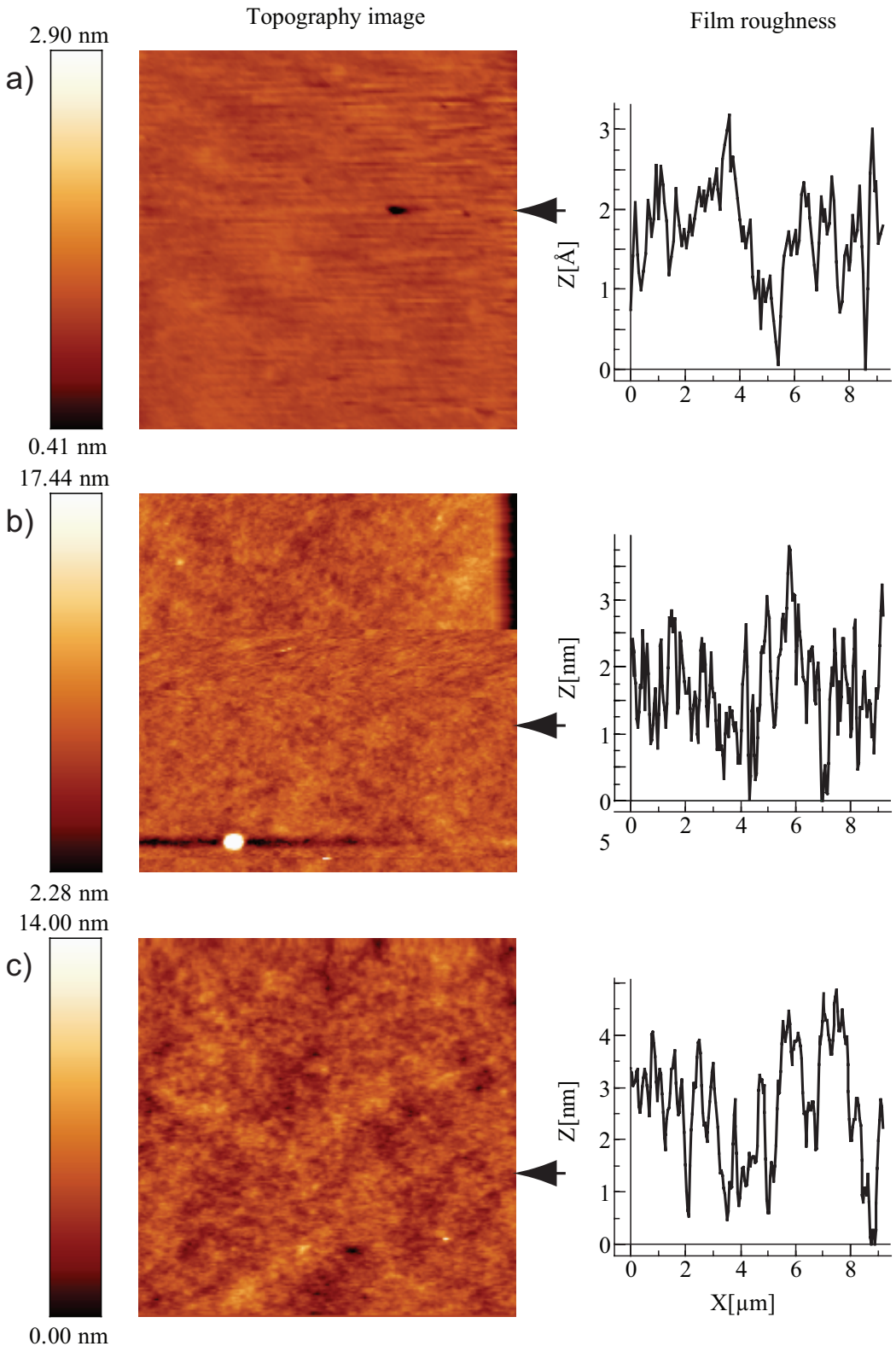

Figure 3.6: AFM topography images of 3 samples with different thickness: a) 1700 nm, b) 140 nm, c) 2400 nm. The scan area is 10 μm $\times$ 10 μm. Roughness profiles of scanned areas in the right hand side. The x direction in plane, the z direction perpendicular to plane.

dispersion. Highly conductive PEDOT-rich domains are separated by insulating PSS-rich domains [Koc07]. If there are excess PSS chains they may exist in the space between gel particles and also on the surface of gel particles, which results in a net negative charge of PEDOT:PSS gel particles [CMO+03].

Phase and topography images of the sample with thickness 2400 nm confirm the presence of gel particles Fig.3.9. AFM phase images are very sensitive to the change of the cantilever tip - sample surface interaction and therefore to the change of surface composition. Two regions in the phase image Fig.3.9 b) can be distinguished. 1) Regions with a high phase contrast, they correspond to PEDOT:PSS shells. 2) Regions with a low phase contrast are voids between gel particles [SGF07]. Fig.3.9 a) shows a corresponding topography image. The height difference indicates also on granulated structure existence.

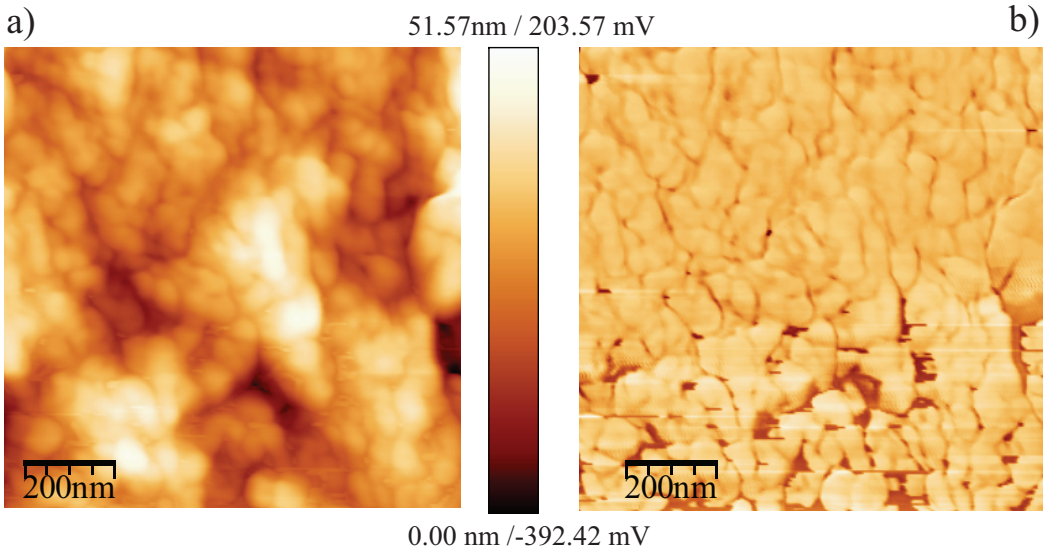

Figure 3.7: Topography a) and phase b) images of PEDOT:PSS surface reveal the granulated structure. The scan area is a) and b) 1 μm $\times$ 1 μm. High contrast regions in the phase image indicate on the change from PEDOT:PSS grains to the filling space between them.

Also the 3 dimensional topography image Fig.3.9 of the film surface clearly shows the granulated structure.

Topography images reveal the size of PEDOT:PSS shells, grain size in the range $20-50$ nm. Grains tend to stick together and form bigger grain agglomerates. Surface roughness across these grain agglomerates is in the range 10 nm. An explanation of PEDOT:PSS morphology was proposed by Nardes [Nar07] This granulated structure of a PEDOT:PSS thin film consists of PEDOT:PSS particles (shown as short black bars) surrounded by PSS shells (shown as circles) Fig.3.10. Calculations concerning the solid-state organization of PEDOT:PSS [DBL+08]

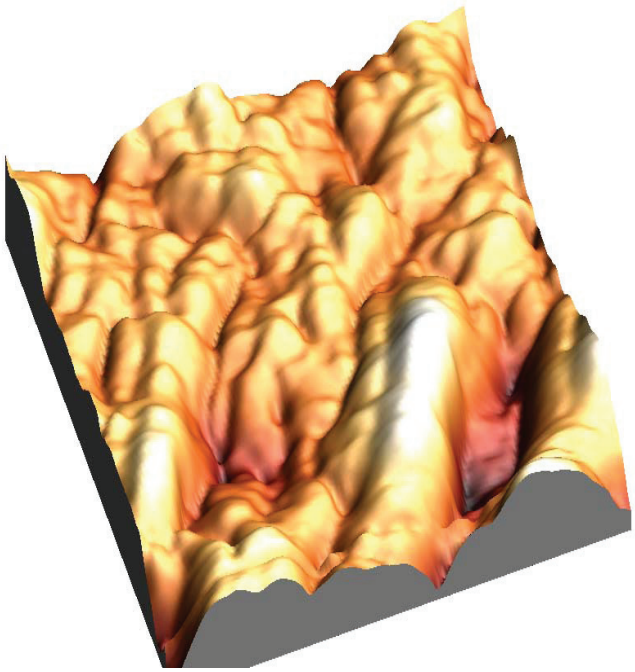

Figure 3.8: 3D image topography image of PEDOT:PSS clearly shows the granulated structure. 560 nm ×560 nm.

also confirm the existence of a one-dimensional conjugated core surrounded by an isolated core (PSS). The charge transport along the conjugated chain should be very efficient. However, the macroscopic transport should be limited by hopping between the PEDOT chains.

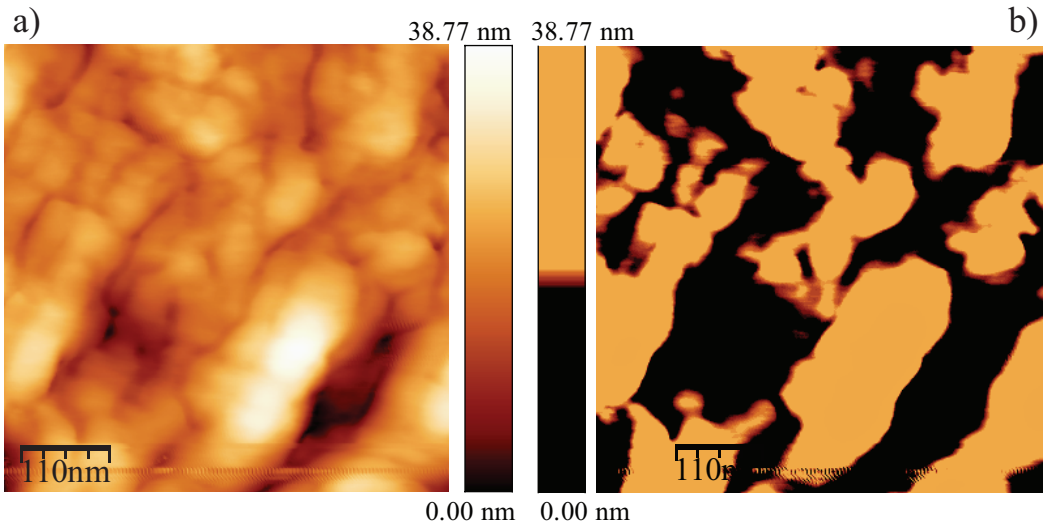

Figure 3.9: Topography image of PEDOT:PSS surface. The scan area is 560 nm× 560 nm. a) normal contrast topography image, b) high contrast topography image.

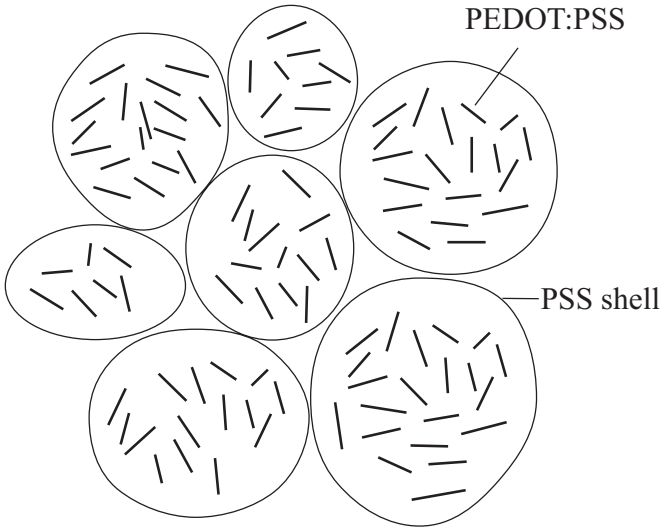

Figure 3.10: Schematically shown morphology of PEDOT:PSS [Nar07]. PEDOT:PSS-rich regions are surrounded by PSS-rich shells.

3.3 Time-domain terahertz spectroscopy (TD-TS)

Time-domain terahertz spectroscopy is a highly accurate method for dielectric function and optical conductivity determination. In transmission measurements both the amplitude of the electromagnetic wave $\vec{E}_0 = |\vec{E}_0| \exp(i\delta)$ and the phase are detected, which provides a complete information about the transmitted electric field. Terahertz spectroscopy (short THz spectroscopy) covers the far infrared part of the electromagnetic spectrum, all measurements in this work were performed in the spectral range from 10 to 30 THz, which corresponds pulse energies from ca. 40 meV to 124 meV and which in turn corresponds to excitation energies of charge carriers in the near of the Fermi Surface. Thus, THz measurements, can provide information about charge transport mechanisms in materials.

A detailed description of the measurement principle and the THz experimental setup has already been given by [Kam05], [Sch08], [Sch05] and [Nöt07]. In this thesis we will give a brief overview.

Generation and detection of THz radiation is based on nonlinear optics. Nonlinear polarization of matter is induced by strong laser pulses.

3.3.1 Nonlinear optics

From the Maxwell's equations follows a wave equation for electric field $\vec{E}(\vec{x}, t)$ propagation in matter [DG02]:

$$\nabla \times \nabla \times \vec{E} + \frac{1}{c^2}\frac{\partial^2}{\partial t^2}\vec{E} = -\frac{4\pi}{c^2}\frac{\partial^2}{\partial t^2}\vec{P}, \tag{3.1}$$

where $\vec{P}$ is the electric polarization induced by the incident electric field $\vec{E}$. In non linear media, as already shown in section 2.1, the dependence of the electric polarization $\vec{P}$ on the electric field $\vec{E}$ is given by the expansion

$$P_i = \sum_j \chi^{(1)}_{ij} E_j + \sum_{j,k} \chi^{(2)}_{ijk} E_j E_k + ... \tag{3.2}$$

The first term gives the linear dependence of the induced polarization on the incoming electric field and leads to the scalar dielectric function. The second order term $\sum_{j,k} \chi^{(2)}_{ijk} E_j E_k$, which is a nonlinear contribution, gives rise to the Pockel's effect. The third rank susceptibility tensor $\chi^{(2)}$ is given by (see [Kam05] for further reference):

$$\chi^{(2)}(\omega, \omega_1, \omega_2) = \chi^{(2)}(\omega_1, \omega_2)\delta(\omega - \omega_1 - \omega_2) \tag{3.3}$$

For positive (non degenerate) frequencies a frequency of nonlinear polarization ω can be $\omega = \omega_1 + \omega_2$, which is a sum frequency generation, or a difference $\omega = \omega_1 - \omega_2$ for difference frequency generation. $\chi^{(2)}$ vanishes in media with

inversion symmetry, but in media like gallium arsenide GaAs it leads to strong nonlinear effects as described above.

Nonlinear effects in matter enable energy conversion to electric fields with different frequencies. As a results strong sources of coherent radiation can be achieved for frequencies where no lasers are available. An example of such application is generation of THz radiation.

3.3.2 THz generation

THz radiation, in 10 to 30 THz frequency range, is generated owing to difference frequency mixing in GaSe crystal.

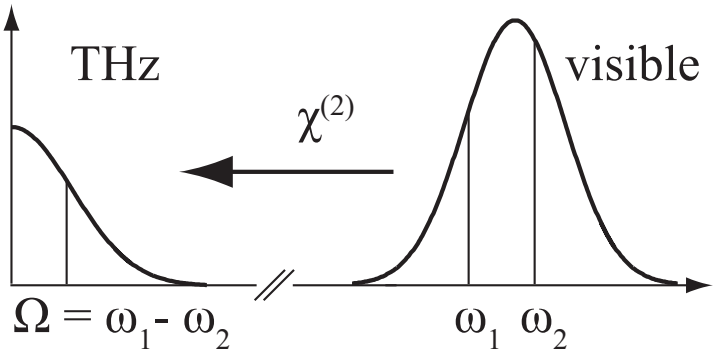

Figure 3.11: Frequency mixing in GaSe crystal due to second order nonlinear effects.

The femcosecond laser used in the experiment produces pulses centered at 780 nm with a bandwidth 80 nm. Thus it is possible to generate radiation in the frequency range $\Omega = 0...40$ THz. However, phase matching effects, which are not discussed here, limit the generated THz frequencies to the range from 10 to 30 THz.

An ideal THz wave form obtainable in the described process is shown in the Fig.3.12 a), with a spectrum shown in Fig.3.12 b).

3.3.3 THz detection

Detection of THz radiation is achieved with the use of the Pockel's effect, known also as the electro-optic effect. A THz laser pulse with an electric field $\vec{E}_{\mathrm{THz}}$ propagates collinearly with a short 10 fs visible laser pulse $\vec{E}_{\mathrm{vis}}$ inside the detection crystal ZnTe. See figure 3.13. The presence of the electric field induces nonlinear polarization. This causes birefringence in the detection crystal. As a consequence the visible sampling pulse $\vec{E}_{\mathrm{vis}}$ becomes elliptically polarized. The change in

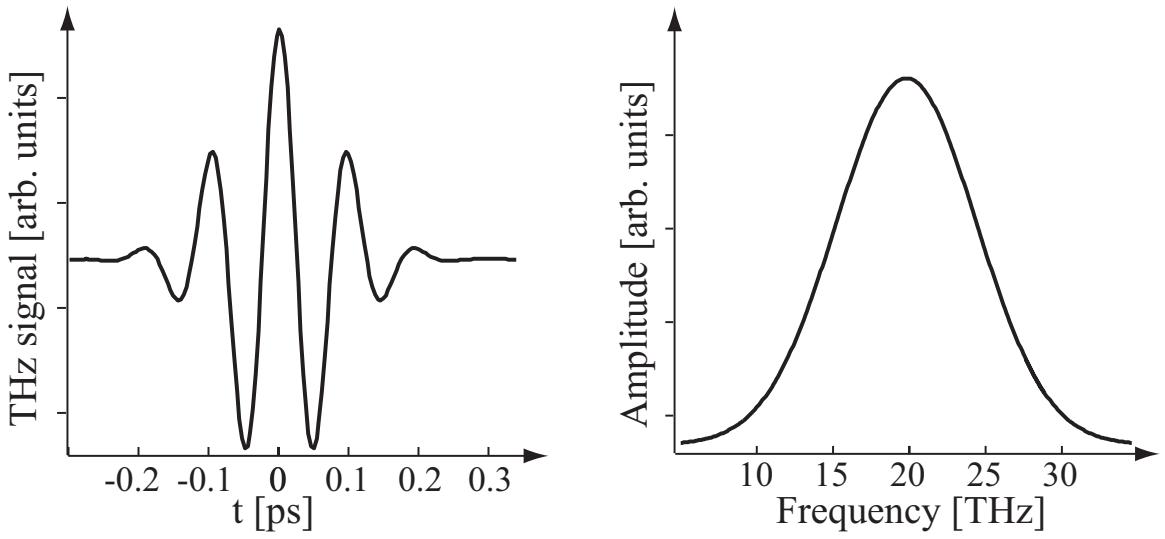

(a) (b)

Figure 3.12: a) Ideal Gaussian THz Pulse in time domain (waveform) b) Spectrum of an ideal Gaussian THz Pulse obtained by Fourier Transform of the waveform.

ellipticity of the visible pulse propagating together with the THz pulse is detected by an electro-optical setup.

The spectral range suitable for measurements is determined by the incident radiation emitted from the THz generation crystal, the silicon wafer response, as the silicon wafer acts as a filter for the NIF and transmitts the THz radiation, and the detection crystal. The spectrum of the measured reference signal E_{ref} described by Eq.(A.2) determines the frequency range over which the sample signal can be measured. Figure 3.15 shows the absolute value of both measured signals in the frequency domain. The output of the measurement setup is shown as segment. It shows the quality of detection for particular frequencies. Figure 3.14 [GP06] shows the transmission spectrum of Silicon in the THz range. At 18 THz ($\approx$ 17 μm) an absorption line of Silicon can be identified, which is also visible in the spectrum of the measured reference signal Fig.3.15.

3.3.4 THz spectrometer

THz Spectrometer allows for the steady-state THz response and the instantaneous THz response measurements of a material of interest [Kam05]. In this work we have focused on steady-state measurements.

The THz Spectrometer is schematically shown in the picture 3.16.

The THz pulse has a duration of $\approx$ 100 fs and is thus much longer that the sampling pulse. Scanning of the THz pulse is possible due to changes in the

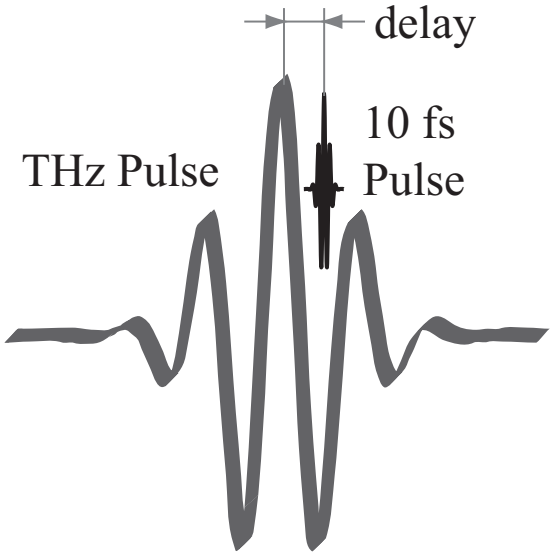

Figure 3.13: Electro-optic sampling - an ultrashort visible pulse scans step by step the THz pulse.

delay of the sampling pulse, so that for each delay the sampling pulse 'samples' a different part of the THz pulse.

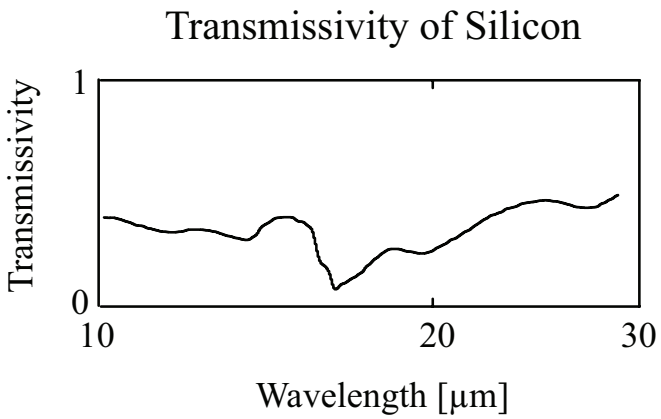

Figure 3.14: Transmitivity of Silicon [GP06].

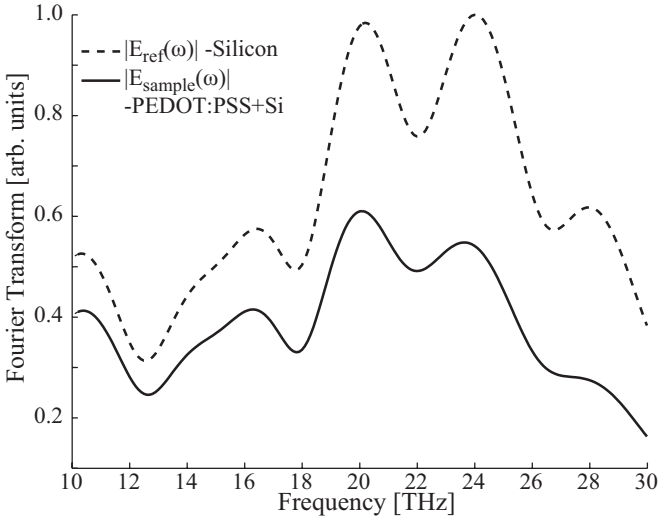

Figure 3.15: Detection spectrum. Magnitude of Fourier Transform of transmitted THz waveforms.

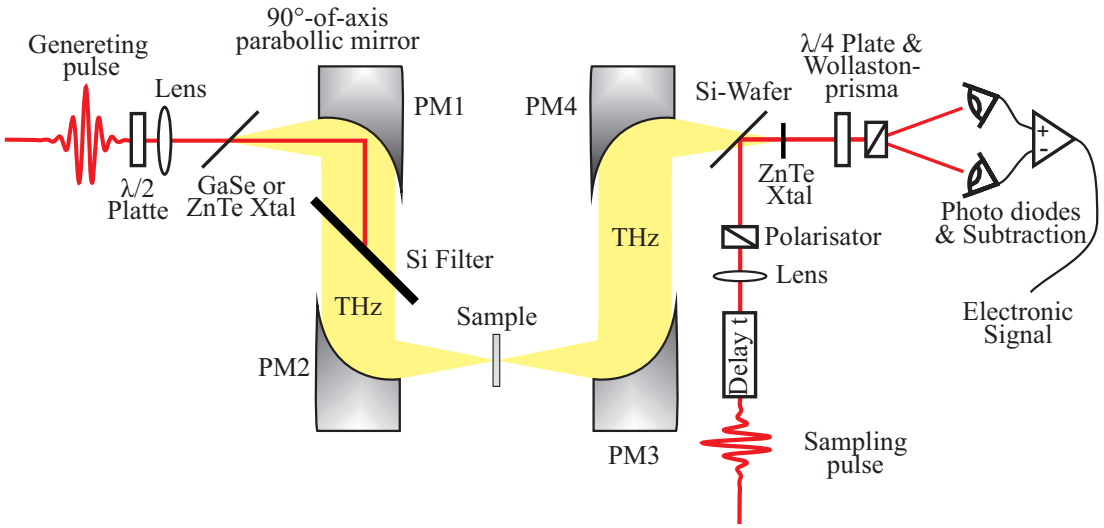

Figure 3.16: THz Spectrometer. The core of the system is a Ti:sapphire femtosecond laser operating at a 1 kHz repetition rate and producing ultra short pulses in the near infrared 780 nm of 10 fs duration [Kam05].
This ultra short, near infrared pulse when directed onto a generation crystal GaSe generates THz radiation due to the principle described in section 3.3.2. The THz beam propagates collinearly with the near infrared beam as it is collimated by the parabolic mirror PM1. A high resistivity Si wafer, the same type as used later for substrates, is placed in the beam to block the near infrared light and transmit the THz part of the beam. The transmitted THz radiation is focused on the sample by the second parabolic mirror PM2. The next two parabolic mirror PM3 and PM4 recollimate the beam and focus it onto the detection crystal ZnTe. The coming ultra short visible sampling pulse is reflected by the second Si wafer and thus propagates collinearly with the THz pulse, which is transmitted through the Si wafer, onto the detection crystal. The ellipticity change of the visible pulse induced by the THz pulse is detected by a system of a $\lambda/2$ plate and a Wollaston prism. The change of ellipticity of both electromagnetic waves $S(t)$ after passing through a Wollaston prism is measured by two photodiodes. The measured voltage is proportional the the change of ellipticity.

Chapter 4

Experimental results

A THz waveform is transmitted through a PEDOT:PSS thin film (layer 1) and a substrate (layer 2) and finally detected. This system is refered to as a two layer system. Applying a model describing the relationship between the complex refractive index and the measured THz transmission signals of PEDOT:PSS films, as described in Appendix A, enabled extracting the following material parameters:

- complex dielectric function $\hat{\epsilon}$
- complex optical conductivity $\hat{\sigma}$
- complex refractive index $\hat{n}$

All measurements were conducted in the bandwidth $10 - 30$ THz. First in sections 4.1 and 4.2 I present the complex refractive index and the complex dielectric function of PEDOT:PSS together with a thorough analysis of the measurement errors, followed by a more detailed analysis of the dielectric behavior of PEDOT:PSS. The section 4.3 contains the analysis and interpretation of the complex conductivity of PEDOT:PSS.

4.1 Complex refractive index of PEDOT:PSS

Figure (4.1) shows the obtained complex refractive index $\hat{n} = n + i\kappa$ of PEDOT:PSS for a $[2400 \pm 400]$ nm thick sample. Standard deviation plots ($\pm$ standard deviation) of both real and imaginary parts of $\hat{n}$ are presented. n and κ are response functions of the material describing propagation and dissipation of electromagnetic fields in the medium. n describes the change of the speed of light in the medium $n = \frac{c}{v}$ and κ is the extinction coefficient. Both the real refractive index n and the imaginary refractive index - the extinction coefficient κ - do not show any significant frequency dependence. Linear approximation of the refractive index $\hat{n} = n + i\kappa$ shows a dependence

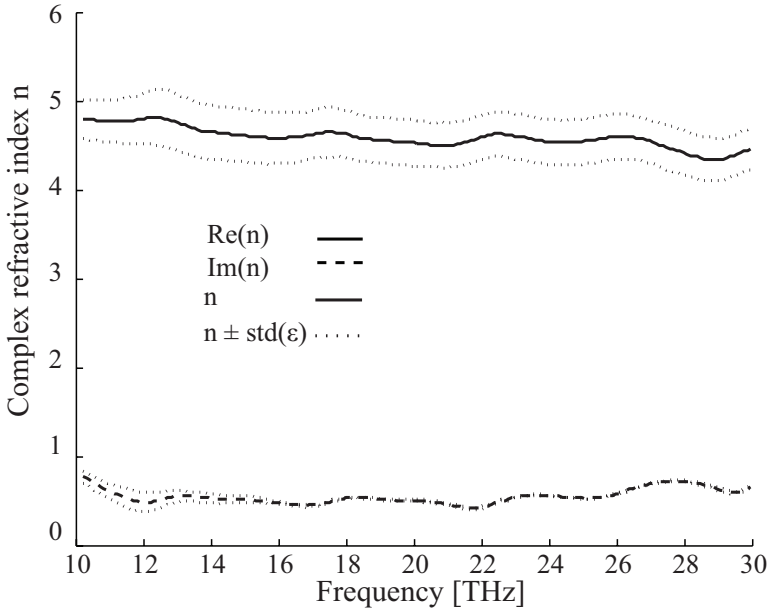

Figure 4.1: Standard deviation plot of the complex refractive index of PEDOT:PSS, sample thickness 2400 nm, measurement conducted in air at room temperature. The visible oscillations are possible artifacts of the Fourier transformation.

$$n = -\frac{[0.0106 \pm 0.0001]}{2\pi \cdot 10^{12}\ \text{Hz}} \cdot \omega + [3.19 \pm 0.35], \tag{4.1}$$

$$\kappa = \frac{[0.0034 \pm 0.0004]}{2\pi \cdot 10^{12}\ \text{Hz}} \cdot \omega + [0.30 \pm 0.05]. \tag{4.2}$$

4.2 Complex dielectric function of PEDOT:PSS

All three material parameters $\hat{\epsilon}$, $\hat{\sigma}$ and $\hat{n}$ are related to each other. This relation for non-magnetic materials is described in details in chapter 2.1 and summarized in table B.1. Both the optical conductivity and the dielectric function can be calculated from the already known refractive index.

Figure 4.2 shows standard deviation plots of the complex dielectric function of PEDOT:PSS derived for the same sample. The dielectric function, both $\text{Re}(\hat{\epsilon}) = \epsilon_1$ and $\text{Im}(\hat{\epsilon}) = \epsilon_2$, the same as the refractive index, do not show any significant frequency dependence. Nonlinearities in the standard deviation plot of the complex refractive index and the complex dielectric function are possible Fourier transformation artifacts. However, Schubert et al. in paper [SBJ+04] gave an explanation, that this effect is due to resonant vibrations. This requires

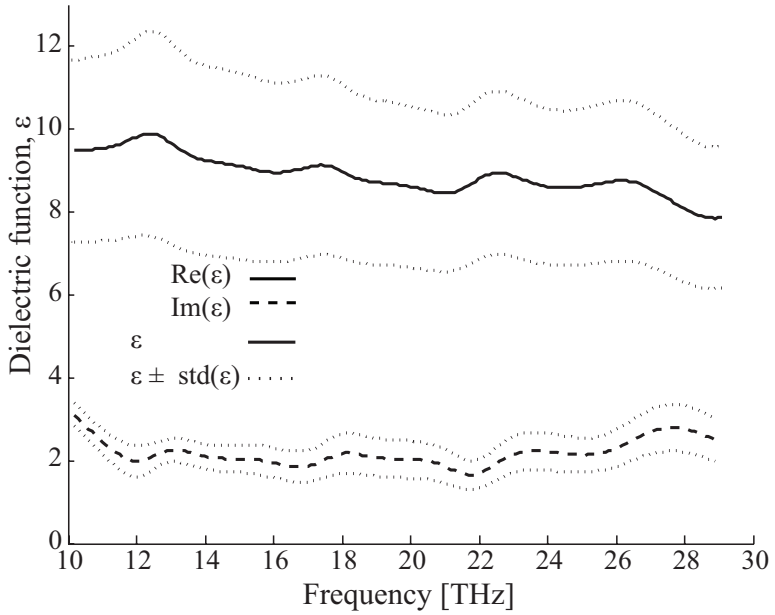

Figure 4.2: Standard deviation plot of the complex dielectric function of PEDOT:PSS for a film thickness $d_{\text{ave}} = 2400$ nm in air at room temperature. Nearly constant value of both real and imaginary part of $\hat{\epsilon}$ in the whole frequency range shows the same charge carrier response to all excitation frequencies of the applied electric field and the same indicates a lack of significant resonant vibrations.

further investigation.

Linear approximation of the dielectric function gives

$$\epsilon_1 = -\frac{[0.065 \pm 0.005]}{2\pi \cdot 10^{12}\ \text{Hz}} \cdot \omega + [10.2 \pm 2.1], \tag{4.3}$$

$$\epsilon_2 = \frac{[0.0137 \pm 0.0114]}{2\pi \cdot 10^{12}\ \text{Hz}} \cdot \omega + [1.92 \pm 0.18]. \tag{4.4}$$

The imaginary part of $\hat{\epsilon}$ is positive and small ($\approx 1.3 - 3.3$), what indicates weak absorption of THz radiation. For materials showing strong absorption in the THz range, like graphite or a superconductor BSCCO, the imaginary part of the dielectric function ϵ_2 can be as big as $50 - 350$ in the same spectral range (see appendix A.5 for details).

4.2.1 Error Analysis

In the figure 4.3 is identified the influence of the three main sources of errors in material parameter estimation from THz measurements. The sources of errors

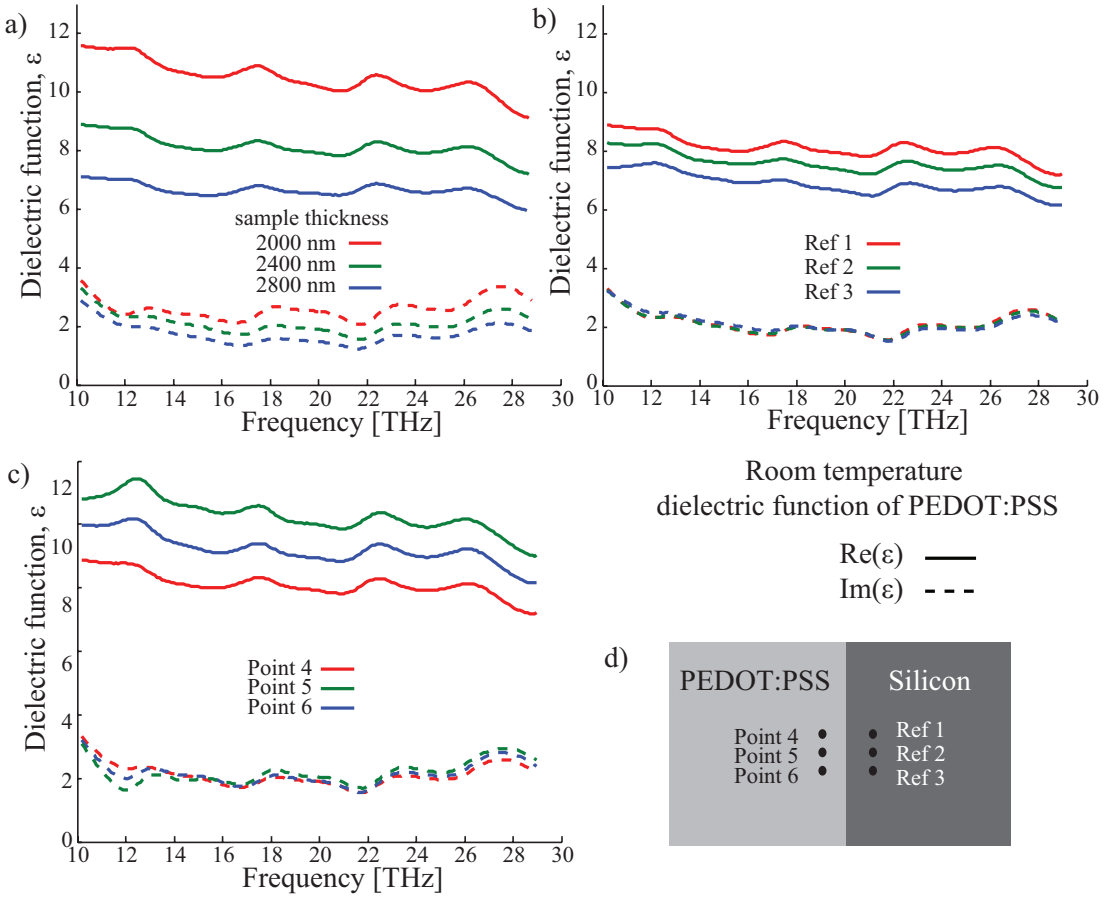

Figure 4.3: Influence of three main measurement uncertainty sources of dielectric function of PEDOT:PSS
a) Accuracy of PEDOT:PSS film thickness determination, dielectric function calculated for average thickness $d = 2400$ nm, maximum thickness $d = 2800$ nm and minimum thickness $d = 2000$ nm at one sample point and the same reference point
b) Silicon substrate homogeneity, dielectric function calculated for signals from various spots on the silicon wafer, at the same sample and average thickness
c) PEDOT:PSS film homogeneity, dielectric function calculated for signals from various spots on the sample, at the same reference point and average thickness.
d) Sample montage. PEDOT:PSS and three measurement points (left), Silicon and three reference points (right).

are due the uncertainty of thickness determination, sample inhomogeneity, which means, that THz transmission on different points on a sample varies (point dependence), and to the lack of substrate homogeneity, which results in variation of reference signal and thus dependence on the choice of points on silicon substrate for reference measurements (reference dependence). Contribution of these three sources of errors is summarized in the figure below.

Figure 4.3 a) shows a change of the calculated dielectric function for measured maximal and minimal values of PEDOT:PSS film thickness. Figure 4.3 b) shows the calculated $\hat{\epsilon}$ value for three difference points on the Silicon substrate taken for reference measurements. The next figure 4.3 c) illustrates the influence of sample quality on the calculated $\hat{\epsilon}$. THz transmission spectra were recorded for three different points on the sample surface. In the next step, the dielectric function for each point was evaluated at a fixed sample thickness and the same reference point. The major contribution the the total measurement uncertainty has the accuracy of film thickness measurement.

4.2.2 Results comparison and analysis

To reproduce our results we have measured THz transmission spectra of two PEDOT:PSS films prepared from solutions with different polymer concentrations in water and also different film thicknesses: 1700 nm and 2400 nm. Next, we determined and compared material parameters. Various points on each sample were measured, the results averaged.

As all three material parameters are related (see appendix B), therefore it is sufficient to compare only the dielectric functions of both samples. The calculated dielectric functions are shown in red and blue in Fig.4.4. Additionally we have compared our results with the dielectric function presented by Schubert [SBJ$^+$04], shown in black in Fig.4.4. He modeled the infrared dielectric function of PEDOT:PSS from ellipsometry measurements. However, the PEDOT:PSS solution was from Bayer AG, EL grade, which is different from the one used in this work. Schubert also worked with doped silicon substrates, unlike high ohmic silicon wafers used for THz measurements.

Comparison of Schubert's results [SBJ$^+$04] in the spectral range $330-1000\,\mathrm{cm}^{-1}$ with THz results in the corresponding range $10-30$ THz is shown in the figure 4.4. Both parts of the dielectric function $\mathrm{Re}(\epsilon_{\mathrm{THz}}) = \epsilon'_{\mathrm{THz}}$ and $\mathrm{Im}(\epsilon_{\mathrm{THz}}) = \epsilon''_{\mathrm{THz}}$ obtained by THz Spectroscopy measurements (red and blue lines) agree well with with results $\epsilon'_{\mathrm{Elli}}$ and $\epsilon''_{\mathrm{Elli}}$ obtained by ellipsometry (black lines) [SBJ$^+$04]. The values are in the same order of magnitude. The real dielectric function $\epsilon'_{\mathrm{Elli}}$ decreases stronger towards higher frequencies as ϵ'_{THz} does. This behavior may be due to another composition of the PEDOT:PSS solution used for measurements. Both $\epsilon'_{\mathrm{Elli}}$ and $\epsilon''_{\mathrm{Elli}}$ show resonant vibrations in the spectral range $330-1000\,\mathrm{cm}^{-1}$. These strong vibrations were not detected in THz measurements. The spectral resolution was $\Delta\omega = 0.1$ THz.

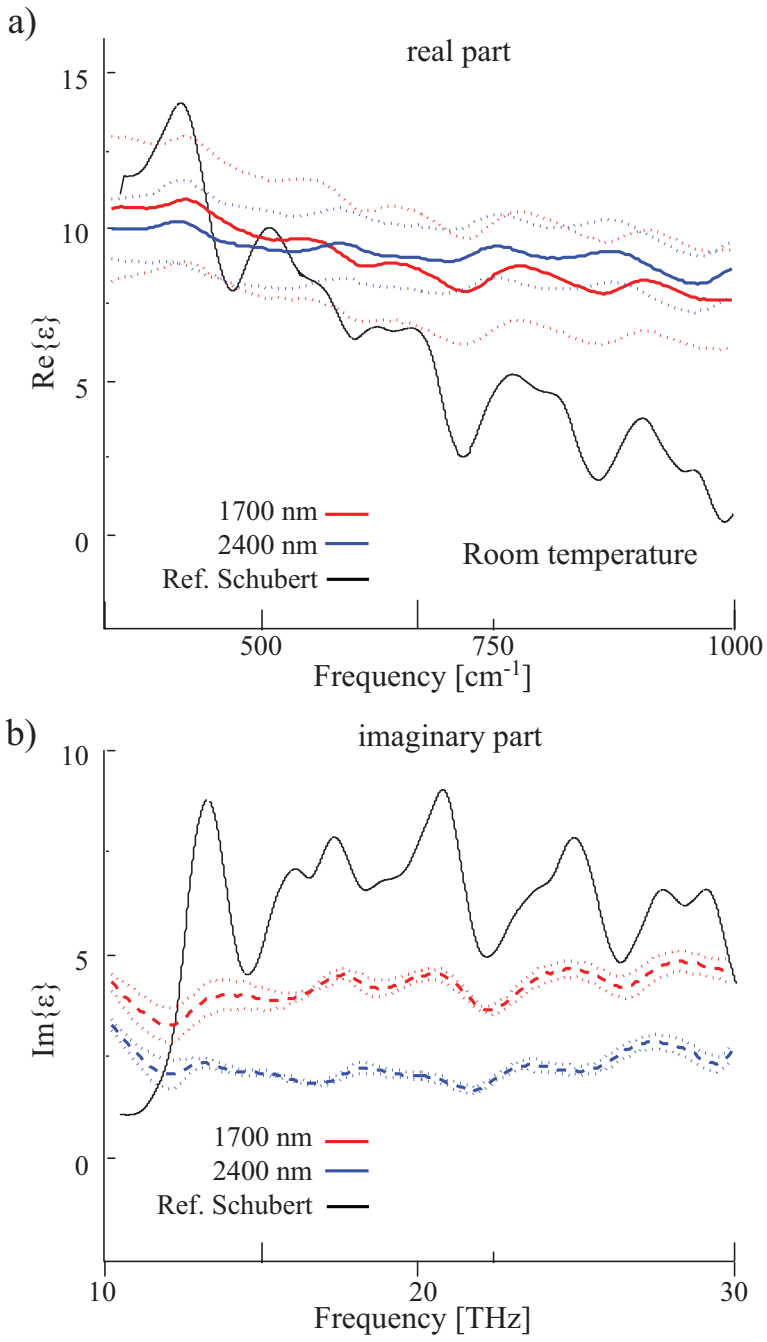

Figure 4.4: Comparison of dielectric functions obtained by ellipsometry $\hat{\epsilon}_{\mathrm{Elli}}$ [SBJ+04] (black) with THz results (red, blue) $\hat{\epsilon}_{\mathrm{THz}}$. The values of the dielectric function, both real and imaginary part, determined by both methods have in the same order of magnitude. Resonant vibrations were calculated for $\hat{\epsilon}_{\mathrm{Elli}}$. No significant resonances were observed with TD-TS.

Following Schubert [SBJ+04] the infrared dielectric function $\hat{\epsilon}$ has contributions from the high frequency electronic polarizability $\hat{\epsilon_\alpha}$, IR active bond resonance vibrations $\hat{\epsilon_{\text{vib}}}$ and free charge carrier plasma modes $\hat{\epsilon}_{\text{fc}}$:

$$\hat{\epsilon} = \hat{\epsilon}_\alpha + \hat{\epsilon}_{\text{vib}} + \hat{\epsilon}_{\text{fc}}. \tag{4.5}$$

4.3 Optical conductivity of PEDOT:PSS

In this section we will analyze the complex conductivity of PEDOT:PSS. We have conducted temperature dependent measurements of a PEDOT:PSS thin film to gain information about the type of charge transfer mechanism in the polymer. As widely known band conduction increases with decreasing temperature in semiconductors, while charge transfer caused by carrier hopping increases for growing temperature.

All results concern the sample with 2.4 μm PEDOT:PSS layer thickness. The temperature-dependent measurements were conducted in the temperature range from 4 to 320 K in 25 K steps for three different spots on the sample surface. Formulas describing optical constants in this work are derived in the gaussian unit system. However, values of conductivity are presented in the typical for σ units siemens pro centimeter of the SI system. The conversion factor from the gaussian to the SI system as given by [Jac99] is $(9 \cdot 10^{11})^{-1} \frac{S}{cm} \rightarrow \frac{1}{s}$.

4.3.1 Temperature dependence of conductivity

Surprisingly, for all temperatures the frequency dependence of $\hat{\sigma}(T)$ is the same and very weak. Also the real conductivity ϵ_1 shows no change at all and σ_2 shows only slight changes under a temperature variation. These changes lie within results' dispersion. To illustrate this, Fig.4.6 shows plots of the dielectric function for three chosen temperatures. As the order of $\hat{\sigma}(T)$ for these three measurements and chosen temperatures is different in each case and always withing the results scattering, we have not observed conductivity variation with temperature.

4.3.2 Conductivity models

To understand electric properties of PEDOT:PSS we have compared the results obtained from TD-TS with four models describing conductivity. Under the influence of a static electric field the charge transfer in PEDOT:PSS is dominated by thermally activated hopping [Nar07], [AHO05]. In the following we have analyzed the frequency dependence of AC conductivity given by two models of hopping mechanisms: Variable range hopping and quantum mechanical tunneling. Further, in sections 4.3.2 and 4.3.2, we have considered conductivity models

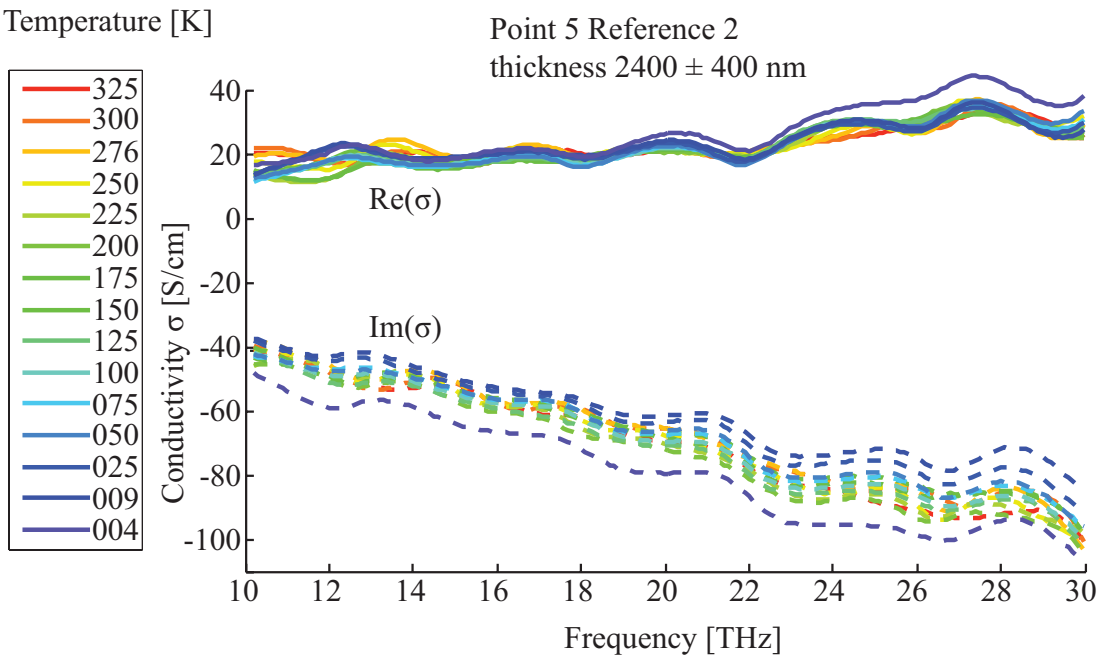

Figure 4.5: Temperature dependence of conductivity of PEDOT:PSS measured from 4 K to 320 K.

of systems with free charge carriers. As PEDOT:PSS is a conducting polymer, we expect a partially filled conduction band at room temperature.

Variable range hopping

As reported in literature [Nar07], [AHO05] the DC conductivity of PEDOT:PSS shows a strong temperature dependence and fits perfectly within the variable range hopping model (VRH), which describes conduction in disordered systems (see section 2.4). Here we will consider the real part of conductivity measured for various temperatures. The polarization conductivity, can be expressed in terms of the AC and DC conductivity [DGBZ89]

$$\sigma^{'}(\omega) = A(T)\omega^{s(T)}, \tag{4.6}$$

in the VRH model it's frequency and temperature dependence is by [DGBZ89]:

$$\sigma_{\mathrm{AC}}(\omega) = \sigma^{'}(\omega) + \sigma_{\mathrm{DC}}(0). \tag{4.7}$$

In a THz experiment we measure $\hat{\sigma}_{\mathrm{AC}}(\omega)$. As given by the PEDOT:PSS manufacturer Stack [Sta09] the DC conductivity of PEDOT:PSS Al4083 used in this work is equal to $\sigma_{\mathrm{DC}} = 1.5$ mS/cm, which is negligible in comparison with $\sigma_{\mathrm{AC}}(\omega) > 10$ S/cm. Thus, we can assume

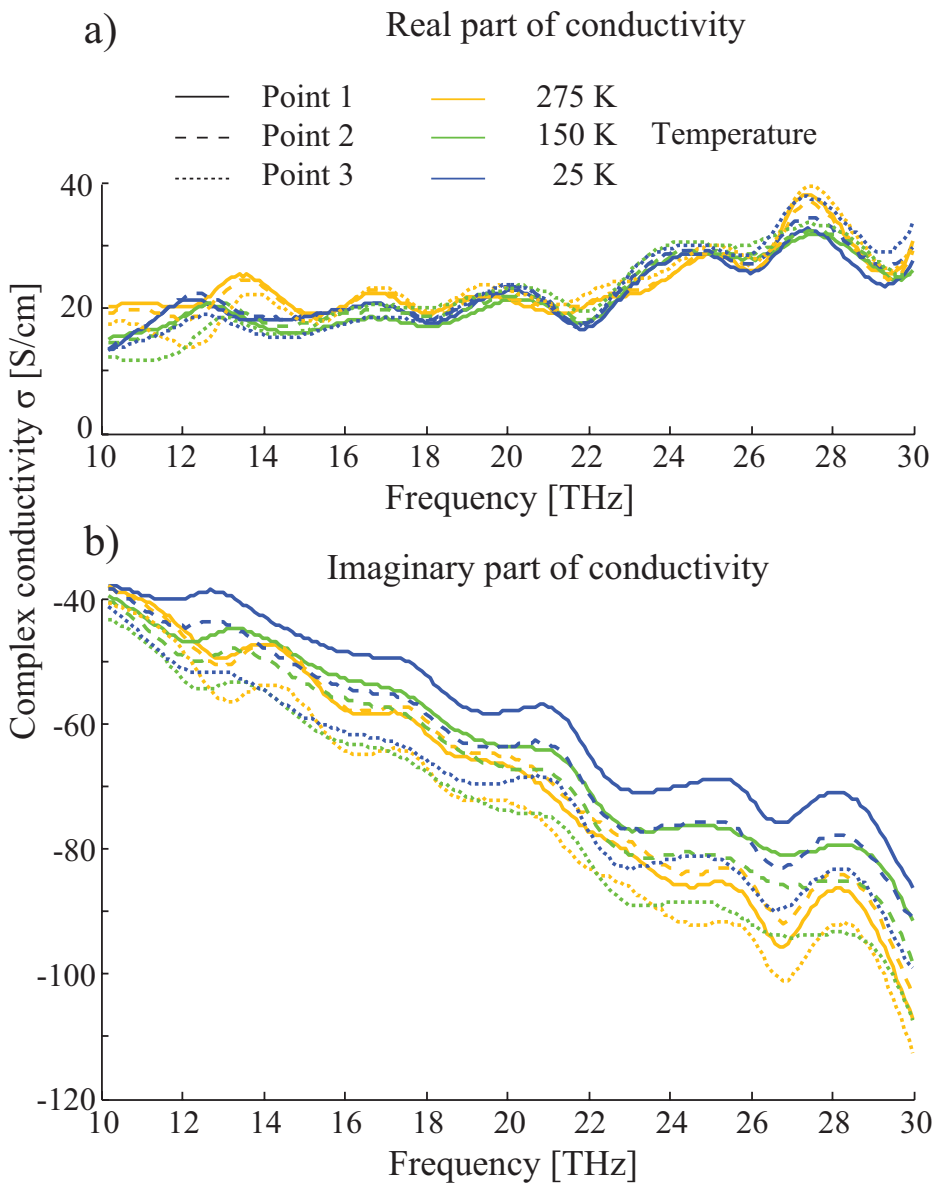

Figure 4.6: a) Real part of the conductivity b) Imaginary part of the conductivity plotted for three different temperatures for three different measurement points. Changes of the $\hat{\epsilon}(T)$ magnitude due to the temperature variation are within measurement uncertainty of the conductivity.

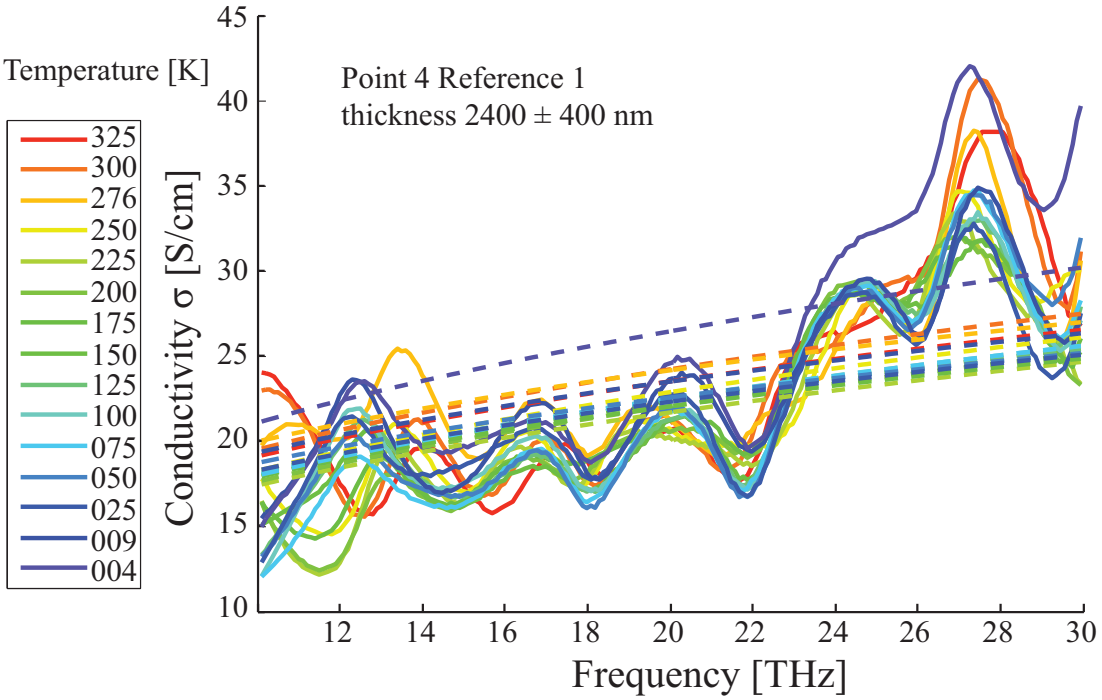

Figure 4.7: VRH fitted to the real part of the conductivity of PEDOT:PSS. The fit hat the same trend as the conductivity, however, the hopping conduction could not be observed. see text for more details.

$$\sigma^{'}(\omega) \approx \sigma_{\mathrm{AC}}(\omega). \tag{4.8}$$

To obtain the parameters $A(T)$ and $s(T)$, we have fitted $\sigma^{'}(\omega)$ given by Eq.(4.6) to the measured optical conductivity of PEDOT:PSS in the temperature range 4 K to 320 K. Figure (4.7) shows the fitted results.

The calculated fit, which in this case is roughly a straight line, follows the general trend of frequency dependence of conductivity. From the fit we obtained values of parameters $A(T)$ and s for all temperatures and all three different measured points. As the conductivity does not show any temperature dependence, the fitted parameters also don't have any. Values both parameters $A(T)$ and $s(T)$ are plotted vs. T $[K]$. See figure (4.8)

The fitted parameter $A(T)$ and $s(T)$ do not show any temperature dependence 4.8. Their average values for every measurement are given in the table below Tab.(4.1).

Quantum mechanical tunneling

Quantum mechanical tunneling (QMT) is the second model describing hopping conductivity, and as already described in section 2.4, electrons cross the potential

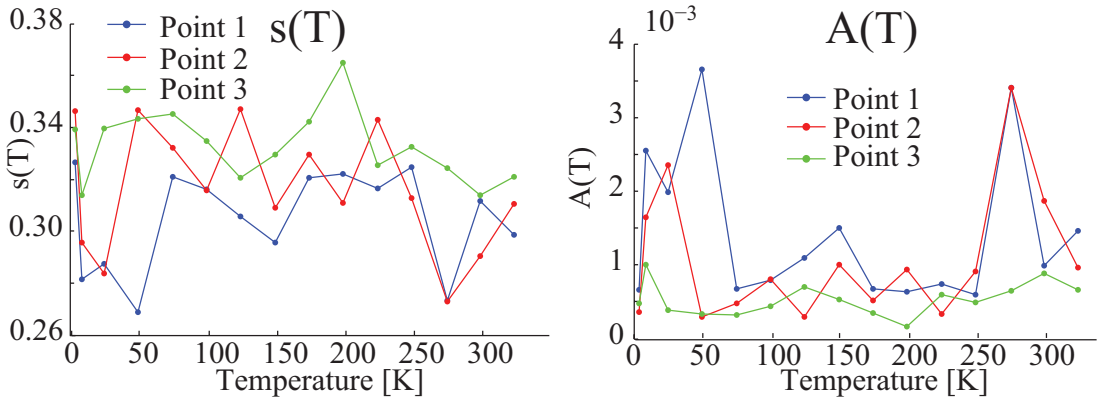

Figure 4.8: Parameters $A(T)$ and $s(T)$ fitted to the variable range hopping model for three measurement points. As expected, these is no dependence of A and s on temperature.

point	$A(T)$	$\Delta(A(T))$	$s(T)$	$\Delta(T)$
1	0.0014	0.0010	0.30	0.02
2	0.0011	0.0009	0.32	0.02
3	0.0005	0.0002	0.33	0.02

Table 4.1: Average values of fitted parameter A(T) and s(T) for three measurement points.

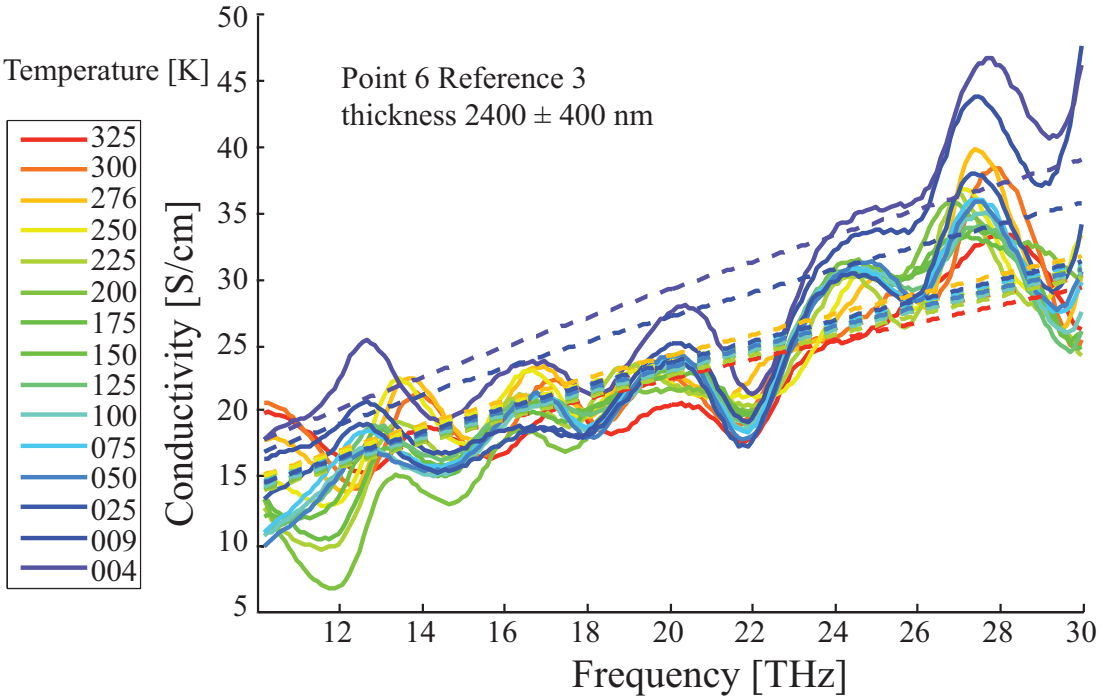

Figure 4.9: Hopping conduction model described by quantum tunneling fitted to the real conductivity of PEDOT:PSS.

barriers between localized states by quantum tunneling. Additionally to the general dependence of conductivity on frequency

$$\sigma^{'}(\omega) = A(T)\omega^{s}, \tag{4.9}$$

a more detailed one [DGBZ89] can be proved with a parameter s independent of temperature.

$$\sigma^{'}(\omega) = A(T)\omega[\ln(\frac{1}{\omega\tau_0})]^4. \tag{4.10}$$

The QMT model fitted to the experimental data is shown in the Fig.4.9.

The fitted curves for all temperatures are approximately straight lines, which overlap. The results are very similar to these obtained by fitting experimental data to the variable range hopping model. In both cases the parameter $A(T)$ and $s(T)$ does not depend on temperature, which contradicts the assumptions underlaying both models (see section 2.4).

In an optical excitation with THz radiation an electron receives an energy corresponding to the energy of the incident electromagnetic wave, which is in this case ca. 40 meV to 120 meV, which may be not sufficient to overcome existing potential barriers. A localized charge motion of a polaron within nano-scale regions

is observed. In THz experiments intra-band transitions are detected [NVMM]. Hopping conduction observed in PEDOT:PSS is a transport mechanism occurring between localized states and in this case between different molecules, thus concerns inter-band transitions. Interband transitions in PEDOT:PSS are not detected by THz spectroscopy in this case.

In DC measurements energy in supplied for the electron to overcome potential barriers between localized states and move freely between contacts. When a certain bias voltage is applied, electrons are driven between contacts. It is schematically shown in Fig.4.10. An electron excited with THz radiation is 'trapped' between existing potential barriers - PSS sites (dark gray). It oscillates locally with a frequency corresponding to the frequency of oscillations, thus $\approx 10^{12}$ Hz (black arrow), while an electron exposed to a bias voltage moves across the sample (black wave arrow) via hopping between localized sites (gray).

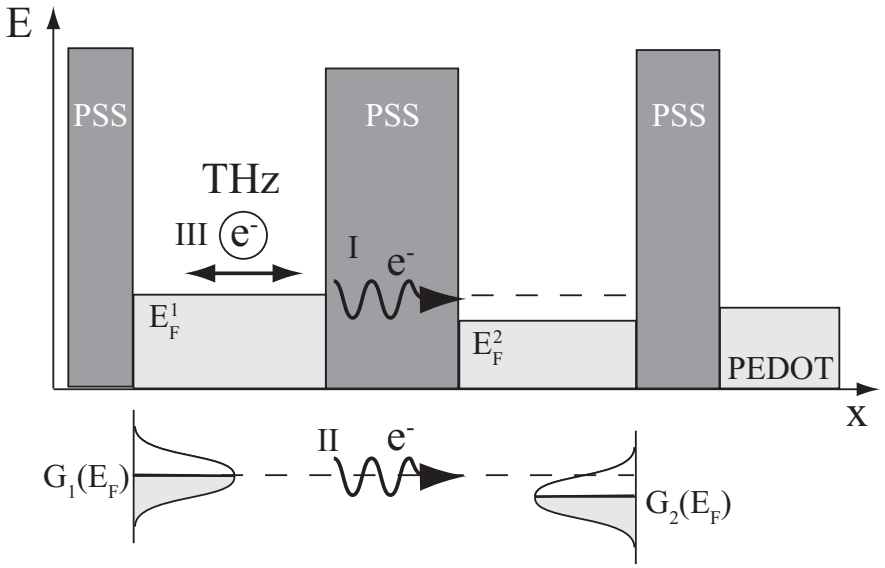

Figure 4.10: Electron trapped in a localized site. I. When a DC voltage is applied, an electron can hop (black wave arrow) between localized sites (gray) and tunnel through potential barriers - the PSS rich sites (dark gray). II. Localized sites have a density of states $G(E_{\mathrm{F}})$. When carrier energy changes, due to thermal activation, the carrier can hop to a matching neighbor state. The charge carrier can also tunnel to the neighbor state with a probability depending on the width of the potential barrier. III. Excitation with THz pulses causes fast electron oscillations (black arrow) on a nanometer range within localized sites.

Drude model

The Drude model describes the dielectric response of free charge carriers $\hat{\sigma}_{\mathrm{fc}}$ [Dru00]. Their contribution to the conductivity of PEDOT:PSS $\hat{\sigma}$ should then fit to the Drude model. Now, compare the frequency dependence of the conductivity given by Drude $\hat{\sigma}_{\mathrm{Drude}}$ (Fig.4.11) with the measured frequency dependence of the conductivity of PEDOT:PSS $\hat{\sigma}_{\mathrm{THz}}$.

The crucial parameter describing the frequency behavior of $\hat{\sigma}_{\mathrm{Drude}}$ is the scattering rate $\gamma = 1/\tau$. At the scattering rate γ the imaginary part of the conductivity $\mathrm{Im}(\sigma_{\mathrm{Drude}})$ reaches the maximum in the Drude model. The real part of the conductivity $\mathrm{Re}(\sigma_{\mathrm{Drude}})$ has the maximum at $\omega = 0$ and decreases for increasing frequency. The experimental conductivity shows exactly the opposite behavior. The real conductivity $\mathrm{Re}(\sigma_{\mathrm{THz}})$ increases with growing ω. The imaginary part of the conductivity $\mathrm{Im}(\sigma_{\mathrm{THz}})$ has a maximum at $\omega = 0$ and not at the scattering frequency γ. It implies that the conductivity of PEDOT:PSS does not show the classical Drude response. A graphical comparison between the response of PEDOT:PSS a) and predictions of the Drude model b) is shown in Fig.4.11.

Drude Smith model (DSM)

The Drude Smith model describes intraband contributions in the infrared range [Smi01]. It accounts for velocity contributions from the previous collisions, which are given by persistence velocity coefficients c_n. It is plausible to consider a single-scattering case, in which only the velocity from before the last collision has a significant contribution, so that $c_1 \neq 0$ and $c_n = 0$ for $n > 1$. This allows describing backscattering processes in localized states [Smi01].

PEDOT:PSS consists of one-dimensional chains of PSS with attached PEDOT segments Fig.4.12 a) [KR05] forming thin PEDOT:PSS gel particles surrounded by PSS [Nar07] Fig.4.12 b). Therefore localized states are present. The Drude Smith model was applied to explain the behavior of the complex conductivity of PEDOT:PSS.

The calculated complex conductivity of PEDOT:PSS fits perfectly well to the conductivity given by the DSM model with $c_1 = -1$ and $\sigma_0 = \omega_{\mathrm{p}}^2 \tau / 4\pi$ [Smi01]:

$$\hat{\sigma}_{\mathrm{DSM}}(\omega) = [\frac{\sigma_0}{1 - i\tau\omega}][1 + \frac{-1}{1 - i\tau\omega}]. \tag{4.11}$$

The fitted results are presented in the graphic 4.13 and the fit parameters are given in the table 4.2: the plasma frequency ω_p and the relaxation time τ. From predictions of the DSM: the relaxation time τ and the equation (2.63), we have calculated the frequency $\omega_{\mathrm{max}}/2\pi = (51 \pm 4)$ THz, for which the conductivity $\mathrm{Re}(\hat{\sigma})$ reaches the maximum value.

The plasma frequency ω_{p} and the relaxation time τ allow for calculating the ratio of the charge carrier concentration to the effective mass n/m^*:

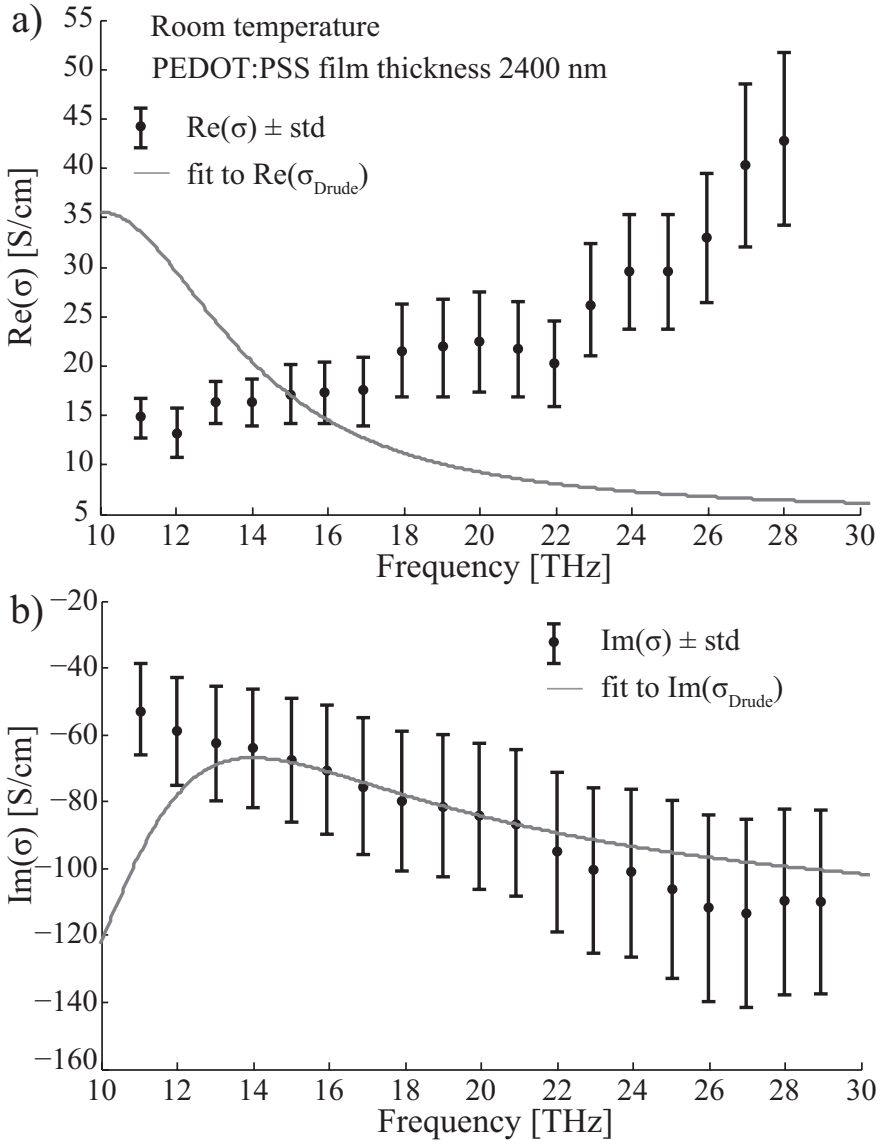

Figure 4.11: Comparison of the experimentally determined complex conductivity σ_{THz} with the predictions from the Drude model σ_{Drude}. PEDOT:PSS does not show the classical Drude response.

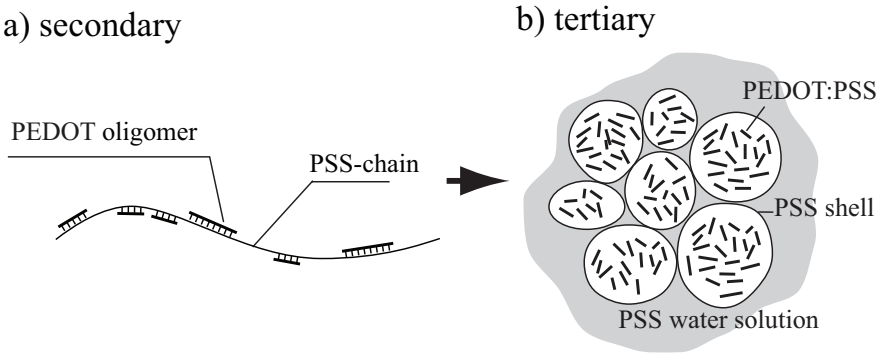

Figure 4.12: Structure of PEDOT:PSS. Formation of localized states. a) PSS-chain with PEDOT oligomers, secondary structure b) PEDOT:PSS chains forming gel particles in PSS water suspension, tertiary structure.

No.	Data	τ [fs]	ω_p [THz]
1	Re($\hat{\sigma}$)	3.1 ± 0.2	103 ± 16
2	Im($\hat{\sigma}$)	1.4 ± 0.2	363 ± 15
3	Re($\hat{\sigma}$), Im($\hat{\sigma}$)	2.3 ± 0.90	233 ± 130

Table 4.2: Parameters fitted to the Drude Smith model: τ and ω_p. Three data set were fitted : separately the real Re($\hat{\sigma}$) and complex Im($\hat{\sigma}$) conductivity, together Re($\hat{\sigma}$) and Im($\hat{\sigma}$).

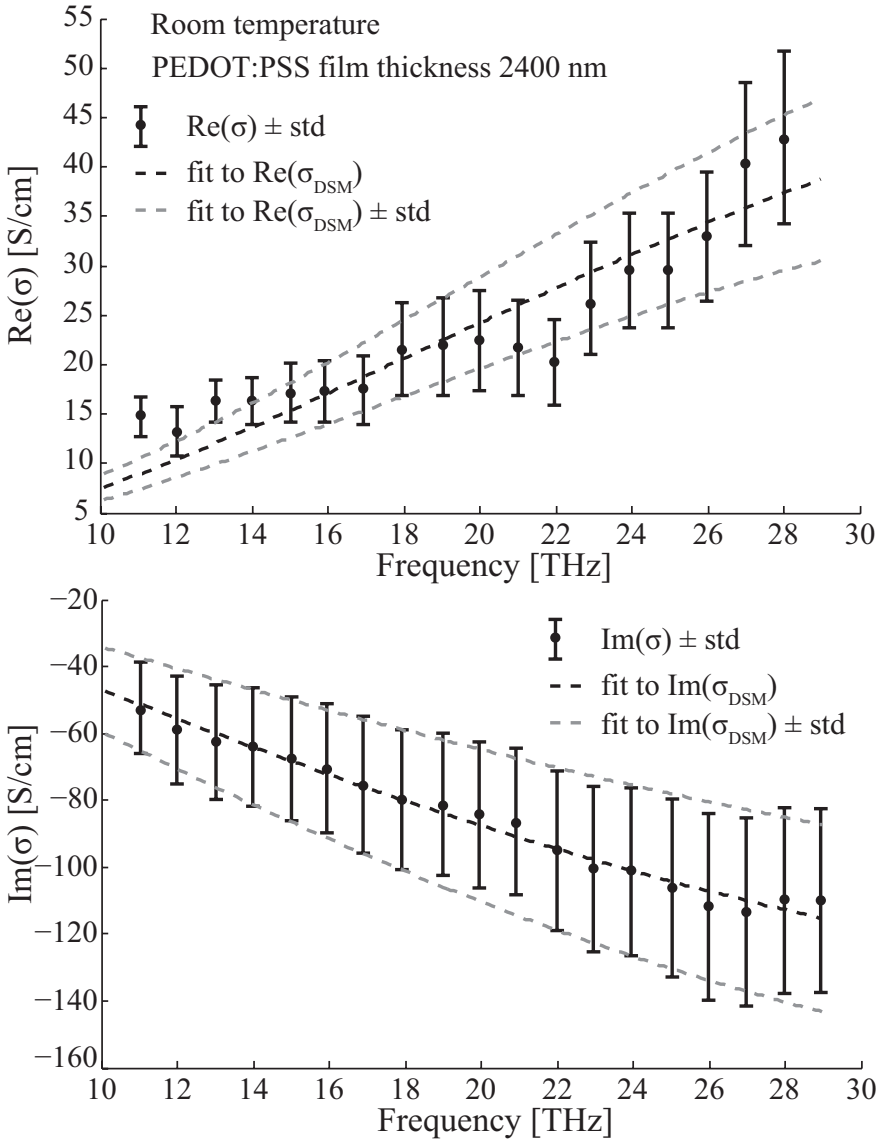

Figure 4.13: Average complex conductivity of PEDOT:PSS fitted to Drude Smith model with persistence velocity coefficient $c_1 = -1$.

$$n/m^* = (365 \pm 75) \cdot 10^{46}\ \mathrm{cm}^{-3}\mathrm{kg}^{-1}, \tag{4.12}$$

The effective mass of an electron in a PEDOT:PSS isolated chain is $m^*/m_0 = 0.099$ according to Kim [KJ08], where $m_0 = 9.1093897 \cdot 10^{-31}$ kg is the electron mass at rest. The equation (4.12) and the effective mass m^* allow for estimating the electron concentration in PEDOT:PSS isolated chains:

$$n = (3.3 \pm 0.7) \cdot 10^{17}\ \mathrm{cm}^{-3}. \tag{4.13}$$

For metals, like copper, gold or silver, the electron concentration is in the order of $n \approx 5 \cdot 10^{22}\ \mathrm{cm}^{-3}$ [AM76], which is approximately 100,000 times higher, which results, of course, in a significantly higher conduction. The Drude relaxation times in metals are in the order of femto second, e.g. for iron $\tau_{\mathrm{Fe}} = 2.4$ fs at 273 K [AM76].

The DC conductivity σ_0 estimated from the Drude Smith model is equal to

$$\sigma_0 = (2.9 \pm 0.6)\ \mathrm{S/cm}. \tag{4.14}$$

As stated by the manufacturer C. H. Starck [Sta09] the solution of PEDOT:PSS Al4083 has a DC conductivity $\approx 0.001\ \mathrm{Scm}^{-1}$. It has been reported [Nar07], [KR05], that the preparation process has a crucial impact on the DC conductivity of PEDOT:PSS. As for sample preparation (see section 3.1) the PEDOT:PSS solution received a long heat treatment resulting in a density change of the solution, it is possible that the parameters of the solution changed significantly. The manufacturer [Sta09] has claimed to have produced a PEDOT:PSS solution with a conductivity as high as ≈ 500 S/cm. Accounting for the wide spectrum of PEDOT:PSS conductivity values ranging from $\approx 10^{-5}$ to 500 S/cm, the value $\sigma_0 = (2.9 \pm 0.6)\ \mathrm{Scm}^{-1}$ obtained from the model predictions is within the range of the reported DC conductivity values.

DSM predicts that conductivity reaches the maximum value at the frequency $\omega_{\max} = 50.8 \pm 2.6$ THz. It follows from the equation (2.63), the fitted relaxation time τ and the persistence velocity coefficient $c_1 = -1$.

Measurements of PEDOT:PSS conductivity in a higher spectral range 40 to 60 THz will reveal if there is a conductivity maximum in the indicated range and consecutively if the Drude Smith model provides an accurate description of charge behavior in PEDOT:PSS.

The value $c_1 = -1$ of the persistence velocity coefficient indicates strongly on the charge carrier localization in PEDOT:PSS. Charge carriers undergo backscattering.

We already know that PEDOT:PSS is a disordered material. PEDOT:PSS chains, shown schematically in Fig.4.12 a), form grains in the order of ≈ 20 - 30 nm, which are surrounded by the water solution of PSS. See section 3.2 for details. The graphic 4.12b) illustrates PEDOT:PSS chains forming grains or gel

particles in PSS suspension. Between such grains charge transport is dominated by interchain variable range hopping [Nar07].

Sample illumination with a laser pulse with an electric field oscillating with the frequency $\approx 10^{12}$ Hz, causes local excitation of electrons within polymer chains. Due to the high frequency of the electric field, the electrons oscillate extremely fast, thus they are being moved by the $\vec{E}$ field on a namometer scale only. Thus, TD-TS probes local conductivity. Charge transfer between polymer chains requires high activation energies, which are not supplied during a short range THz excitation. Excitations with THz pulses are withing single polymer chains. However, the measured THz signal is a sum of contributions of carrier excitations from a larger region, as the size of the laser spot in focus is ca. 100 μm.

Charge transport within a single polymer chain can be considered as one dimensional, thus defects within the polymer chain cause electron backscattering. Alternatively, to move further along the polymer chain an electron can hop to the nearest state. See Fig.4.14 c). Hopping conduction within a polymer chain requires again an activation energy. The model of electrons backscattering on defects within polymer chains agrees perfectly well with predictions of the Drude Smith model.

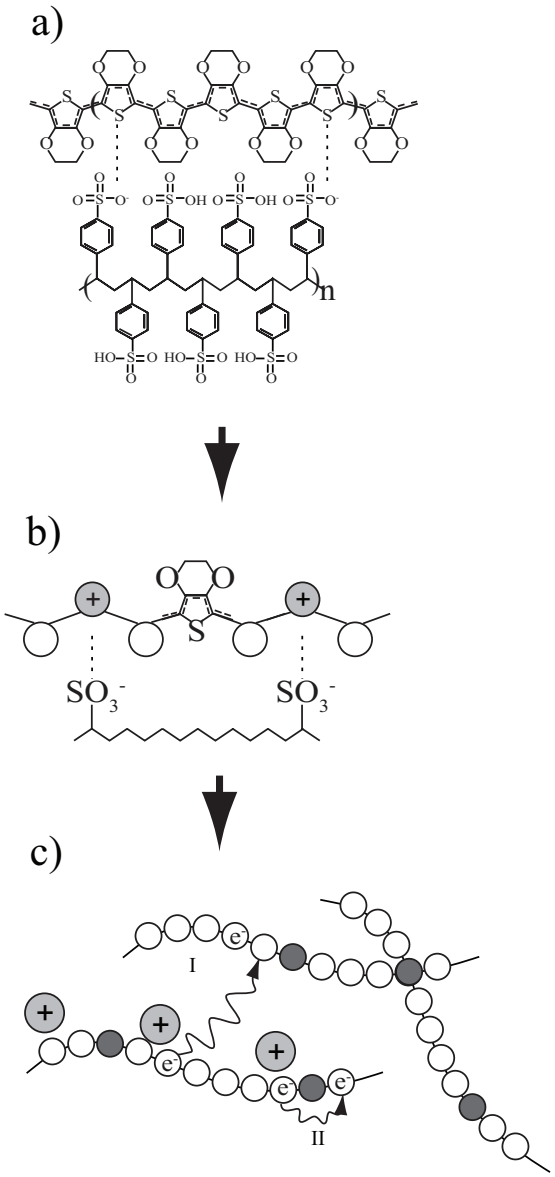

Figure 4.14: a) Primary structure of PEDOT:PSS, b) PEDOT doping with negatively charged SO_3^- groups from the PSS chain. Formation of positively charged ions in the PEDOT chain (gray) c) I - hopping between chains, II - hopping within a PEDOT:PSS single chain, dark gray - defects in the polymer chain, gray - positively charged ions in the PEDOT chain resulting in strong electron - phonon interaction: polaron formation.

Chapter 5

Summary and conclusions

Due to their unique features, like flexibility and easy processing, organic polymers are a highly interesting alternative to classical semiconductors. The polymer PEDOT:PSS is presently dominating the market of conducting polymers. Although until today it has been vastly applied in various areas of organic electronics and as coatings even in traditional inorganic electronics. But still the charge transfer mechanism has not been fully understood yet.

TD-TS is sensitive to electrons with excitation energies in the meV range, thus, as it has been shown [vLFK+08], it provides a detailed information on the nature of the charge transport also in polymers. In this work I have presented the first successful results of measurements on PEDOT:PSS with time-domain terahertz spectroscopy. For PEDOT:PSS we have demonstrated that it is possible to determine the complex dielectric function $\hat{\epsilon}$, the complex refractive index $\hat{n}$ and the complex conductivity $\hat{\sigma}$ in the far infrared range.

PEDOT:PSS thin films on silicon substrates were successfully fabricated by using spin-coating directly from a commercial water polymer solution, without further treatment. The optimal thin film thickness for THz measurements was determined and found to be within the range $1.7 - 2.4\ \mu$m. The sample preparation process was then optimized by reprocessing the water suspension to fabricate samples with an exactly matching thickness and homogeneity for THz measurements, so that the THz radiation is absorbed by approximately 30%. The sample thickness is a crucial parameter for success, because thin polymer films of thickness below 140 nm, do not absorb enough radiation to perform measurements. The measurement uncertainty for these films is so high, that it was found, that based on the extracted dielectric function, it is not possible to draw any conclusions about transport mechanisms. Consequently, an important factor is the sample homogeneity, because film thickness variation holds the dominating contribution to the total measurement error.

To derive the dielectric function and thus $\hat{n}$ and $\hat{\sigma}$ from the THz measurements, the model for the dielectric function calculation had to be revised. The previously applied thin film formula describing the dielectric function [Kam05] is only a second order approximation. As the investigated samples of PEDOT:PSS are nearly forty times thicker than samples previously measured with the same experimental setup [Kam05], [Sch08], the assumptions underlying the validity of the applied approximation have not been met. To evaluate the measured data and to extract the interesting material properties a completely different way for solving the general formula for the dielectric function numerically has been implemented and applied.

Both the complex refractive index and the dielectric function, as they are related by $\hat{\epsilon} = \hat{n}^2$, do not show any significant frequency dependence in the investigated bandwidth. The values of both parts of the dielectric function are approximately $\mathrm{Re}(\hat{\epsilon}) = [9 \pm 3.0]$ and $\mathrm{Im}(\hat{\epsilon}) = [2.3 \pm 1.0]$. The obtained results are in good agreement with results found in literature [SBJ$^+$04]. Both dielectric functions are in the same order of magnitudes, further differences may be due to different types of PEDOT:PSS solutions and substrates used in both measurements.

Additionally, we have examined the conductivity of PEDOT:PSS in the far infrared region with time-domain terahertz spectroscopy and compared it with conductivity models describing free charge carriers (Drude model, Drude Smith model) and hopping conduction (variable range hopping, quantum mechanical tunneling). It has been reported [AHO05], [Nar07] that the electric transport on macroscopic distances is dominated by charge carrier hopping. However, this hopping mechanism has not been observed with TD-TS. The THz signal is an integrated material response over a spot size of ca. 100 μm in diameter. Charge carriers oscillate due to excitations with an incident electric field with a THz frequency. Thus, these oscillations are on nanometer range. THz radiation induces local charge carrier oscillations and does not provide sufficient energy to overcome the existing potential barriers. The conductivity and dielectric behavior of PEDOT:PSS does not follow the simple Drude model describing the response of free charge carriers. Thus PEDOT:PSS, an organic semiconductor, is not comparable with classical metals as it has been desired for applications.

To explain the measured optical conductivity we have compared our results with the predictions of the Drude Smith model. It is a generalization of the classical Drude formula accounting for the influence of localized states on the conductivity. The Drude Smith model fits the experimental data very well. From the predictions of the Drude Smith model the plasma frequency was estimated

$\omega_p = 103 \pm 16$ THz at room temperature and the scattering time of PEDOT:PSS $\tau = 3.1 \pm 0.2$ fs, which is comparable with the scattering time of iron $\tau_{\mathrm{Fe}} = 2.4$ fs at 273 K [AM76]. The charge carrier concentration of PEDOT:PSS was calculated to be $n = (3.3 \pm 0.7) \cdot 10^{17}$ cm^{-3}, which is significantly lower than in metals, where $n \approx 5 \cdot 10^{22}$ cm^{-3} [AM76].

We have confirmed the existence of a granulated structure in PEDOT:PSS thin films, which has previously been reported by [SGF07], [Nar07] and [TKT$^+$04], with AFM. Topography images of PEDOT:PSS films, obtained with atomic force microscopy, revealed the polymer's microstructure and provided information about the film thickness, which was measured at the PEDOT:PSS - silicon edge. Formation of gel particles, with PEDOT:PSS chains surrounded by PSS shells and PSS water suspension, indicates on the presence of localized grain-sites. In order to move on macroscopic distances electrons have to overcome potential barriers existing between $20 - 30$ nm long grains. Charge carriers are trapped within these localized grain-sites consisting of highly conductive PEDOT:PSS chains surrounded by isolating PSS shells. We suppose, that localized sites exist also inside these highly conductive grains.

The Drude Smith model fits the experimentally determined conductivity perfectly well. The Drude Smith model with the fitted persistence velocity $c_n = -1$ predicts, that charge carriers are scattered at an angle of $\theta = 180°$, as $c_n = \langle \cos\theta \rangle$. This means, that in average, charge carriers are backscattered. A possible explanation is, that as the carrier motion is much higher along the polymer chain [Bru08], [Bar05], it can be considered as one-dimensional. Impurities and structural defects inside PEDOT:PSS chains would act like scattering centers, which, accounting for the one dimensionality of the system, leaves only one possibility for scattering: backscattering. In order to move forward charge carriers could hop through the scattering centers by thermally activated hopping or by tunneling through the potential barriers of the scattering centers. However, this hypothesis has to be further investigated.

Surprisingly, we have not observed any temperature dependence of the conductivity of PEDOT:PSS within the range from 4 K to 300 K. Both charge transfer mechanisms present in conducting polymers: band transport and hopping transport show significant temperature dependence. For the first one, the charge carrier mobility increases with decreasing temperature, owing to fewer scattering events. For hopping conductivity the mobility increases with increasing temperature, due to thermal activation of the process. The lack of the temperature dependence of PEDOT:PSS might be due to compensation of both mechanisms. This, however, has to be investigated more carefully. To do so one could measure

the conductivity of other PEDOT:PSS species, with different ratio of PEDOT to PSS, resulting in different PEDOT:PSS film conductivity. Measurements of pure PSS, which is an insulator, will help determine, whether the locally measured conductivity in a THz experiment is the conductivity of a PEDOT:PSS conducting region, or of a boundary between PEDOT:PSS and PSS insulating domain, or maybe an averaged conduction of a region of mixed properties. In these cases, for various chemical compositions of investigated materials, one charge transfer mechanism should dominate over the other revealing a temperature dependence.

THz spectroscopy provided important information on charge transfer mechanism in the conducting polymer PEDOT:PSS on the nanoscale. The Drude Smith model predicts an existence of a conductivity maximum $\mathrm{Re}(\hat{\sigma}_{max})$ at $\omega_{\max}/2\pi = (51 \pm 4)$ THz. To confirm that the charge carriers in PEDOT:PSS are in average backscattered, when moving along polymer chains, the PEDOT:PSS conductivity has to be investigated in a broader range of the THz spectrum.

Appendix A

Derivation of the Formula for Dielectric Function for a Two Layer System

A.1 Linear system

In this chapter we will derive a model for parameter extraction from the signal measured in a THz experiment. The model for dielectric function calculation for a three layer system has previously presented by [Kam05]. Slight corrections and model derivation for a two layer system, like the PEDOT:PSS / Si system are presented in this work. As described in chapter (3.3.4) the experimental setup consists, briefly, of a THz generator, an optical path, a two layer sample/reference system and a detector. We consider light propagation only in the z direction, so we can derive a model in one dimension. Besides we treat the incoming electromagnetic waves as plane waves.

An initial signal $E_{\text{incident}}(r,t)$, a THz wave form (Fig.3.12), is being projected onto a sample, transmitted through the sample, transmitted through the reference and finally detected Fig.A.1 as $E_{\text{sample}}(r,t)$. A detailed analysis of the beam path will be given below. In chapter 2.1 we assumed a linear response of the investigated material to the stimulus - incident electromagnetic field ($\vec{D} = \epsilon\vec{E}$), therefore the system under consideration can be described in terms of the linear time invariant system theory [PWK07]. Therefore the detected signal $E_{\text{sample}}(r,t)$ in the time domain is a convolution of the initial signal $E_{\text{incident}}(r,t)$ with the sample transfer function $h_{\text{sample}}(r,t)$ and a transfer function of the reference material together with the detector response function $h_{\text{ref}}(r,t)$ (Silicon wafer used as a substrate for PEDOT:PSS films).

In analogy the reference signal E_{ref} is a convolution of the incident beam passing through an air layer instead of a sample with a reference layer response function and a term for wave propagation in the air on a distance d_1. Fig.(A.2).

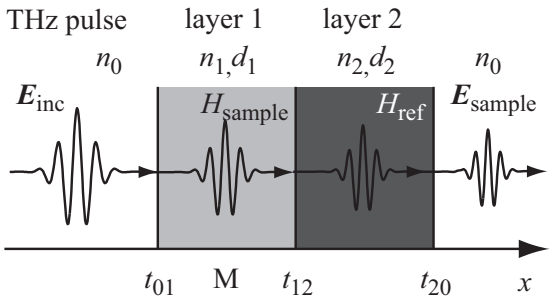

Figure A.1: THz radiation $E_{\text{incident}}(r,t)$ transmission through the two layer system - sample and reference. The surrounding medium is air.

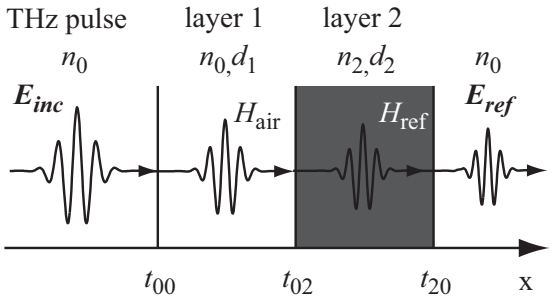

Figure A.2: THz radiation $E_{\text{incident}}(r,t)$ transmission through the two layer system - reference part. The surrounding medium is air.

Applying the Parseval's theorem in the frequency domain gives

$$E_{\text{sample}}(k,\omega) = H_{\text{sample}}(k,\omega) \cdot H_{\text{ref}}(k,\omega) \cdot E_{\text{incident}}(k,\omega), \tag{A.1}$$

$$E_{\text{ref}}(k,\omega) = H_{\text{air}}(k,\omega) \cdot H_{\text{ref}}(k,\omega) \cdot E_{\text{incident}}(k,\omega), \tag{A.2}$$

where H_i are the corresponding transfer functions in the ω space. Therefore the ratio of measured signals in the frequency domain multiplied by the factor accounting for electromagnetic propagation in air H_{air} gives the searched transfer function H_{exp} of the sample material.

$$H_{\text{exp}}(k,\omega) = \frac{E_{\text{sample}}(k,\omega)}{E_{\text{ref}}(k,\omega)} = \frac{H_{\text{sample}}(k,\omega) \cdot H_{\text{ref}}(k,\omega) \cdot E_{\text{incident}}(k,\omega)}{\mathrm{H}_{\text{air}}(k,\omega) \cdot H_{\text{ref}}(k,\omega) \cdot E_{\text{incident}}(k,\omega)}. \tag{A.3}$$

Provided that the sample thickness is known the transfer function of an air layer H_{air} can be calculated.

$$H_{\text{exp}}(k,\omega) \cdot H_{\text{air}}(k,\omega) = H_{\text{sample}}(k,\omega). \tag{A.4}$$

The left side of the equation (A.4) is the measured transfer function H_{exp} of the sample material, while the right side can be modeled theoretically. In chapter (A.2) we will derive a model for $H_{\text{theor}} = H_{\text{sample}}$.

A.2 Model derivation

Consider an electromagnetic wave E_{incident} propagating in one dimension through a two layer system as shown in the picture Fig. A.1. Each medium has a thickness and a refractive index corresponding to n_i, d_i. First, E_{incident} is partially reflected and partially transmitted on the interface between air and medium 1. We are only interested in the transmitted part of E_{incident}, as the reflected part of the incoming radiation does not reach the detector. The behavior of E_{incident} when passing through the interface between media of two different refractive indexes is describes by the Fresnel's equations [DBM01]. Here we assume that the sample plane is orthogonal to the direction of light propagation z. It follows that the angle of incidence is 90° and the Fresnell's coefficients for transmission t_{ij} and reflexion r_{ij} take a form

$$t_{ij} = \frac{2n_i}{n_i + n_j}, \tag{A.5}$$

$$r_{ij} = \frac{n_i - n_j}{n_i + n_j}. \tag{A.6}$$

Light E_1 transmitted through the interface $0-1$ is then given by

$$E_1 = t_{01} E_{\text{incident}}. \tag{A.7}$$

On the sample boundary - interface $1-2$ between media 1 (PEDOT:PSS sample) and media 2 (Silicon substrate) - the electromagnetic wave is again partially transmitted and partially reflected. Reflected light undergoes multiple reflections inside the sample [Kam05].

Multiple reflections inside layer 2 (substrate) are in the order of pico seconds. As the temporal window of the THz waveform detection is up to 0.8 ps, the multiple reflections are outside the temporal window of the THz detection. Therefore multiple reflections inside Silicon wafer can be neglected. It follows that M, a factor describing multiple reflection, is $M = 1$ for this layer. However, multiple reflections inside a thin-film sample (layer 1) have to be accounted for Fig.A.3.

First, a part of the wave E_1 is transmitted through the layer 1 (no reflections inside the sample $E_1 = E_{R0}$), a part after having propagated at a distance d_1, is reflected at the second boundary $1-2$ $E_1 r_{12} \exp(2ik_1 d_1)$. It then propagates back and is partially transmitted on the interface $0-1$ E_{out}, this part of radiation does not reach the detector, thus is not interesting. However, the reflected part propagates back and after one internal reflection (at both boundaries) is equal

to $E_{R1} = E_1 r_{01} r_{12} \exp(2ik_1 d_1)$. It gets again partially transmitted and partially reflected [DBM01].

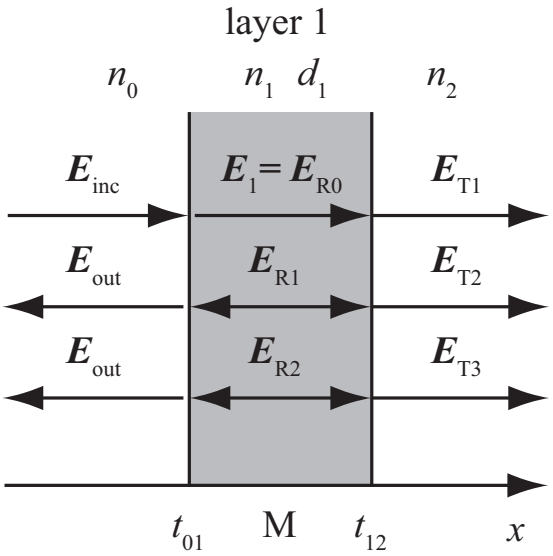

Figure A.3: Multiple reflections inside a thin film.

The detected signal is the sum of all waves transmitted through the system. The in this work presented transmission spectra were recorded for 0.8 ps, which accounts for approximately 30 multiple reflections inside the PEDOT:PSS thin film.

$$E_{sample} = E_{T1} + E_{T2} + E_{T3} + ... \tag{A.8}$$

The multiple reflection factor M describing infinitely many reflections inside the sample is thus equal to

$$M = 1 + r_{10} r_{12} \exp(2ik_1 d_1) + (r_{10} r_{12} \exp(2ik_1 d_1))^2 + ... \tag{A.9}$$

as it is a sum of the geometric series it is equal to

$$M = \frac{1}{1 - r_{10} r_{12} \exp(2ik_1 d_1)}. \tag{A.10}$$

Summarizing, the electromagnetic wave transmitted through this system can be written as

$$E_{\text{sample}} = t_{01} e^{ik_1 d_1} M t_{12} e^{ik_2 d_2} t_{20} E_{\text{incident.}} \tag{A.11}$$

An incident electromagnetic wave transmitted through a reference system Fig.(A.2), which consists of air (layer 1) and a substrate (layer 2), can be represented as

$$E_{reference} = t_{00}e^{ik_0d_1}t_{02}e^{ik_2d_2}t_{20}E_{incident}. \tag{A.12}$$

Both signals E_{sample} and $E_{\text{reference}}$ are measured, their ratio in the frequency domain contains information about the dielectric function. Let $Q = \frac{E_{\text{sample}}}{E_{\text{reference}}}$. After short calculations we obtain the general expression relating the complex transmission Q to the waveform's phase shift δ.

$$Qe^{ik_0d_1}\frac{2n_0}{n_0+n_2} = \frac{t_{01}t_{12}}{\exp(-i\delta) - r_{10}r_{12}\exp(i\delta)} \tag{A.13}$$

The left side of equation (A.13) is the experimentally determined transfer function of the system H_{exp}, while the right side represents the theoretical transfer function H_{theor}. With $\delta = k_1d_1 = \frac{\omega d_1 n_1}{c}$ equation (A.15) gives the general expression for the theoretical transfer function of the investigated material. H_{theor} depends on material parameters.

$$H_{\text{exp}} = Qe^{ik_0d_1}\frac{2n_0}{n_0+n_2} \tag{A.14}$$

$$H_{\text{theor}} = \frac{t_{01}t_{12}}{\exp(-i\delta) - r_{10}r_{12}\exp(i\delta)} \tag{A.15}$$

$$H_{\text{exp}} - H_{\text{theor}} = 0 \tag{A.16}$$

Material parameter extraction means solving equation (A.16). As equation (A.13) cannot be solved analytically, it can be either approximated or solved numerically. Let us explore both possibilities. First, we derive a formula for the 2nd order approximation of the dielectric function. Results obtained with this approximation will be compared in section A.5 with results of the numerical solution of Eq.(A.16) for various materials.

A.3 2nd order approximation

Let $n_1 = n$ be the searched refractive index of the sample (layer 1). As $n^2 = \epsilon$ equation (A.13) contains information on the dielectric function. To find an approximate solution of Eq.(A.13) we expand the exponential function in the Taylor series and substitute $\exp(i\delta) = 1 + i\delta - \frac{\delta^2}{2}$ to equation Eq.(A.13):

$$Qe^{ik_0d_1}\frac{2n_0}{n_0+n_2} = \frac{2n_02n}{(n_0+n)(n_2+n)\exp(-i\delta) - (n-n_0)(n-n_2)\exp(i\delta)}. \tag{A.17}$$

With $\epsilon = n^2$ is

$$Qe^{ik_0d_1}\frac{2n_0}{n_0+n_2} = \frac{2n_0}{(n_0n_2+\epsilon)(-i\frac{\omega d_1}{c})+(n_0+n_2)(1-\frac{(\frac{\omega d_1}{c})^2\epsilon}{2})}, \tag{A.18}$$

which gives the analytical expression for the dielectric function in the 2nd order approximation:

$$\epsilon = -\frac{c}{\omega d}\frac{i\frac{\omega d_1}{c}(n_0n_2)-(n_0+n_2)+\frac{(n_0+n_2)\exp ik_0d_1}{Q}}{i+(n_0+n_2)\frac{\omega d_1}{2c}}. \tag{A.19}$$

For all calculations we take $n_{\text{air}} = n_0 = 1.0+0i$ and for $n_{\text{Si}} = n_2 = 3.4155+0i$.

A.4 Model bounaries

The above derived model is used to calculate material parameters of a system of interest with an assumption that the theoretical transfer function is identical with the measured transfer function. To verify the validity of the model we impose the following condition which have to be met for the model to be correct: the formula (A.13) has to be reversible. For what type of samples does the approximation hold?

A.5 Model choice

We aim to solve an indirect electromagnetic problem. The dependence Q on ϵ is given by the above described model. The value of $H_{exp} = Qe^{ik_0d_1}\frac{2n_0}{n_0+n_2}$ is known - it is the transfer function of the sample material, it is the ratio of the measured signals in the frequency domain. We are interested in extracting material parameters from the measured signals, which are n, ϵ and σ, thus we are looking for the dependence $\epsilon(H_{\text{exp}})$.

As described in chapter A we can use two methods for parameter extraction. First, it is to solve the general formula:

$$Qe^{ik_0d_1}t_{02} - \frac{t_{01}t_{12}}{\exp(-i\delta)-r_{10}r_{12}\exp(i\delta)} = 0, \tag{A.20}$$

with $\delta = k_1d_1 = \omega\hat{n}d_1/c$. Eq. (A.20) is equivalent to

$$Q = \frac{t_{01}t_{12}e^{-ik_0d_1}/t_{02}}{\exp(-i\delta)-r_{10}r_{12}\exp(i\delta)}, \tag{A.21}$$

$$Q = \frac{\frac{2n_0}{n_0+\hat{n}}\frac{2\hat{n}}{\hat{n}+n_2}e^{-ik_0d_1}/\frac{2n_0}{n_0+n_2}}{\exp(-i\omega\hat{n}d_1/c)-\frac{\hat{n}-n_0}{n_0+\hat{n}}\frac{\hat{n}-n_2}{n_2+\hat{n}}\exp(i\omega\hat{n}d_1/c)}. \tag{A.22}$$

Equation (A.22) can be written in the form

$$Q - L_{\text{gen}}(\hat{n}, n_0, n_2, d_1, \omega) = 0, \tag{A.23}$$

where L_{gen} is an operator acting on the frequency space and complex refractive index of a material, by fixed parameters n_0, n_2, d_1, giving the theoretical transfer function Q_{theor}.

Minimizing the expression on the left side of equation (A.23), which is the difference between the measured transfer function Q and the theoretically determined transfer function Q_{theor} in the 2 layer model system (A), enables finding the solution, which is the unknown frequency dependent complex refractive index $\hat{n}$.

The second way to extract material parameters is to calculate ϵ directly by approximating $\exp(i\delta) \approx 1 + i\delta - \frac{\delta^2}{2}$ in the general formula (A.22) [Kam05]. The dielectric function ϵ is given then by

$$Qe^{ik_0 d_1}\frac{2n_0}{n_0 + n_2} = \frac{2n_0}{(n_0 n_2 + \hat{n}^2)(-i\delta/\hat{n}) + (n_0 + n_2)(1 - \frac{\delta^2}{2})}, \tag{A.24}$$

$$\epsilon = -\frac{c}{\omega d_1}\frac{i\frac{\omega d_1}{c}(n_0 n_2) - (n_0 + n_2) + e^{-ik_0 d_1}\frac{n_0 + n_2}{Q}}{i + (n_0 + n_2)\frac{\omega d_1}{2c}}, \tag{A.25}$$

In analogy, equations (A.24) and (A.25) can be represented as

$$Q = L_{2nd}(\hat{n}, n_0, n_2, d_1, \omega), \tag{A.26}$$

and

$$\epsilon = L_{2nd}^{-1}(Q, n_0, n_2, d_1, \omega), \tag{A.27}$$

where $\hat{\epsilon} = \hat{n}^2$.

To check the validity of both data evaluation methods we have calculated the dielectric function of two materials previously investigated with the same measurement setup. For reference on graphite (Highly Ordered Pyrolytic Graphite - HOPG) see [Kam05], [Sch05] and for the superconductor $Bi_2Sr_2CaCu_2O_{8+\delta}$ BSCCO see [Sch08].

Dielectric function of graphite

To compare the two methods we have calculated the dielectric function of graphite (HOPG) using both methods. Results are shown in the Fig.A.4.

First, the 2nd order approximation of the dielectric function was calculated with the measured transfer function Q, which is

$$\epsilon_{\text{black}} = L_{2nd}^{-1}(Q_{\text{black}}, n_0, n_2, d_1, \omega) \tag{A.28}$$

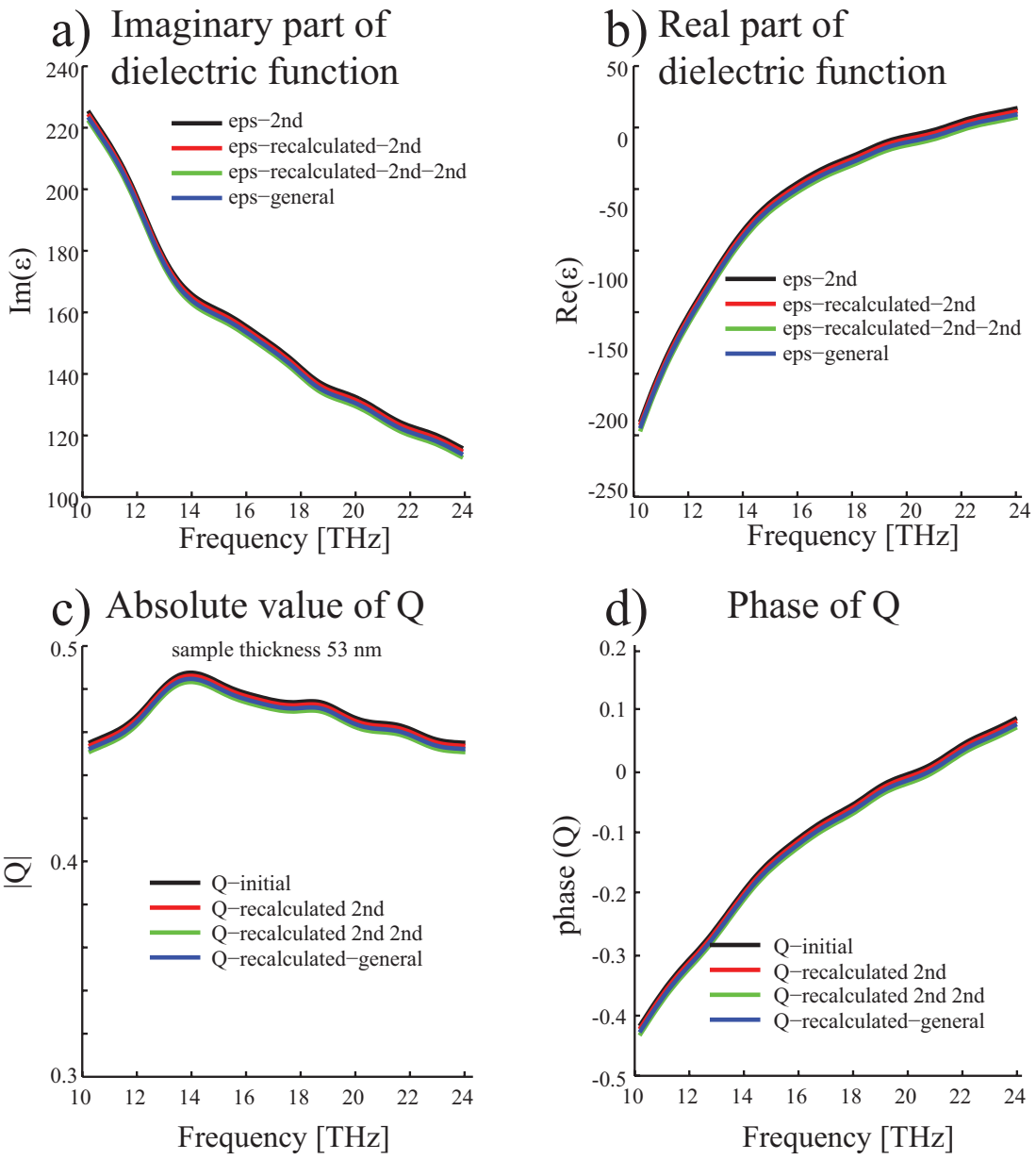

Figure A.4: Dielectric function of HOPG, comparison of the general model and the 2nd order approximation. See text for details.

The result is shown in Fig.A.4 a) and b). The dielectric function is printed black. The input data Q, the absolute value and the phase (black), are shown in the Fig.A.4 c) and d). If the model is correct, then inverting the action of the operator L_{2nd}^{-1} gives the input data Q. To check this we have applied the operator L_{2nd} to the calculated the dielectric function $\epsilon_{\mathrm{black}}$

$$Q_{\mathrm{red}} = L_{\mathrm{2nd}}(\sqrt{\epsilon_{\mathrm{black}}}, n_0, n_2, d_1, \omega). \tag{A.29}$$

The resulting recalculated transfer function Q_{red} is exactly equal to the initial transfer function Q_{black}. Furthermore, results of the next three iterations

$$\epsilon_{\mathrm{red}} = L_{2nd}^{-1}(Q_{\mathrm{red}}, n_0, n_2, d_1, \omega)$$

$$Q_{\mathrm{green}} = L_{\mathrm{2nd}}(\sqrt{(}\epsilon_{\mathrm{red}}), n_0, n_2, d_1, \omega)$$

$$\epsilon_{\mathrm{green}} = L_{2nd}^{-1}(Q_{\mathrm{green}}, n_0, n_2, d_1, \omega)$$

perfectly agree with the initial result. The formula for the 2nd order approximation is reversible.

The same iteration procedure (A.28) - (A.29) was applied to calculate $\epsilon_{\mathrm{general}}$ (blue) and to recalculate the transfer function Q (blue) and finally to prove the first described data evaluation model Eq. (A.23)

As presented in the Fig.A.4 a) and b) the dielectric function $\epsilon_{\mathrm{general}}$, a solution to the general formula, matches exactly the dielectric function calculated in the 2nd order approximation. The general formula is also reversible.

The obtained dielectric function complies with results published in literature [Kam05] in the 10 to 27 THz frequency range, which confirms the validity of used evaluation method.

It is important to note that for graphite the output of both methods is the same, but the first evaluation method is a precise one, as it solves the general formula, and the second method is an approximation valid only if $\exp(i\delta) \approx 1 + i\delta - \frac{\delta^2}{2}$.

Dielectric function of BSCCO

The same procedure was applied for BSCCO evaluation as for graphite evaluation Fig.A.5. Again all iterations give exactly the same input data, so both evaluation methods are reversible. However, the dielectric functions calculated in both ways are slightly different Fig. (A.5) a) and b). Obtained results are comparable with dielectric functions of BSCCO found in literature [Sch08].

Temperature dependence of the dielectric function

THz Spectroscopy allows for detection of temperature dependence of optical parameters. The temperature dependent dielectric function for BSCCO measured

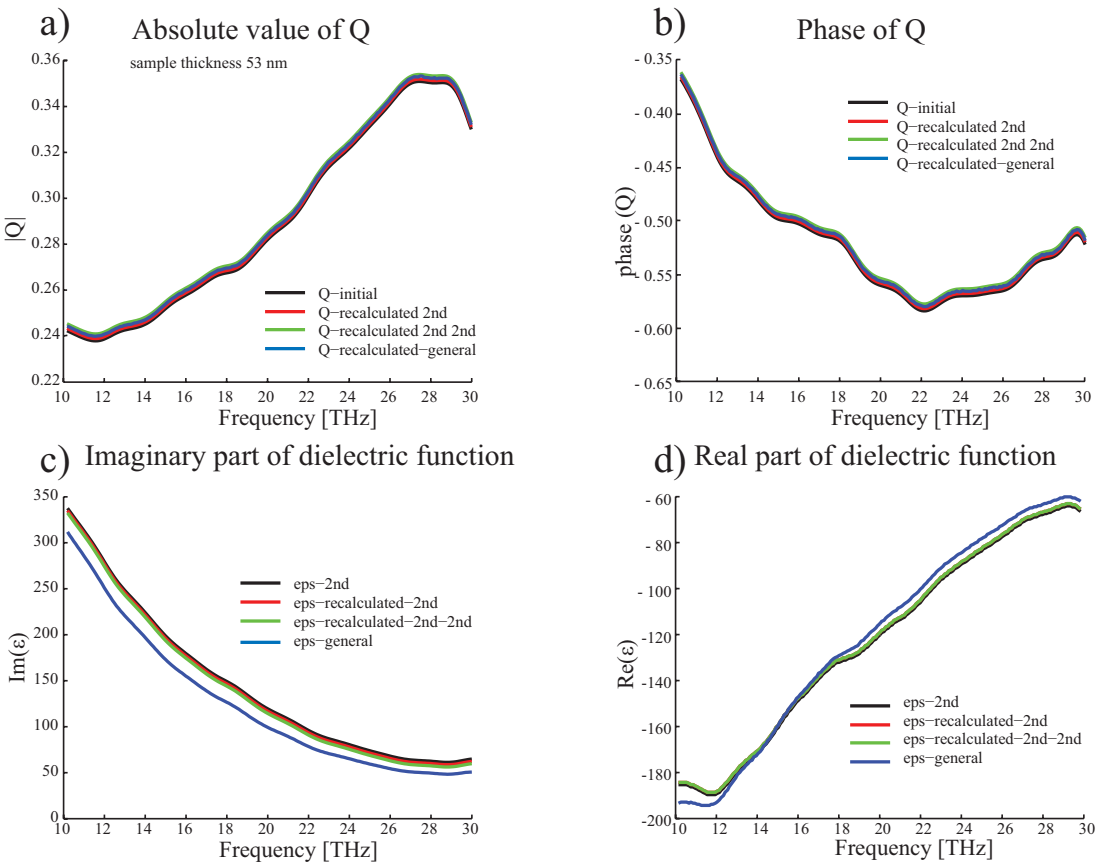

Figure A.5: Dielectric function of BSCCO, model comparison.

for four different temperatures is presented in Figure A.6. This results clearly shows, that changes of the dielectric function with temperature can be detected with TD-TS.

Dielectric function of PEDOT:PSS

The situation for PEDOT:PSS is different. Dielectric function of the polymer varies strongly depending on the model chosen for evaluation. As shown in graphic A.7, when the iteration procedure described above has been applied to every formula separately both formulas have proved to be reversible, as values of the initial transfer function Q (black), and recalculated in the 2nd order approximation transfer function $Q_{\mathrm{rec-2nd}}$ and doubly recalculated transfer function $Q_{\mathrm{rec-2nd-2nd}}$ are identical with the values of the recalculated transfer function in the general formula $Q_{\mathrm{rec-general}}$. Therefore each formula is reversible. The general formula (A.20) gives of course the exact solution of the 2 layer system model described in chapter A.

Considering the calculated dielectric function, the difference is not only in the

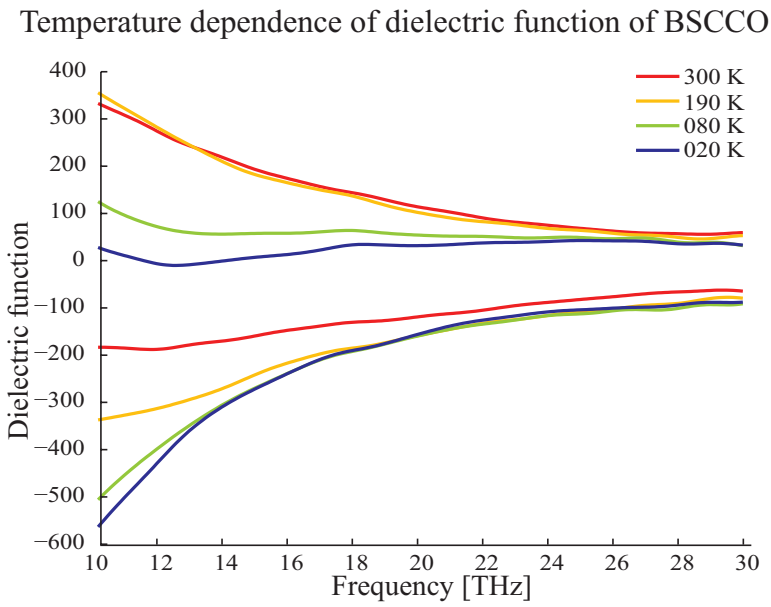

Figure A.6: Dielectric function of BSCCO, temperature dependence.

absolute value, which is up to 90% for the real part of ϵ. For the imaginery part of the dielectric function $\mathrm{Im}(\epsilon)$ calculated with the general formula is positive, while $\mathrm{Im}(\epsilon) < 0$ when calculated in the 2nd order approximation. A negative imaginary part of epsilon would mean that the polymer emitts more light as it absorbs, which would only be possible, if there is a population inversion before the laser pulse enters polymer. A population inversion in a ground state, an we assume that before measurement the polymer is in its ground state, is contradictory to the second law of thermodynamics. Therefore we reject the 2nd order approximation method and use the general formula as a solution (A.20) to the 2 layer system model for all further calculations.

The conclusion is that the 2nd order approximation for dielectric function commonly used in literature [Kam05], [Sch08] is not valid for PEDOT:PSS.

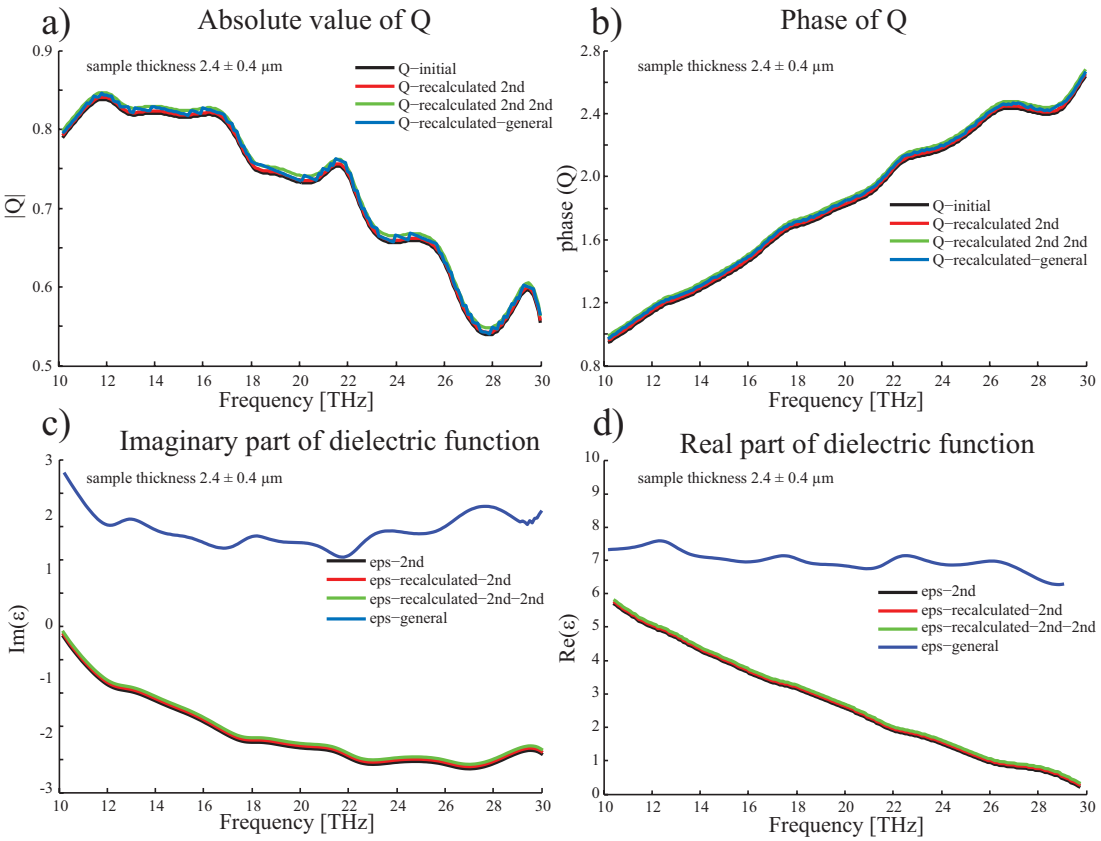

Figure A.7: Dielectric function of PEDOT:PSS, model comparison.

Appendix B

Optical material parameters

	Dielectric function $\hat{\epsilon}$	Conductivity $\hat{\sigma}$	Refractive index $\hat{n}$
$\hat{\epsilon}$	$\hat{\epsilon} = \epsilon_1 + i\epsilon_2$	$\epsilon_1 = 1 - \frac{4\pi\sigma_2}{\omega}$, $\epsilon_2 = \frac{4\pi\sigma_1}{\omega}$	$\epsilon_1 = \frac{n^2-\kappa^2}{\mu_1}$, $\epsilon_2 = \frac{2n\kappa}{\mu_1}$
$\hat{\sigma}$	$\sigma_1 = \frac{\omega\epsilon_2}{4\pi}$, $\sigma_2 = \frac{\omega(1-\epsilon_1)}{4\pi}$	$\hat{\sigma} = \sigma_1 + i\sigma_2$	$\sigma_1 = \frac{n\kappa\omega}{2\pi\mu_1}$ $\sigma_2 = (1 - \frac{n^2-\kappa^2}{\mu_1})\frac{\omega}{4\pi}$

Table B.1: Relationships between optical material parameters

Appendix C

Results obtained for various film thicknesses

In the figure C.1 are presented the dielectric functions extracted for measured samples. Interesting is the comparison between the results for thick samples ($d = 1700,\ 2400$ nm), which were evaluated in this work, with the results for thin samples ($d < 140$ nm). We have found, that PEDOT:PSS films with thickness below 140 nm are unsuitable for THz measurements. The change is the signal amplitude (see section 3.1 for details) is comparable with the measurement error. The dielectric function extracted for thin films ($d < 140$ nm) cannot be reproduced.

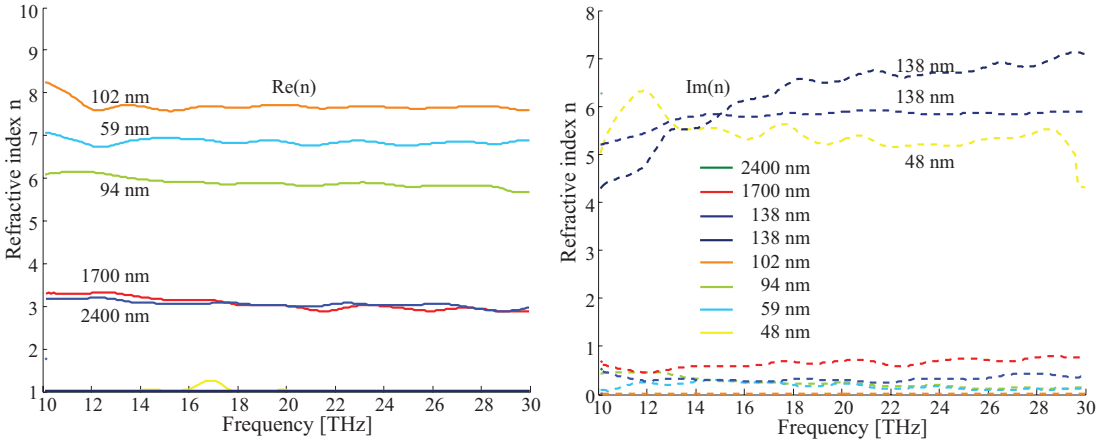

Figure C.1: Dielectric function derived for PEDOT:PSS thin-films in the thickness range from 49 nm to 2400 nm. a) Real part b) imaginary part. The dielectric function varies strongly for samples with thickness under 140 nm.

Bibliography

[ABK+06] X. Ai, M. Beard, K. Knutsen, S. Shaheen, G. Rumbles, and R. Ellingson. *Photoinduced Charge Carrier Generation in a Poly(3-hexylthiophene) and Methanofullerene Bulk Heterojunction Investigated by Time-Resolved Terahertz Spectroscopy.* J. Phys. Chem. B 2006, 110, 25462-25471, 2006.

[AHO05] S. Ashizawa, R. Horikawa, and H. Okuzaki. *Effect of solvent on carrier transport in poly(3,4-ethylenedioxythiophene)/poly(4 styrenesulfonate).* Synthetic Materials 153 (2005) 5-8, 2005.

[AM76] N. Ashcroft and N. Mermin. *Solid State Physics.* Holt, Rinehart and Winston, 1976.

[And58] P. W. Anderson. *absence of diffusion in certain random lattices.* Phys. Rev. 109 (1958) 1492, 1958.

[Bar05] W. Barford. *Electronic and Optical Properties of Conjugated Polymers.* Clarendon Press, Oxford, 2005.

[BKN+08] S. Bange, A. Kuksov, D. Neher, A. Vollmer, N. Koch, A. Ludemann, and S. Heun. *Organic Electronic Devices and Their Functional Interfaces.* J. of Appl. Phys. 104, 104506, 2008.

[Bru08] W. Bruetting. *Grundlagen der organischen Halbleiter.* Physik Journal 7 (2008), 2008.

[CLRR98] S. Capacciolo, M. Lucchesi, P. A. Rolla, and G. Ruggeri. *Dielectric response analysis of a conducting polymer dominated by the hopping charge transport.* J. Phys. Condens. Matter 10 (1998) 5595-5617, 1998.

[CMO+03] X. Crispin, S. Marciniak, W. Osikowicz, G.Zotti, A. W. Danier Van Der Gon, F. Louwet, M. Fahlman, L. Groenendaal, F. De Schryver, and W. R. Salaneck. J. Polym. Sci. B Polym. Phys. 41 (2003) 2561, 2003.

[CWLT00] H. P. Chiang, Y. C. Wang, P. T. Leung, and W. S. Tse. *A theoretical model for the temperature-dependent sensitivity of the optical sensor based on surface plasmon resonance.* Optics Communications 188 (2001) 283-289, 2000.

[DBL+08] A. Dkhissi, D. Beljonne, R. Lazaroni, F. Louwet, and B. Gronendaal. *Modeling of the solid-state packaging of charged chains (PEDOT) in the presence of the counterions (TSA) and solvent (DEG).* Theor Chem Account(2008) 119:305-312, 2008.

[DBM01] T. Dorney, R. Baraniuk, and D. Mittleman. *Material parameter estimation with terahertz time-domain spectroscopy.* J. Opt. Soc. Am. A/Vol. 18, No. 7, 2001.

[DD08] C. Deibel and V. Dyakonov. *Sonnenstron aus Plastik.* Physik Journal 7 (2008) Nr.5, 2008.

[Deg06] L. Degiorgi. *The Drude model in correlated systems.* Ann. Phys. 15, No. 7-8, 571-584(2006), 2006.

[DG02] M. Dressel and G. Grüner. *Electrodynamics of Electrons in Matter.* Cambridge University Press, 2002.

[DGBZ89] B. Deroide, J. C. Giuntini, P. Belougne, and J. V. Zanchetta. *Numerical approach to hopping conduction.* Journal of Materials Science 24 (1989) 53-56, 1989.

[Dre] M. S. Dresselhaus. *Solid state physics. Optical Properties of Solids. PART II.* Lecture notes.

[Dru00] P. Drude. *On the electron theory of metals.* Annalen der Physik 1, 566, 1900.

[Fix08] W. Fix. *Elektronik aus der Rolle.* Physik Journal 7 (2008) Nr.5, 2008.

[Gal] Y. Galperin. *Introduction to modern solid state physics.* Lecture notes.

[GJF+00] L. Groenendaal, F. Jonas, D. Freitag, H. Pielartzik, and J. R. Reynolds. *Poly(3,4-ethylenedioxythiophene) and Its Derivatives: Past, Present, and Future.* Advanced Materials 12, 481, 2000.

[GP06] S. D. Ganichev and W. Prettl. *Intense Terahertz Excitation of Semiconductors.* Oxford Science Publications, 2006.

[HFGR+07] I. Horcas, R. Fernandez, J. M. Gomez-Rodrigues, J. Colchero, J. Gomez-Herrero, and A. M. Barro. Review of Scientific Instruments 78, 013705 (2007), 2007.

[Hol54] T. Holstein. *Optical and Infrared Volume Absorptivity of Metals.* Phys. Rev. 96(1954) 535, 1954.

[Hol64] T. Holstein. *Theory of transport phenomena in an electron-phonon gas.* Ann. Phys.(NY) 29 (1964) 410, 1964.

[HS07] I. Hertel and C. P. Schultz. *Atome, Moleküle und optische Physik, Band I.* Springer, 2007.

[Jac99] J. Jackson. *Classical Electrodynamics.* Wiley ans Sons, 1999.

[JB09] A. Haldi J. Birnstock. *OLEDs und organische Elektronik auf dem Vormarsch.* Wiley-VCH Verlag, Optik and Photonik Nr.1, 2009.

[Kam05] T. Kampfrath. *Charge-Carrier Dynamics in Solids and Gases Observed by Time-Resolved Terahertz Spectroscopy.* Im Fachbereich Physik der Freien Universität Berlin eingereichte Dissertation, 2005.

[KH08] M. Klein and K. Heuser. *Lichthimmel und Lichttapeten.* Physik Journal 7 (2008) Nr.5, 2008.

[Kit96] C. Kittel. *Introduction to solid state physics.* John Wiley and Sons, 1996.

[KJ08] E. Kim and J.Bredas. *Electronic Evolution of Poly(3,4-ethylenedioxythiophene) (PEDOT): From the Isolated Chain to the Pristine and Heavily Doped Crystals.* J. Am. Chem. Soc. 130, 16880–16889, 2008.

[Koc07] N. Koch. *The role of poly (3,4-ethylenedioxythiophene):poly(styrenesulphonate) as a hole injection layer in a blue-emitting polymer light-emitting diode.* Physik Journal 7 (2008), 2007.

[Koc08] N. Koch. *Energy levels at interfaces between metals and conjugated organic molecules.* J. Phys. Condens Matter 20 (2008) 184008, 2008.

[KR05] S. Kirchmeyer and K. Reuter. *Scientific importance, properties and growing applications of poly (3,4-ethylenedioxythiophene).* J. Mater. Chem, 15, 2077-2088, 2005.

[Law76] W. E. Lawrence. *Electron-electron scattering in low-temperature resistivity of noble-metals.* Phys. Rev. B 13 (1976) 5316, 1976.

[LBNL08] K. Leo, J. Blochowitz-Nimoth, and O. Langguth. *Vom Handy bis zum Fernseher.* Physik Journal 7 (2008) Nr.5, 2008.

[MD71] N. F. Mott and E. A. Davis. *Electronic Processes in Non-Crystalline Materials.* Clarendon Press Oxford, 1971.

[Nar07] A. Nardes. *On the conductivity of PEDOT:PSS thin films.* Thesis submitted at the Electronic System Engineering Department of Polytechnic School of the University of Sao Paulo, Brazil., 2007.

[NJK08] A. Nardes, R. Janssen, and M. Kemerink. *A Morphological Model for the Solvent-Enhanced Conductivity of PEDOT:PSS Thin Film.* Adv. Funct. Mater. 2008, 18, 865-871, 2008.

[NKJ07] A. M. Nardes, M. Kemerink, and R. A. J. Janssen. *Anisotropic hopping conduction in spin-coated PEDOT:PSS thin films.* Physical Review B 76, 085208, 2007.

[Nöt07] J. Nötzold. *Ultraschnelle Entmagnetisierung Laserangeregter Ferromagneten untersucht mit zeitaufgelöster Terahertz-Emissions-Spektroskopie.* Diplomarbeit Uni Konstanz, gefertigt an der FU-Berlin, 2007.

[NVMM] E. Nguema, V. Vigneras, J. L. Miane, and P. Mounaix. *Dielectric properties of conducting polyaniline films by THz time-domain spectroscopy.* European Polymer Journal 44 (2008) 124-129.

[PG61] M. Pollak and T. H. Geballe. *Low-frequency conductivity due to hopping processes in silicon.* Phys. Rev. 122 (1961) 1742, 1961.

[PGI02] L. Pettersson, S. Ghosh, and O. Inganas. *Optical anisotropy in thin films of poly(3,4-ethylenedioxythiophene)-poly(4-styrenesulfonate).* Organic Electronics 3 (2002) 143-148, 2002.

[PWK07] I. Pupeza, R. Wilk, and M. Koch. *Highly accurate optical material parameterdetermination with THz time-domain spectroscopy.* Optics Express 4335, Vol. 15, No.7, 2007.

[SBJ+04] M. Schubert, C. Bundesmann, G. Jakopic, H. Maresch, H. Arwin, N. C. Persson, F. Zhang, and O. Inganas. *Infrared ellipsometry characterization of conducting thin organic films.* Thin Solid Films 455 –456 (2004) 295–300, 2004.

[Sch05] F. Schapper. *THz-Spektroskopie von Graphit und Erzeugung geformter Laserpulse im mittleren Infrarot.* Im Fachbereich Physik der Freien Universität Berlin eingereichte Diplomarbeit, 2005.

[Sch08] M. Scheuch. *Ladungsträgerdynamik in hochkorrelierten Elektronensystemen untersucht mit zeitaufgelöster THz-Spektroskopie.* Im Fachbereich Physik der Freien Universität Berlin eingereichte Diplomarbeit, 2008.

[SGF07] J. Sun, W. Gerberich, and L. Francis. *Transparent, conductive polymer blend coatings from latex-based dispersions.* Progress in Organic Coatings 59, 115-121, 2007.

[SKSM02] K. Sieranski, M. Kubisa, J. Szatkowski, and J. Misiewicz. *Polprzewodniki i struktury polprzewodnikowe.* Oficyna Wydawnicza Politechniki Wroclawskiej, 2002.

[SMH00] H. Shirakawa, A. G. MacDiarmid, and A. J. Heeger. *The Nobel Prize in Chemistry 2000 for the discovery and development of conductive polymers.* Nobel Foundation, 2000.

[Smi01] N. V. Smith. *Classical generalization of the Drude formula for the optical conductivity.* Physical Review B, Vol. 64, 155106, 2001.

[Son09] Sony. *OLED Digital TV.* http://www.sonystyle.com/, 2009.

[SR07] T. Skotheim and J. Reynolds. *Handbook of Conducting Polymers.* Wiley-VCH, 2007.

[ST07] B. E. A. Saleh and M. C. Teich. *Fundamentals of Photonics.* Wiley and Sons, 2007.

[Sta09] C. H. Starck. *Organic LED.* http://www.clevios.com/, 2009.

[SW05] M. Schwoerer and H. C. Wolf. *Organische Molekulare Festkörper.* Wiley-VCH, 2005.

[TKT+04] S. Timpanaro, M. Kemerink, F. Touwslager, M. Kok, and S. Schrader. *Morphology and conductivity of PEDOT/PSS films studied by scanning-tunneling microscopy.* Chemical Physics Letters 394 (2004) 339-343, 2004.

[TS87] C.W. Tang and S. A. Van Slyke. *Electronic and Optical Properties of Conjugated Polymers.* Appl. Phys. Lett. 51, 913, 1987.

[vLFK+08] H. A. v. Laarhoven, C. F. J. Flipse, M. Koeberg, M. Bonn, E. Hendry, G. Orlandi, O. D. Jurchescu, T. T. M. Palstra, and A. Troisi. *On the mechanism of charge transport in pentacene.* J. Chem. Phys. 129, 044704, 2008.

Acknowledgement

I am grateful to those, who made this thesis possible. During this work I have collaborated with many colleagues, for whom I have great regard.

Foremost, I would like to express my deepest gratitude to my adviser Prof. Dr. Martin Wolf, for his open approach and support in developing my interests.

I thank my coworkers, who have assisted me in numerous ways:

Priv.-Doz. Dr. Christian Frischkorn especially for his detailed review of this thesis;

Konrad von Volkmann for sharing his experience and suggestions concerning laboratory routine and experimental methods;

Martin Scheuch for his always enjoyable cooperation, patience, help with measurements and numerous discussions;

Dr. Tobias Kampfrath for discussions about THz and carbon nanotubes;

Uwe Lipowski, for many hints for technical drawings;

Dr. Peter West, for helping in dealing with all sorts of applications;

Dietgard Mallwitz, for always friendly smile and help with administrative matters;

I thank all members of the group of Prof. Wolf for their support.

I thank Dr. Norbert Koch for detailed and constructive comments concerning the physics of PEDOT:PSS and Dr. Ingo Salzmann for teaching me sample preparation techniques.

I thank the engineers from the mechanical and electrical workshops for manufacturing parts of equipment used in experiments.

I wish to thank Christian Lotze for his assistance with AFM measurements.

I warmly thank Alexander Gottberg for fabrication of electrodes for the THz spectrometer and for his guidance.

My sincere thanks also goes to Linus Duchstein for his support in moments of pessimism.

I also thank the German National Science Foundation and the Hertie Foundation for their financial support for the duration of this work.

And finally I thank my parents for constant encouragement and for caring about my education so much. If it hadn't been for them, I would not be writing these words now.

Erklärung gemäß Paragraph 17, Abs. 7 DPO

Ich versichere hiermit, diese Arbeit selbständig verfaßt und keine anderen als die angegebenen Hilfsmittel benutzt zu haben.

Berlin, den 29. Mai 2009